Graduate Theses and Dissertations   Graduate School

January 2012

Design of Colloidal Composite Catalysts for CO2 Photoreduction and for CO Oxidation

Bijith D. Mankidy
University of South Florida, bmankidy@mail.usf.edu

Design of Colloidal Composite Catalysts for CO_2 Photoreduction

and for CO Oxidation

by

Bijith D. Mankidy

A dissertation submitted in partial fulfillment
of the requirements for the degree of
Doctor of Philosophy
Department of Chemical and Biomedical Engineering
College of Engineering
University of South Florida

Co-Major Professor: Vinay K. Gupta, Ph.D.
Co-Major Professor: Babu Joseph, Ph.D.
John Kuhn, Ph.D.
Ashok Kumar, Ph.D.
Kirpal Bisht, Ph.D.

Date of Approval:
October 5, 2012

Keywords: Nanoparticle, Cobalt, Titania, Insitu, FTIR

DEDICATION

Dedicated to the late Dr. John Wolan.

ACKNOWLEDGMENTS

TABLE OF CONTENTS

ii

LIST OF TABLES

LIST OF FIGURES

x

ABSTRACT

In this doctoral dissertation, novel colloidal routes were used to synthesize nanomaterials with unique features. We have studied the impact of nanoparticle size of catalyst, role of high surface area of a photocatalyst, and the effect of varying elemental composition of co-catalytic nanoparticles in combination with core-shell plasmonic nanoparticles. We have demonstrated how physical and chemical characteristics of nanomaterials with these unique features play a role in catalytic reactions, specifically the oxidation of CO and the photoreduction of CO_2. The first objective of this doctoral dissertation involved the preparation of CoO nanoparticles with discrete nanoparticles sizes (1-14 nm) using a colloidal thermal decomposition technique. The impact of size of CoO for CO oxidation reaction was studied using an in-situ FTIR reactor. By analyzing the reaction intermediates observed using in-situ IR, a two-step reaction mechanism was proposed. The average values of activation energies of step-1 and step-2 were ~15 kJ/mol and ~90 kJ/mol that showed step-2 was the rate determining step. From activation energy calculations for the catalysts of different CoO sizes, it was found that activation energy increased as nanoparticle size increased. The second objective of this doctoral research involved the development of high surface area TiO_2 nanoshells using polymeric templates. The deposition of TiO_2 was achieved by surface functionalization procedures. TiO_2 was then deposited on colloidal SiO_2 after the SiO_2 surface was modified by grafting poly(NIPAAM) oligomers. TiO_2 nanoshell composites possessed high surface of ~35 m^2/gm. The photocatalytic performances of TiO_2 nanoshells and Pt

deposited TiO_2 nanoshells were evaluated for CO_2 photoreduction reaction. Primary products from CO_2 photoreduction reactions were carbon monoxide and methane. The product yield and product selectivity of hydrocarbons produced during CO_2 photoreduction was measured using a home-built FTIR reactor. When Pt was deposited on TiO_2 nanoshells, the overall yield was nearly doubled and the CH_4 selectivity nearly quadrupled. The third objective pursued in this research project was to synthesize Ag, Pt and bimetallic Ag-Pt nanoparticles to demonstrate the role of elemental composition of metal co-catalysts for CO_2 photoreduction reaction. The novel bimetallic nanoparticles played an important role in improving product selectivity in the photocatalytic reduction of CO_2. Bimetallic Ag-Pt nanoparticles synthesized with low Pt content had 4-5 times higher CH_4 selectivity compared to native TiO_2. The final objective was to prepare Ag(core)/SiO_2(shell) nanoparticles with specific core-shell structure to enhance photoactivity of TiO_2 during catalytic reactions. Ag@SiO_2 core-shell nanoparticles have plasmonic character that helped to improve product yield by increasing the number of electron-hole pair generations. When bimetallic Ag-Pt nanoparticles were used in combination with core-shell Ag@SiO_2 plasmonic nanoparticles, the overall yield increased ~8-fold compared to native TiO_2.

xii

CHAPTER 1: COLLOIDAL COMPOSITES FOR CATALYSIS

1.1 Nanomaterials: Properties and applications

In recent years, nanomaterials have been the subject of extensive interest due their potential uses in a wide range of areas such as electronics, therapeutics, diagnostics, catalysis, and sensing. The versatility of nanomaterials stems from their unique optical, magnetic, thermal, and mechanical properties that result from their small dimensions. Some of the significant characteristics that determine the structure-property relationships in nanomaterials are size, shape, elemental composition, and geometric structure.

The extensive literature on gold (Au) nanocomposites is one example wherein these structure-property relationships can be observed. For example, catalytic reactions performed using bulk and nanoparticles of Au demonstrate the critical role of size [1-3]. Au nanoparticles have been found to be highly active as catalysts for water-gas shift reaction[1] and carbon monoxide (CO) oxidation reaction[2, 3], whereas bulk Au is virtually inactive. In other reports different shapes such as nanospheres, nanocubes, truncated nanocubes, triangular nanoprisms, and nanorods have been used to show unique applications in biological imaging and biomedicine[4-6].

Elemental composition of a catalyst material is also an important factor that determines the function. For instance, in a study on gold catalysts, Scott and coworkers

1

found that by alloying Au nanoparticles with Pd metal, the activity of CO oxidation reaction was increased[7]. In another study, Mott and[i] coworkers[8] found the chemical interaction of reactants was significantly different during electro-oxidation of methanol when Au nanomaterial composition was alloyed with platinum (Pt).

The influence of geometric structure of nanomaterials is also evident from studies on core-shell particles of Au(core)-silica shell (Au@SiO_2) as well as the reverse geometry, namely SiO_2@Au core-shell particles. These core-shell particles, Au@SiO_2 and SiO_2@Au, have distinct optical properties. Colloidal Au nanoparticles suspended in an aqueous medium without aggregation have an optical absorbance typically near the 520nm wavelength region[9, 10]. Deposition of thin SiO_2 shell can cause a red-shift of the peak position to ~550nm[9, 11]. In contrast, when the structure of nanoparticles is reversed to SiO_2@Au core-shell structure, the visible absorbance can red shift to near-infrared (IR) regions[12, 13]. Since skin, tissue, and hemoglobin have a transmission window in the range from orange-red of visible wavelengths to near-IR, SiO_2@Au with a characteristic optical response in the IR can be used for photo-thermal therapy applications[12, 14, 15].

Therefore, the ability to tune physical, chemical and structural properties of nanomaterials leads to a multitude of potential applications. Within this multiplicity of applications, the research project described in this dissertation focuses on chemical catalysis.

2

1.2 Role of key features of nanomaterials in chemical catalysis

Nanomaterials have long been used as a catalyst of various reactions since nano-size particles and clusters maximize the sites for catalytic reactions. In the last century, nanomaterials used for catalysis have revolutionized many industrial applications. For example, ZSM-10, a nanostructured zeolite material was developed by controlling features such as size, structure, shape and composition. Since then there has been rampant use of ZSM-10 in the petrochemical industries for processing several billions of barrels of petroleum and chemicals on an yearly basis[16]. Another example is from the refinery industry that started to utilize precious metal Pt nearly fifty years ago for increasing the octane number of gasoline through a process called platforming. Prior to the discovery of using Pt, refineries added lead (Pb) metal or benzene compounds to meet octane number requirements combustion engines. Platforming was beneficial to eliminate environmentally unfriendly Pb and benzene; however, Pt is an expensive metal a relatively low catalyst life. Since then, several researchers have attempted to improve performance and to reduce catalyst cost by engineering the size and composition of the catalyst. According to a study in 2005, the market for reforming catalyst is about $100M[16]. Due to the increasingly stringent regulatory prerequisites, researchers are striving to find ways to improve the performance of refinery processes. Engineered nanomaterials have the potential to allow catalyst standards become at par with regulatory standards and to provide a safer and cleaner environment.

The great interest in catalysts with enhanced longevity, improved activity, and product selectivity has led to an increased focus on how physical and chemical characteristics of nanomaterials can influence reactions. In spite of extensive research,

3

clear and systematic principles are yet to be determined regarding paths by which a new nanomaterials catalyst performs in the course of a specific reaction.

In this section, we briefly look at the scientific research on the role of four important features (figure 1.1) of nanomaterials; size, surface area, elemental composition and geometrical structure in catalysis.

1.2.1 Size

As the size of a nanoparticle decreases, the percentage of atoms on the surface with low coordination number (Coordination number of an atom is defined as the number of nearest neighboring atoms to the central atom) increases. This has two implications.First, only surface atoms are useful for catalysis, therefore nanomaterials lead to increased number of active sites per unit mass of catalyst material. For nanomaterials, the percentage of atoms on the surface and the percentage of atoms at the step edges or corners increase exponentially with a decrease in size, when size decreases from ~30nm to 1nm. This is very beneficial from an economic standpoint if the catalyst metal used is expensive. Second, the atoms present in corners or edges of a nanoparticle with low coordination numbers possess unique electronic properties compared to an atom on a flat surface with high coordination number. For example, studies on ruthenium, Ru(001), single crystal by Dahl and coworkers[17] have shown high reactivity of atoms with low coordination numbers. They have demonstrated using experiments and density functional theory (DFT) that dissociation of nitrogen (N_2) on step sites was a billion (10^9) times greater than on a terrace site. This is because the energetics of the surface atoms on a terrace or a corner site is different than the effect of the interaction of adsorbing molecule with the surface atoms. Therefore, nanomaterials

4

of different sizes can be potentially used in catalysis to tune the reactivity of the chemical reactions.

One of the most common reactions that has been used to understand the role of nanoparticle size is CO oxidation reaction, which is a reaction relevant from an industrial and scientific point of view. Industrial applications include detoxification CO gas pollutants from automobile exhausts, gas cylinders used in hospitals, and industrial flue gases. Another important application is in fuel cell industry to preferentially oxidize CO in a hydrogen (H_2) feed-gas containing impurities of CO. From a scientific point of view, the reaction of carbon monoxide involves a molecular level interaction of a simple CO molecule that allows us to probe fundamental theories in catalysis.

Various researchers have studied different types of nanomaterials and the role of size of the catalyst on CO oxidation reaction. Haruta's research group [18, 19] has studied the effect of nanoparticle size for CO oxidation reaction on Au and Pt. They found that turn-over frequency (TOF) increases for Au but decreases for Pt when the nanoparticle size decreases. Studies by McCarthy and coworkers[20] on Pt nanoparticles have shown a similar trend where larger Pt nanoparticle have higher catalytic activity. Shaikhutdinov and coworkers[21] showed by adsorption measurements that smaller Au nanoparticles adsorb CO more strongly. On the contrary, a theoretical thermodynamic model for Pt nanoparticle developed by Lu and coworkers[22] illustrated that activation energy decreases as Pt nanoparticle size decreases. The calculations of activation energy were based on changes in the cohesive energy and electron affinity between the nanoparticle atoms as size varies. Overbury and coworkers[23] report the opposite trend for Au where the reaction TOF decreased as size was decreased from 10

5

to 2nm. Furthermore, Valden and coworkers[24] found that there was a maximum TOF for Au particles with a size of 3.5nm and lower activity for other sizes below and above 3.5nm. Grass and coworkers[25] have investigated rhodium (Rh) nanoparticles and showed improved activity for smaller nanoparticles. In contrast, studies on Ru nanoparticles by Joo and coworkers[26], and irridum (Ir) nanoparticles by Boudart and coworkers[27] showed that larger Ru and Ir particles have higher activity.

The studies on Au, Pt, Ru, Rh, Ir and other noble metals indicate that for CO oxidation reaction the role of nananoparticle size cannot be predicted for all metal elements due to the wide variation in results. Nørskov research group [28, 29] have used density functional theory calculations to predict reaction rates of different metal catalysts by applying Sabatier principles. For instance, if the adsorption energy of the reactant is too low, it means that the interaction is weak and the coverage of the reactant on the catalyst surface would be low leading to low rates of reaction. On the other hand, if the interaction is too strong, the ability of the reactant to dissociate or otherwise take part in a reaction can be hindered again leading to lower reaction rates. This leads to a volcano type behavior when the TOF is plotted as a function of absorption energy of the reactant on the surface. Sabatier plots of 12-atom clusters composed of different metals were also simulated to compare the above results obtained from extended metal surface catalysts. It was shown that platinum and palladium are the most active catalysts for extended surfaces and gold is the most active for 12-atom clusters[28]. The above mentioned experimental and theoretical studies have shown the reactivity of noble metal extended surfaces and 12-atom clusters. However, performing computer simulations on nanoparticles in the size range of 1-100nm to understand reactivity is highly challenging since they require extreme computational complexity. From a practical standpoint,

6

metals of first row transition elements are more inexpensive and widely available than noble metal counterparts. There are fewer reports in the literature available on first row transition metals presumably because the preparations of first row transition metals are more challenging due to their poor stability from agglomeration and difficulty to prepare them in discrete sizes.

Thus, there is a need to develop methods for nano-sized catalyst synthesis using inexpensive metals such as iron (Fe), cobalt (Co) or nickel (Ni) to investigate the role of the size of these catalysts on CO oxidation. In this dissertation, we provide insights into both of these challenges for the specific case of Co.

1.2.2 Surface area

Another feature that attracts the use of nanoparticles and nanomaterials, in general, for catalytic applications is the enhanced surface-to-volume ratio. High surface area of a catalyst material is beneficial because it increases the total number of active sites available for reactant molecules that helps to enhance the overall rate of reaction. In chemical catalysis, increasing both surface area and porosity promotes catalytic activity; therefore, a number of studies have pursued novel routes for catalyst preparation. Ledoux and coworkers[30] have synthesized high surface metal carbides and shown increase rate of reaction for isomerization or dehydrogenation of hydrocarbons due to the increase in specific surface area. Syntheses of porous structures of inorganic materials such as SiO_2, zirconia (ZrO_2), and ceria (CeO_2) have also been reported. Reports on SiO_2 by Zhao and coworkers have shown that highly porous structures of tunable morphologies such as fiber-, rope-, doughnut-, sphere-, gyroid-, and discoid- like shapes can be synthesized[31]. Terribile and coworkers

7

demonstrated preparation and characterization of high surface area mesoporous CeO_2 with pore sizes of 40Å[32]. Chuah and coworkers have studied the preparation conditions that influence porosity and surface area of ZrO_2 catalyst[33]. In all of these studies, the porosity and surface area enhancement has been found to be beneficial for the reaction rate kinetics.

In the special case of photocatalysis, since reactions are initiated by the interaction of light on the surface of the catalyst, it is critical to increase the exposed surface area. Porous structures contribute towards increasing internal surface area, but photoreactions may not be improved since light can be blocked from reaching the porous interiors. Thus, great care has to be taken for choosing catalysts and their supports for photochemical reactions. Amongst the many photocatalyst that have been investigated, titania (TiO_2) is a popular choice because it is cheaply available, highly stable and non-toxic.

Exhaustive physical characterization[34, 35] of TiO_2 and photocatalytic reactions[36-40] have been done by several researchers since its discovery as a photocatalyst by Fujishima and Honda[41] nearly half a century ago. Precipitation and electrochemical methods have been developed for creating highly ordered 3-D porous structures, coatings, films, nanotubes, nanoparticles of TiO_2 by careful crystallization and calcination[42-49]. Colon and coworkers have used a precipitation technique to deposit TiO_2 nanoparticles on templates of highly porous activated carbon[47]. Macák and coworkers have synthesized highly porous TiO_2 nanotubes with high aspect ratios by tailoring the conditions during electrochemical anodization of titanium[42]. Chu and coworkers also applied electrochemical anodization techniques to synthesize a three-

8

dimensional highly porous photocatalyst composite of TiO_2 with SiO_2, tellurium oxide (TeO_2), and alumina (Al_2O_3)[46]. Grimes' research group synthesized self-aligned highly ordered TiO_2 nanotube arrays[48] by anodization methods and found that nanotubes were useful for catalyst for the photoreduction of CO_2 to synthetic hydrocarbons[50].

While there is sufficient information in the literature to create highly porous structures, there are fewer reports on TiO_2 photocatalyst where the focus is to increase exposed surface area rather than porous interiors. Use of femtosecond lasers, lithography, or plasma and chemical etching techniques can be approaches to create high surface nano-features to increase the exposed surface area[51-55]. However, these methods are either slow or highly energy intensive. In this dissertation, we propose to apply colloidal methods to create TiO_2 photocatalyst with high exposed surface area.

1.2.3 Elemental composition

Choosing a right metal element for catalysts is critical since this determines the activity and selectivity of the reaction. Studies indicate that alloys or multi-metallic catalyst particles exhibit more favorable reaction kinetics compared to catalysts composed exclusively of their parent metal element[56]. This can sometimes be explained in terms of the work function of the final alloy nanoparticle compared to the work function of the original parent metals. The introduction of a promoter metal on the surface of a catalyst, for example, causes a shift in the d-band center due to the shift in the electron density from the metal with filled d-states to the other metal with less filled d-states. The shift in the d-band center affects the interaction of adsorbing molecules with the catalyst surface and results in significant alteration in activation energies and catalytic activities.

9

One of the best examples of bimetallic nanoparticles used in photocatalytic reduction of nitrate-to-nitrite is palladium-copper (Pd-Cu) bimetallic particles[57, 58] The Pd-Cu bimetallic photocatalyst composite is beneficial in removing nitrate toxicity in water that otherwise causes a disease to infants called the blue baby syndrome. Another example is the addition of manganese (Mn) to Fe based Fischer-Tropsch Synthesis (FTS), which leads to an improvement in light olefin production compared to the unpromoted Fe catalyst[59]. Addition of molybdenum (Mo) to Fe based FTS catalyst has shown higher stability and longevity[60].   Promoters of chromium (Cr), Mn, Mo, tantalum (Ta), vanadium (V), tungsten (W) and zirconium (Zr) have been also investigated by Lohitharn and coworkers for Fe based FTS catalysts[61]. Lee and coworkers have found that there was an increase in activity and stability of catalysts for oxygen reduction reaction in proton exchange membrane cells when catalysts were prepared by alloying Pt and Pd[62]. There are numerous other examples of different alloys used for a variety of reactions.

In this dissertation, our focus is to design an alloy co-catalyst for assisting TiO_2 based photocatalyst for carbon dioxide (CO_2) photoreduction reaction. Taking into consideration CO_2 photoreduction reaction specifically, studies on alloyed metal catalysts have not been reported yet. We intend to design an alloy catalyst nanomaterial that is inexpensive, possesses enhanced catalytic activity, and shows high product selectivity for CO_2 photoreduction.

1.2.4 Geometrical structure

The designing of geometric structure of a catalyst nanomaterials is a crucial element that determines overall catalytic behavior of the catalyst. For example, Kamat's

10

research group have synthesized catalysts composed of metal@TiO_2 core-shell and metal/TiO_2 sandwich structures and found that a metal@TiO_2 core-shell structure nanoparticles were less photo-active than a metal-TiO_2 sandwich structure[63]. It was postulated that when a metal is in contact with a semiconductor, a charge separation occurs during photocatalytic reactions. In both cases of metallic-core and the metallic-sandwich composites, the metal traps the photo-excited electrons during the charge separation. However, the charge accumulates in a core-shell structure over time without being discharged into an electrolyte, which reduces the overall reactivity. Having a metal oxide shell is not always a disadvantage. For instance, a shell structure may be useful in other cases, to protect an inner metal core from oxidation during catalysis, which cannot be realized in sandwich structure[64]. Cheng and coworkers have shown that oxidation of Fe was reduced by having an inert SiO_2 shell around the nanoparticle surface and preserved the magnetic properties[65]. Therefore, the design of the geometric structure of a nanomaterial is a specific purpose reaction and that particular reaction.

In the field of photocatalysis, the use of plasmonic metals as catalysts is gaining interests. Awazu and coworkers have found that there was 8-fold increase in the photocatalytic degradation of methylene blue by using plasmonic Ag nanoparticles embedded inside TiO_2 semiconductor[64]. Akimov et al.[66] and Hägglund et al.[67] have designed thin-film solar cells with silver (Ag) nanoparticles as sub-wavelength light trapping sites to increase the photocurrent generated in the solar cells. An and coworkers have used Ag and silver chloride (AgCl) hybrid nanoparticles that exhibited high catalytic performance under visible light and sunlight for decomposing organics[68]. Linic research group has also reported that silver nanostructures drive catalytic reactions

11

such as ethylene epoxidation, CO oxidation, ammonia (NH_3) oxidation and degradation of methylene blue[69-71].

Silver and other plasmonic nanoparticles improve catalytic activity by the phenomenon of localized surface plasmon resonance (SPR), which is caused when there is a frequency match between the vibrations of conduction electrons of the metal with the frequency of incident light. In this dissertation, we will describe the design of a plasmonic Ag nanoparticle to perform CO_2 photoreduction reaction compared to previous studies that studied only photo-oxidation reactions. The SPR effect produced in the plasmonic nanoparticles will help boost electron-hole pair generations in TiO_2 photocatalyst. In order to avoid discharge of photo-electrons from TiO_2, design considerations such as creating an inert shell around Ag nanoparticles will be considered. The colloidal techniques used in this dissertation also allow optimization of the shell thickness of the insulating spacer to effectively reduce discharging of photo-excited charges with minimum dampening of SPR effect.

1.3 Research focus: Engineering colloidal nanomaterial for catalysis

Catalytic reactions can be influenced greatly by nanomaterial features such as size, surface area, elemental composition and geometric structure as detailed in the previous sections. In our research, colloidal methods have been used to synthesize nanomaterials with precise control of the key nanomaterial features to allow a systematic understanding of how these key features influence catalytic reactions of our interest. Other common methods of nanomaterial preparation are gas condensation, chemical vapor deposition, mechanical attrition and electrodeposition methods. Gas condensation and chemical vapor deposition methods involve vaporizing a metal or a non-metallic

12

material and condensing the precursor material on a substrate. These methods are very slow, energy intensive, and limited by material precursors that cannot be vaporized easily. Lithography or focused ion beams have been used to deposit or remove material for creating nano-features on a surface. High energy ball mills use mechanical attrition to crush down larger particles to smaller sizes. This technique has also recently received attention in the field of temperature controlled mechanical alloying. For example, it is not otherwise possible to alloy aluminum (Al) and Ta due to their different melting temperatures[72]. However, this process also requires high energy to operate and the polydispersity in size of the alloys is one of the major drawbacks. Electrodeposition methods are used to create uniform coating and high purity nanoporous materials. But this method is also a slow and expensive process. On the other hand, colloidal techniques are economical and require less sophisticated setup. Therefore, colloid methods can be more promising for commercial industrial application because of the convenience and scalability.

Below, we broadly describe the scope of this research project to study the influence of nanomaterial features on catalytic reactions. Some details of the catalyst nanomaterials and the catalytic reactions used are also mentioned.

Firstly, we have studied the role of nanoparticle size of cobalt oxide for CO oxidation reaction. Cobalt metal is comparatively cheaper than the other noble metal counterparts. Xie and coworkers[73] have shown recently the high activity of nano-rod shaped cobalt oxide for CO oxidation reaction that suggests low coordination cobalt oxide sites play an important role in catalysis. We have synthesized cobalt oxide nanoparticles of discrete sizes (1-14nm) using colloidal thermal decomposition technique

13

to vary the percentage of low coordinated sites as nanoparticle size was changed. Surface modified SiO_2 supports were prepared and cobalt oxide nanoparticles were decorated on SiO_2 via self-assembly techniques. These Co/SiO_2 nanocomposites were then used to study the CO oxidation reaction. Advanced *in-situ* FTIR tools were used to measure both surface species and bulk gases during the reaction to relate the impact of cobalt nanoparticle size with CO oxidation activation energies.

Secondly, colloidal techniques were used to synthesize TiO_2 photocatalyst nanoshells with high surface area to convert CO_2 to hydrocarbon fuels. Other conventional methods such as layer-by-layer deposition or precipitation deposition methods have been shown to deposit TiO_2 shells on SiO_2 supports. However these conventional methods require multiple deposition steps to create a thick enough shell. Our strategy to deposit TiO_2 on SiO_2 using a polymer poly(NIPAAM)-SiO_2 core-shell template colloids is a quick one-step process where shell thickness is determined by the thickness of polymer template. During the calcination step the polymer template was burned off leaving behind nanoshells of crystalline TiO_2 with high surface roughness.

Thirdly, we have prepared bimetallic Ag-Pt nanoparticles to deposit on TiO_2 to improve catalytic selectivity of products during CO_2 photoreduction reaction. Pt is a traditionally used metal that has been used from the past as a catalyst for a multitude of reactions as well as for CO_2 photoreduction as a co-catalyst deposited on TiO_2. [50, 74] When a metal co-catalyst such as Pt is in contact with a semiconductor, it allows easy and quick transfer of photo-excited charges from TiO_2 to the electrolyte. [63, 74-82] Pt is an expensive metal and has poor product selectivity. Our focus was to integrate catalytic properties of Pt with a relatively cheaper metal Ag for photocatalytic application.

14

According to the APMEX Inc, the average value of Ag is ~50 times less that Pt[83]. When Ag and Pt metals are compared, the Ag nanoparticles possess a strong optical absorbance band in the UV-Vis region while Pt nanoparticles have no such optical behavior. Using colloidal techniques we have synthesized Ag-Pt bimetallic nanoparticles that showed high catalytic activity and product selectivity for photocatalytic reactions. The new bimetallic nanoparticle is an improved photocatalyst since it encompasses catalytic properties of both Ag and Pt elements.

Finally, we have designed core-shell Ag@SiO_2 structured nanoparticles with surface plasmon characteristics. These core-shell nanoparticles induce surface plasmon resonance effect upon light irradiation causing an electric field enhancement near the vicinity of the nanoparticles. This energy was conveyed for electron-hole pair generation in the TiO_2 during photocatalytic reduction of CO_2. The reason for choosing Ag was based on the fact that the plasmon band was near the wavelength of light that excites TiO_2. By creating an insulating shell around the Ag core, the discharge of photo-excited charges from TiO_2 surface to Ag core was avoided.

The organization of this dissertation describing how nanoparticle size, surface area, elemental composition and geometric structure were probed to study the role of these features on catalytic reactivity is as follows. Chapter 2 deals with the synthesis of cobalt oxide (CoO) nanoparticles, surface modification of SiO_2 supports and understanding the role of cobalt oxide nanoparticle size on CO oxidation reaction. Use of colloidal and self-assembly routes for the synthesis is provided in the second chapter. Chapter 3 details the preparation of TiO_2 nanoshells with high surface area and its utilization for CO_2 photoreduction reaction. Chapter 4 describes the preparation of

15

Ag@SiO$_2$ core-shell plasmonic nanoparticles and co-catalyst Ag-Pt nanoparticles for improvement of CO$_2$ photoreduction activity and product selectivity. Finally, Chapter 5 summarizes the various synthesis and catalytic reactions on nanoscale materials as well as provides some insights on future prospects and recommendations.

16
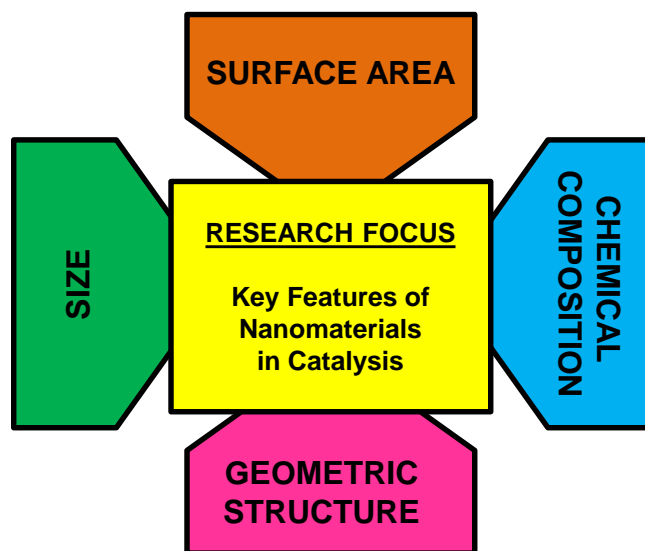
Figure 1.01. Key features of nanomaterials in catalysis

CHAPTER 2: COLLOIDAL COBALT OXIDE AND SILICA NANOCOMPOSITES FOR CARBON MONOXIDE OXIDATION: IMPACT OF SIZE

In this chapter, a detailed description is given on synthesis, characterization and CO oxidation reaction studies of CoO/SiO_2 nanocomposites. Our objective was to investigate the effect of CoO nanoparticle size for carbon monoxide oxidation reaction using *in-situ* FTIR spectrophotometry. CoO nanoparticles were immobilized on the surface of Stöber SiO_2 catalyst support by surface functionalization methods to create a model catalyst. A host of characterization techniques were used to completely understand the physicochemical and catalytic properties. Microscopy, spectroscopy, and scattering techniques were used to gain insight into the particle size, shape, crystallinity, and chemical functional groups present. Temperature programmed *in-situ* surface IR experiments allowed us to measure activation energies for CO oxidation elementary steps and understand the role of nanoparticle size on kinetic parameters.

2.1 Experimental details and material characterization

2.1.1 Synthesis of colloidal SiO_2 support

To study the effect of cobalt oxide nanoparticle size for CO oxidation, nanoparticles were supported on SiO_2 substrate. A non-porous SiO_2 colloidal support was chosen rather than a porous support structure. The primary reason for choosing a non-porous support is because porous catalyst support structures becomes a barrier for the transfer of reactant/product species from the catalyst surface into the gas phase. [84]

18

Since repeated adsorption and desorption of radicals may take place within the pores, the use of a porous supported catalyst becomes more complex and not ideal for fundamental studies of catalytic reactions such as one studied here.

Sub-micron non-porous spherical SiO_2 colloids were synthesized using a modified Stöber process[85]. The synthesis procedure is well documented in literature. Typically, 3.14 ml of 28-30 wt% NH_4OH was added to an ethanol-water mixture and equilibrated for 30 min. An aliquot of 6ml TEOS was added and stirred for 6 hours at room temperature to yield monodisperse sub-micron SiO_2 particles. The NH_4OH in solution helps to control the charge of the SiO_2 colloids. The SiO_2 colloid solution was purified by centrifuging the solution at 7,000 rpm for 30 minutes and the resulting residue was washed repeatedly with water. The particles were dried overnight under vacuum at room temperature. Stöber SiO_2 particles of different sizes of were prepared similarly by varying the reaction conditions such as concentration of ethanol or reaction temperature.

2.1.2 Surface modification of colloidal SiO_2

The strategy to immobilize cobalt oxide nanoparticles was by tailoring the surface of Stöber SiO_2 with chemical functional groups. In surface functionalization steps, the surface –OH groups on Stöber SiO_2 were covalently modified by small molecule ligands or oligomers, that contain different functional groups namely, carboxyl (–C=O) or amine (–NH_2) groups. Specifically, compounds such as methacryloxypropyltrimethoxysilane (MPS), aminopropyl dimethoxysilaneAPDMS, poly(acrylic acid) (PAA) and Acetoacetoxyethyl methacrylate (AAEM) were used for grafting.

19

MPS was added to a colloidal (6 wt%) Stöber SiO_2 solution dispersed in 70% ethanol in water and stirred for approximately 12 hours. The solution was held at $80^{\circ}C$ for 1 hour to promote covalent bonding of the organosilane molecules to the surface of the silica nanoparticles[86, 87]. The amount of MPS ligand added was 50% in excess of that required for full coverage. The estimate of full surface coverage was based on 25 $Å^2$ per molecule of MPS on the SiO_2 surface. The colloidal solution was purified in a similar manner to Stöber SiO_2 colloids. MPS functionalized silica particles prepared by above approach were denoted as MPS-SiO_2. Similarly, amine (-NH_2) terminated surfaces were obtained by adding APDMS to a dispersion of Stöber SiO_2 in toluene. The dispersion was continuously stirred for 4 hours under N_2 atmosphere at room temperature. The colloidal solution was purified in a similar manner to Stöber SiO_2 colloids and the particles were denoted as APDMS-SiO_2.

Grafting of oligomers was performed by the polymerization of a monomeric solution (acrylic acid or AAEM) in the presence of the MPS, a coupling agent to form siloxane terminated oligomers[88-90]. Need typical conditions. SiO_2 colloids were then added to the oligomeric solution to bridge the oligomers on SiO_2 surface through the siloxane bonds of MPS. Typically, a colloidal solution of 6 wt% of MPS-SiO_2 in water and 0.5 mmol AAEM monomer concentration was mixed for 5-10 min. The solution was heated to 70°C and the polymerization was initiated by 0.6 wt% KPS. The polymerization reaction was continued for 12 hours at 70°C. The solution was cooled and the particles were purified by centrifugation and washing cycles with water. The samples were dried and denoted as PAAEM-SiO_2. PAA-SiO_2 particles were synthesized in a similar manner to AAEM grafting method.

20

2.1.3 Synthesis of CoO nanoparticles: Control of nanoparticle size

CoO nanoparticles with high crystallinity and narrow size distributions can be successfully prepared by following certain strategies learnt from the past prototypical systems. In the past, catalysts have been synthesized by incipient wetness impregnation methods for obtaining pure catalyst composites[91-94]. But this method lacks control of particle size in the nanoscale regime. Other methods for preparing well-controlled nanoparticles such as laser ablation [95-102], thermal plasma [103], high pressure sputtering [104], high current pulsation [105], ion beam [106], supercritical fluid assisted [107-110], and high energy ball-milling [111-114] are energy intensive and expensive for large scale production of nanoparticles. Colloidal techniques such as inverse micelle [115-117], sonochemical [118-122], and thermal decomposition [123-126] provide alternative and inexpensive ways to synthesize nanoparticles in large scale. We describe here the experimental details of synthesis of CoO nanoparticles of discrete sizes via thermal decomposition technique.

For thermal decomposition method, a cobalt carbonyl precursor was allowed to decompose in an organic solvent maintained at a temperature approximately equal to its boiling point. Typically, a ~0.25gm of $Co_2(CO)_8$ was mixed into 60 ml toluene and heated to 110°C in the presence of a surfactant AOT (sodium bis(2-ethylhexyl) sulfosuccinate). The concentration of AOT was based on a molar ratio of cobalt precursor to AOT equal to 0.2. Additional $Co_2(CO)_8$ was added into the solution at every 3 hour intervals. The solution color turned from dark orange to black once nucleation of nanoparticles was initiated. After 3 hours, prior to adding additional cobalt precursor, 3-4 ml of sample were collected and stored. AOT surfactant prevented nanoparticle aggregation by lowering metal-to-metal surface interactions through charge transfer. Nucleation and growth

21

kinetics were controlled by slow additions of cobalt precursor every 3 hours to obtain monodisperse cobalt nanoparticles of different sizes[126]. After successive additions of cobalt carbonyl, the final molar ratio of cobalt precursor to AOT surfactant was approximately equal to 10. In the case of preparing cobalt nanoparticles with two surfactants, a combination of AOT and BUA surfactants was used. Cobalt nanoparticles when exposed to ambient conditions oxidized to cobalt oxide due to their reactivity to air. XRD characterization techniques described below were used to confirm that the type of oxide was CoO.

2.1.4 Preparation of CoO/SiO$_2$ nanocomposites

In general, conventional methods such as such as incipient wetness impregnation (IWI) methods have been used to obtain high metal catalyst loading on oxide supports for higher catalytic reactivity[127-129]. For an IWI method, a metal precursor is reduced from a precursor salt to metallic catalyst via calcination at very high temperatures. However, such catalysts often have lower dispersion and wider distribution of the particle sizes[130]. Another drawback of this approach is that calcination step results in unwanted cobalt-silicate formation thereby reducing the catalyst quality and purity. Our strategy was to prepare colloidal solutions of CoO nanoparticles and surface-modified SiO$_2$ to two containers separately and then mix the two solutions to obtain CoO nanoparticles decorated on the surface of the modified-SiO$_2$ via self-assembly. By this approach, we intended to avoid cobalt-silicate formation in the synthesis step.

CoO/SiO$_2$ nanocomposites were prepared by mixing together the colloidal solutions of cobalt nanoparticles and surface modified SiO$_2$. Typically, ~1gm of surface

22

functionalized silica particles MPS-SiO$_2$, PAA-SiO$_2$ and PAAEM-SiO$_2$ were dispersed in toluene in three different beakers. 2-3 ml of CoO nanoparticle solution prepared using AOT as surfactant was then added to each beaker. CoO prepared from AOT and BUA surfactants were mixed with APDMS-SiO$_2$ into a fourth beaker. The nanoparticles of CoO were immobilized on the surface of the SiO$_2$ support by self-assembly. After few hours, CoO/SiO$_2$ nanocomposites settled to the bottom, whereas the excess CoO nanoparticles that did not take part in self-assembly remained in the supernatant. The CoO/SiO$_2$ residue was separated from free CoO nanoparticles in the supernatant by decantation. However, one disadvantage of this method is that it is difficult to quantify the amount of Co immobilization. An alternative way to quantify would be to measure cobalt indirectly using ICP-MS characterization. The final residue was dried at 50℃ in the vacuum oven for ~1day.

2.2 Material characterization techniques

A host of instrumentation tools were utilized to understand the physico-chemical properties of materials. TEM measurements were performed on a FEI Morgagni 268D where samples were prepared by drying a drop of the colloidal solution on a carbon-support film TEM grid (Electron Microscopy Sciences, PA). SEM samples were prepared by drying the colloid on a double sided adhesive carbon tape fixed on a specimen stub. Hitachi S800 with a field emission electron gun was used to analyze the surface topography of catalyst supports and composites. FTIR measurements were done using a Nicolet Magna-IR 860 spectrometer to identify the bonding peaks. Hydrodynamic diameter and polydispersity of particles were estimated from DLS technique (Malvern Nano-S Zetasizer). Philips X'pert materials research diffractometer was used to analyze the crystal structure of the cobalt oxide nanoparticles. Samples for XRD were mounted

23

on a Si zero-background plate using an adhesive tape and covering the sample with Parafilm® to avoid spillage during measurements. Temperature programmed reduction method was used to measure the temperature at which cobalt oxides reduced by hydrogen gas to metallic cobalt using Autosorb-1® from Quantachrome Instruments.

2.3 CO oxidation reaction studies using in-situ FTIR spectroscopy

CO oxidation reaction was studied in AABSPEC #2000A, a stainless steel reactor equipped with zinc selenide (ZnSe) windows for in situ FTIR spectroscopy measurements on a Bio-RAD Excalibur FTS3000. CoO/SiO_2 nanocomposites pressed into pellets were placed along the IR beam on a programmable hot finger inserted into the FTIR reactor. Actual temperatures were monitored by an external thermocouple. The chamber was preheated in-situ to 140˚C for 30mins to remove any water vapor and then cooled back to room temperature under a 30 sccm N_2 flow. A gas mixture of CO (10 sccm) and compressed dry air (20 sccm) were introduced using mass flow controllers. Both inlet and outlet valves were closed after 10-15 min of steady flow of gases. A new background signal was collected against which further spectra were compared with. Temperature programmed reactions were carried out by increasing the temperature from room temperature to 475˚C at a constant heating ramps set at 10, 7.5, 4.5 and 2˚C/min. The actual temperature ramps were measured as 9.7, 7.2, 4.4 and 1.9˚C/min using a thermocouple attached to the transmission probe. FTIR spectra were collected in transmission mode at regular intervals of time during the temperature programmed reaction.

24

2.4 Results and discussion

Physical and chemical properties of CoO nanoparticles, colloidal SiO_2 and CoO/SiO_2 nanocomposites were analyzed using various characterization techniques. TEM, SEM and DLS were used to estimate the particle size shape and morphology. FTIR spectroscopy was used to infer the presence of chemical groups on the surface of the SiO_2 support material. Crystallinity of CoO nanoparticles was examined using XRD spectroscopy. TPR techniques were used to observe reducibility of cobalt oxides to metallic cobalt nanoparticles. CO oxidation results obtained from *in-situ* FTIR studies were analyzed to calculate the activation energies for CO oxidation reaction for all nanoparticle sizes.

2.4.1 Analysis of SiO_2 supports using DLS, TEM, SEM and FTIR

In the Stöber method, the solution turned turbid within a few minutes upon TEOS addition which indicated the nucleation of SiO_2. The SiO_2 size was dependent on reaction conditions such as nature of alcohol, alcohol-water ratio, reaction temperature and concentration of NH_4OH[131-134]. Table 2.1 summarizes different sizes of SiO_2 colloids obtained by varying ethanol-to-water volume ratio or reaction temperature. The size was almost halved when temperature was raised to 40 C in the case where ethanol to water volume ratio was 100:8. The size analysis plot of SiO_2 of different sizes obtained from DLS results is plotted in figure 2.1. TEM and SEM images of Stöber SiO_2 shown in figures 2.2 and 2.3 reveal that the particles are spherical in shape. Surface modification of SiO_2 particles was verified using FTIR methods. The presence of chemical groups after surface modification using ligands or oligomers was inferred from FTIR spectroscopic measurements as shown in figure 2.4. The absorbance peak for –OH stretching at 1400 cm^{-1} was removed when the surface silanol groups of Stöber SiO_2

25

were replaced with organosilanes. The increase in (–C=O) peak intensity at 1723cm^{-1} was observed from MPS and PAA grafting.

2.4.2 DLS, TEM and XRD of CoO nanoparticles

CoO colloids with discrete nanoparticle sizes were prepared by thermal decomposition technique. Figure 2.5 shows the size distribution of CoO nanoparticle samples obtained from DLS analysis. TEM images of two samples of CoO nanoparticles with size average of 2 nm and 6nm are shown Figure 2.6 and 2.7. The aggregation of larger nanoparticles of CoO nanoparticles may have been caused due to low surfactant concentration and high magnetic field interactions[135]. A surfactant helps to overcome metal-metal attractive van der Waals and magnetic dipole-dipole forces. [125, 126] The crystallinity of CoO nanoparticles prepared using decomposition technique was studied using XRD and high resolution TEM. The X-ray diffraction patterns of CoO nanoparticles are shown in figure 2.8. The peak positions were common for both samples of CoO prepared from single and two surfactants except for the peak at 60 (2θ). The appearance of this small broad peak suggests that CoO nanoparticles prepared from two surfactants have slightly different crystalline facets. This phenomenon has been also observed in other literature reports where it was found that changing the type of surfactants leads to changes in the shapes or sizes of nanoparticles with altered crystalline facet orientations[136, 137]. The XRD spectral lines were used to verify that the cobalt oxide synthesized was CoO in comparison to the other commonly synthesized oxide, Co_3O_4[138-140]. Using high-resolution TEM, the distances between the crystal planes were measured as shown in figure 2.9 to obtain the mean lattice spacing of 2.12Å, which was consistent with the past literature reports[141].

26

2.4.3 TEM and TPR of CoO/SiO$_2$ nanocomposites

The self-assembly of CoO nanoparticles on SiO$_2$ functionalized with different functional groups were verified using TEM. TEM of surface modified SiO$_2$ support without cobalt nanoparticled showed that the surface topography of SiO$_2$ was smooth in comparison with the CoO/SiO$_2$ nanocomposites. This feature was used as a quick diagnostic to identify the presence of cobalt nanoparticles on the SiO$_2$ surface. Carbonyl functional groups in MPS, AAEM or PAA and, amine functional groups in APDMS were target sites for CoO nanoparticles for self-assembly since carbonyl and amine groups were known to form physisorbed bonds to metal surfaces[142-145]. Figure 2.10, 2.11 and 2.12 shows the self-assembly of 14nm CoO on carbonyl functionalized MPS-, AAEM- and PAA-SiO$_2$ supports. There was no self-assembly of CoO with amine functionalized APDMS-SiO$_2$, however, CoO nanoparticles prepared from two surfactants showed some interaction as shown in figure 2.13. In a two-surfactant cobalt colloidal system, the carboxylic acid group of the second surfactant BUA adsorbs strongly to the nanoparticles of cobalt with the terminal Br group pointing outwards. The hydrogen bonding between the -NH$_2$ group of the aminated silica support and the terminal bromine of BUA contributes to the anchoring of cobalt nanoparticles on the surface[146]. Low resolution and high resolution TEM of CoO/MPS-SiO$_2$ are shown in figure 2.14 and 2.15. From the high resolution TEM image, we can distinguish the crytalline CoO metallic features from amorphous SiO$_2$ support which provides us with a qualitative verification that the particles on SiO$_2$ was indeed CoO nanoparticles.

TPR method was used to measure the temperature at which CoO was reduced to cobalt metal. In general for all metal oxides, the nature of reducibility is found to be a function of size and metal-support interactions[147-150]. FTIR spectra of samples before

27

and after TPR testing was taken to understand the changes in the nanocomposites when subjected to high temperature treatments during TPR. The results are described later in this section. Figure 2.16 details the TPR profiles of CoO/MPS-SiO$_2$ composites of different CoO sizes. In the figure, we observe multiple peaks for 14nm CoO nanocomposites and single peaks for 6, 2 and 1nm CoO nanocomposites. The major peak at the lowest temperature for each samples is the temperature at which CoO reduces to Co metal. The subsequent peaks at higher temperatures are a result of metal-support interations. When an oxide support is present in close proximity to an oxide metal, the reduction temperature shifts to higher temperatures[151]. In figure 2.16 we can see a trend in the nanoparticle size effect for CoO with respect to TPR peak positions. The nanocomposites with smaller CoO nanoparticles reduces at higher temperatures since they have a higher interaction with the SiO$_2$ support. The nanocomposites with larger CoO nanoparticles, such as CoO nanoparticles of 14nm have lower metal-support interations that allow reduction to occur at lower temperatures. The subsequent peaks for 14nm CoO nanocomposites may be due to small percentage of smaller sized CoO nanoparticles in the sample. After the TPR run, all the nanocomposite samples were exposed to air and TPR testing was performed for a second time with the same composites. Cobalt is highly reactive to ambient air and undergoes oxidation. The second TPR would allow us to understand the reproducibility of CoO nanoparticles for hydrogen reduction. Figure 2.17 depicts the TPR profile for the second reduction cycle. Comparing the two TRP cycles, the reduction temperature for nanocomposites with 14nm CoO nanoparticles have a reduction temperature at 240°C, which is lower than the reduction temperature of 280°C observed during the first cycle. In addition, the reduction peak intensities have significantly dropped for all nanocomposites, significantly for the nanocomposites of 6, 2 and 1nm CoO nanparticles.

28

This suggests that during TPR, there may be aggregation of nanoparticles to form larger sized particles.

To further study the effect of structural changes of CoO/SiO$_2$ nanocomposites after high temperature TPR treatment, FTIR spectra of nanocomposites with 6nm CoO nanoparticles before and after the TPR run were collected as shown in figures 2.18 and 2.19. The FTIR spectra in figure 2.18 shows that the organic ligands were removed when composites were heated to 600°C indicated by the disappearance of 2982 cm^{-1} peak which is a characteristic band for C-H bonds[152]. Figure 2.19 shows that the peak that corresponds to Si-O-Si band at 1100 cm^{-1} does not shift, which suggests the absence of cobalt silicate (Co-O-Si) formation[153]. Cobalt silicate is an inactive material that is usually formed while preparing cobalt-metal and SiO$_2$-support based catalysts[154-157]. Kogelbauer et al.[158] have proposed that in the presence of a hydrogen gas and water, cobalt metal in contact with SiO$_2$ have higher chances of forming cobalt silicates. Coulter and Sault[159] as well as Van Steen and coworkers[160] have postulated that even surface silanol groups present in SiO$_2$ can react with aqueous cobalt complexes to form cobalt silicates. With the current characterizations from FTIR, it is still not clear how the CoO/SiO$_2$ nanocomposites show lower reducibility during the second TPR run. Other characterizations such as XRD and EXAPS should be done to further understand this behavior more in detail[161].

2.4.4 Role of CoO nanoparticle size on CO oxidation reaction

When CO is introduced into the reactor, bands at 2058, 2140 and 2170 cm^{-1} were observed. The figure 2.20 depicts the spectrum obtained when CO was introduced into the reactor for CoO/SiO$_2$ with CoO nanoparticle size of 2nm. The peak at 2058 cm^{-1}

29

corresponds to the linear adsorption of CO gas on CoO surface[162] and the vibrational frequencies of CO in bulk gaseous phase were seen at 2140 cm^{-1} and 2170 cm^{-1}. The appearance of 1630 cm^{-1} peak suggests the presence of small amounts of water vapor. This may be due to inherent trace water vapor present in the gas lines or storage cylinders. After flowing CO and air for 10-15mins, both the exit and inlet valves were closed. Spectra were collected as temperature was ramped from room temperature to 475°C at various heating rates as shown in figure 2.21. There was a decreasing trend in the peaks intensities for 2058, 2140 and 2170 cm^{-1} bands and appearance of new two bands at 2350 cm^{-1} and 2342cm^{-1} indicated the formation of CO_2 gas.

We proposed a reaction mechanism for CO oxidation reaction on CoO surface based on *in-situ* FTIR analysis. The experimental results were used to calculate the activation energies for the proposed reaction intermediate steps. The proposed reaction is as follows:

$$CO + O_2 \xrightarrow{step-1} [CO - O_2]^* \xrightarrow{step-2} CO_2 + byproducts$$
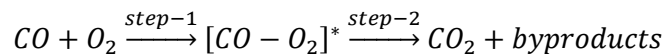
Adsorbed CO molecule reacts with O_2 from air to form an intermediate denoted as step-1. This intermediate molecule rearranges itself on CoO nanoparticle surface and desorbs to form CO_2 molecule, denoted above as step-2. Activation energies for step-1 and step-2 were estimated experimentally using *in-situ* FTIR studies.

Activation energy for step-1 was found from FTIR spectra collected for all experiments at various heating rates. Plots of 2058cm^{-1} peak height vs. temperature for samples of different CoO sizes are shown in figures 2.22, 2.23, 2.24 and 2.25. The peak height reduced as temperature was raised and began to plateau at a particular temperature T' as depicted in the above mentioned figures. This plateau-onset

30

temperature T' and the corresponding heating rates, ψ were then incorporated into an equation for calculating the activation energies for step-1 for different CoO sized nanocomposites. The model equation originally developed by Kissinger[163] and further extended by others [164, 165] uses an Arrhenius equation to find activation energies from temperature programmed studies. The linear equation that correlated ramp rate ψ, and the plateau-onset temperature T' was obtained as follows:

$$\ln\left(\frac{\psi}{T'^2}\right) = \frac{-E}{RT'} - \ln\left(\frac{AR}{E}\right) + C$$

where E is the activation energy for step-1, R is the universal gas constant, and A & C are other constants. Activation energy of step-1 was calculated from the slope $-E/_R$ obtained from the linear plot of $\ln\left(\frac{\psi}{T'^2}\right)$ vs. $\left(\frac{1}{T'}\right)$. A detailed derivation for these equations is provided below.

The derivation for Kissinger's equation is as follows:

$$r = d\alpha/_{dt} = k_1(T)f(\alpha)f'([CO])$$

(1)

where α is the degree of conversion of a catalyst, T the temperature, f(α) the reaction mechanism function and the concentration of gas phase reactants represented as [CO]. Under differential conditions during a temperature programmed analysis with a linear heating rate, $\psi = dT/_{dt}$, the gas phase dependent term is approximately a constant.

Therefore, equation (1) can be re-written as

$$d\alpha/_{dT} = \frac{1}{\psi}k(T)f(\alpha)$$

(2)

31

www.manaraa.com

where k is the rate constant given by the Arrhenius equation.

$$k(T) = Ae^{(-E/RT)}$$

(3)

Combining equations (2) and (3), we get

$$d\alpha/dT = \frac{A}{\psi}e^{(-E/RT)}f(\alpha)$$

(4)

The peak height profiles shown in the figures 2.22-2.25 can then be represented in the form of equation (4) and the plateau-onset temperature was found by differentiating equating the equation to zero as shown below:

$$\left(\frac{d}{dT}\left(d\alpha/dT\right)\right)_{T'} = 0$$

$$\left(\frac{d}{dT'}\left(\frac{A}{\psi}e^{(-E/RT')}f(\alpha)\right)\right)_{T'} = 0$$

$$\left\{\frac{A}{\psi}e^{(-E/RT')}\frac{d}{dT'}[f(\alpha)] + f(\alpha)\frac{d}{dT'}\left[e^{(-E/RT')}\right]\right\} = 0$$

$$\frac{A}{\psi}e^{(-E/RT')}\left[\frac{d\alpha}{dT'}\frac{df(\alpha)}{d\alpha}\right] + f(\alpha)\frac{A}{\psi}\left[e^{(-E/RT')}\right]\left(\frac{E}{RT'^2}\right) = 0$$

$$\frac{A}{\psi}e^{(-E/RT')}\left[\frac{d\alpha}{dT'}\frac{df(\alpha)}{d\alpha}\right] + f(\alpha)\frac{d\alpha}{dT'}\left(\frac{E}{RT'^2}\right) = 0$$

$$\frac{d\alpha}{dT'}\left\{\frac{A}{\psi}e^{(-E/RT')}\frac{df(\alpha)}{d\alpha} + \frac{E}{RT'^2}\right\} = 0$$

Since, $\frac{d\alpha}{dT'} \neq 0$, the above equation reduces to

$$\frac{E}{AR}\frac{\psi}{T'^2} = -e^{(-E/RT')}\frac{df(\alpha)}{d\alpha}\bigg|_{T'}$$

32

$$\ln\left(\frac{\psi}{T'^2}\right) + \ln\left(\frac{E}{AR}\right) = \frac{-E}{RT'} + \ln\left(-\frac{df(\alpha)}{d\alpha}\right)_{T'}$$

Assuming that $f(\alpha)$, the reaction model, and $\alpha_{T=T\max}$ are independent of the heating rate, the final expression is:

$$\ln\left(\frac{\psi}{T'^2}\right) = \frac{-E}{RT'} - \ln\left(\frac{AR}{E}\right) + C$$

Therefore, activation energy for step-1 can be obtained from the slope of $\ln\left(\frac{\psi}{T'^2}\right)$ vs. $\left(\frac{1}{T'}\right)$

The Kissinger plots obtained for all nanocomposites with different CoO sized are depicted in figure 2.26. It was found that activation energies for step-1 followed an increasing trend as nanoparticle size increases. For composites with 1 and 2nm sized CoO nanoparticles, the T' values obtained from the slowest heating rate, i.e., 1.9 K/min were not included in the activation energy calculations due to large deviation from linearity. This might be due to surface reconstruction during a prolong exposure to CO gas or aggregation of smaller nanoparticles into bigger sizes. Surface reconstruction behavior of a metal surface such as cobalt metal has been observed due to an adsorbing CO gas. [166, 167]

Activation energy for step-2 was found based on the CO_2 evolution profile obtained from *in-situ* FTIR analysis. Figure 2.27 depicts moles of CO_2 produced during the analysis of nanocomposites with different CoO sizes for heating rate of 9.7 C/min. This data was fitted to a rate equation to calculate the activation energy of step-2. The details of the derivation of the rate equation are as follows:

33

The rate of CO_2 formation can be written as

$$\frac{d(CO_2)}{dt} = A \exp\left(-E/RT\right) g(CO_2)$$

where, $A \exp\left(-E/RT\right)$ are the kinetic constant and $g(CO_2)$ the kinetic model for the reaction. For an experiment taking place under a linear heating rate ψ, the temperature-time relationship $T = T_0 + \psi t$ can be used to obtain

$$\int_{C_o}^{C} \frac{d(CO_2)}{g(CO_2)} = \int_{T_o}^{T} \frac{A \exp\left(-E/RT\right) dT}{\psi}$$

Assuming a power law model equation $g(CO_2) = [CO]^n$ for the chemical reaction with the order of reaction n=1, we get

$$\frac{1}{\left[1 - \dfrac{CO_2(t)}{CO(t_o)}\right]} = \frac{AT_o}{\psi} \int_{T_o}^{T} A \exp\left(-E/RT\right) dT$$

The right hand side of this equation was obtained from the experimental values of CO_2 at a particular time t. The left hand side of the above equation is an integral function that was fitted to the experimental data. The data from CO_2 formation was then used in the regressions analysis by keeping E and A as fitting parameters. This right hand side of the equation was rewritten as

$$f = \propto \cdot I(A', \theta)$$

where, $\propto = \dfrac{AT_o}{\psi}$, $A' = \dfrac{E}{RT_o}$, $\theta = \dfrac{T}{T_o}$ and I is the integral. The integral function was approximated by using relationships developed by Coats and Redfern [168, 169] to:

$$I \cong \frac{\exp(-A')}{(A' + 2)} \left\{ \theta^2 \frac{(A' + 2)}{(A' + 2\theta)} \exp\left(-\frac{A'(1 - \theta)}{\theta}\right) - 1 \right\}$$

34

From regression analysis, E values for nanocomposites of different CoO nanoparticle sizes were obtained. Figure 2.28 summarizes the relationship between CoO nanoparticle size and activation energies of step-1 and step-2 for CO oxidation reaction. Smaller nanoparticles have lower activation energies demonstrating the impact of nanoparticles for catalytic applications. Other studies have utilized metal flat surfaces [170, 171] or metal clusters of Fe with 55 atoms[172] that energy barriers are lower on a metal sites with low coordination numbers.

We have found that the activation energies to decrease as nanoparticle size decreases for the CO oxidation reaction that was investigated. The reduction in activation energies for smaller particles may be due to the percentage of low coordinated atoms present in smaller nanoparticles. The number of low-coordinated sites and the energy associated with reaction steps are both influenced by the size.[173] Therefore, particle size plays an important role in determining catalyst activity, especially at the nanometer scale. To our knowledge, this is for the first time cobalt oxide nanoparticles have been studied to understand the role of size in CO oxidation reaction. The experimental results have also provided a valuable context for computational calculation of reaction energetics in CO oxidation using DFT approaches (PhD dissertation by Ms. Nianthrini Balakrishnan). Computational calculations were used to support the activation values predicted by experimental results. Computational simulations also provide details about the reaction intermediates and the probable orientation of intermediate molecules proposed by the experiments.

2.5 Summary

CoO nanoparticles of discrete sizes were prepared via colloidal synthesis. The surface of the SiO_2 support surface was modified using ligands or oligomers to immobilize the CoO nanoparticles on the surface of the support. The weak interaction between the functional groups on the support and the CoO nanoparticles lead to anchoring of nanoparticles on the support surface. The self-assembly of CoO nanoparticles was observed from TEM images. Characterizations were performed to understand the physical and chemical properties of CoO/SiO_2 nanocomposites. *In-situ* FTIR studies capable of analyzing adsorbed gas species on the catalyst surfaces were used. The activation energies for CO oxidation reaction and their impact on CoO nanoparticle size were experimentally estimated.

Table 2.1. Stöber SiO_2 colloids of different sizes

Volume ratio of Ethanol to Water	Temperature (˚C)	Diameter (nm) [a]
100:27	25	486
100:8	25	315
100:8	40	169
100:0	60	55

[a] DLS measurements
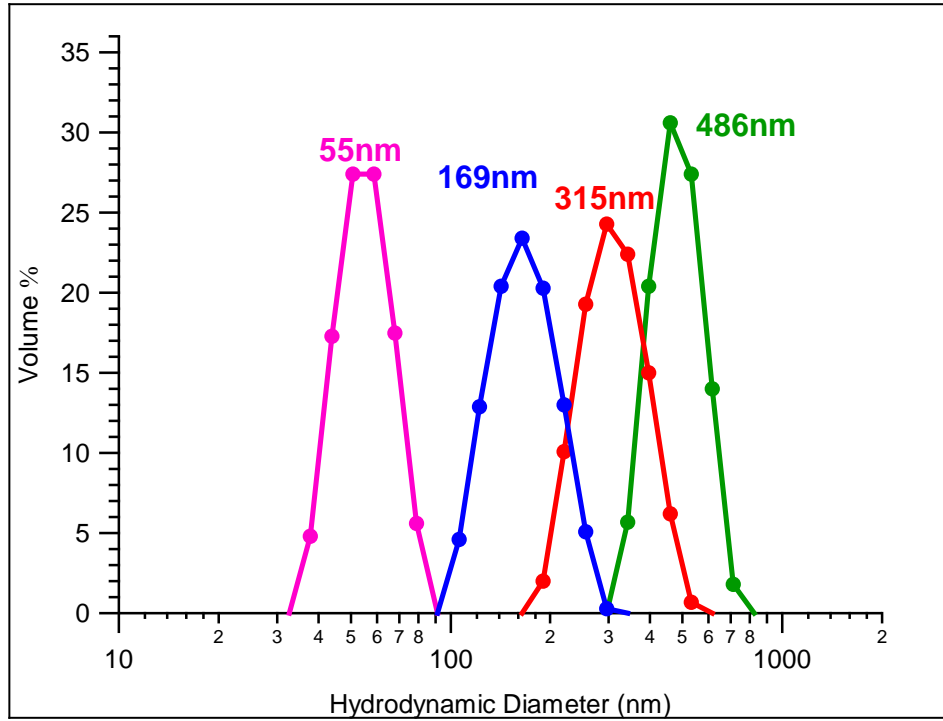
Figure 2.01. DLS measurements of Stöber SiO$_2$ colloids of different sizes.
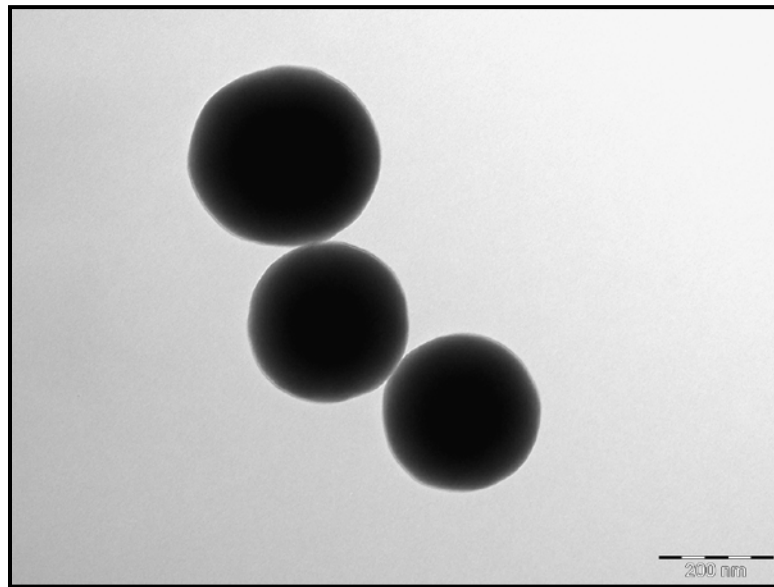
Figure 2.02. Typical TEM image of Stöber SiO$_2$ particles

37
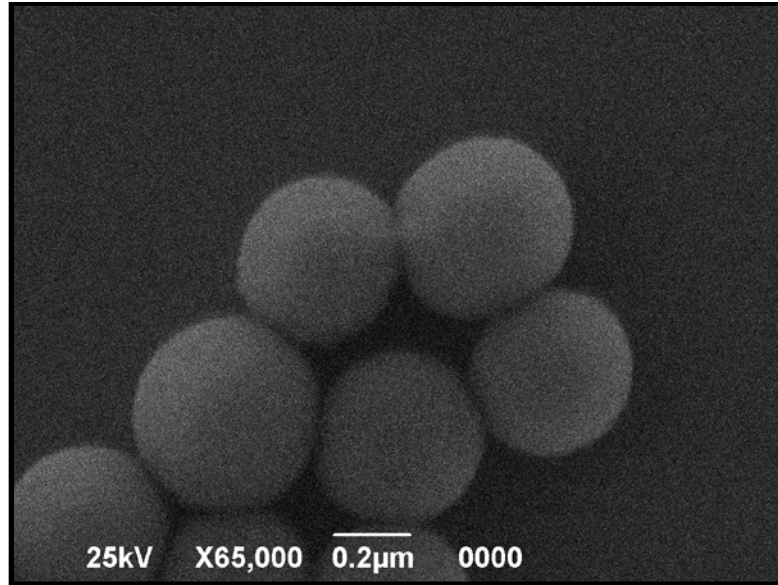
Figure 2.03. SEM image of Stöber SiO$_2$ colloids
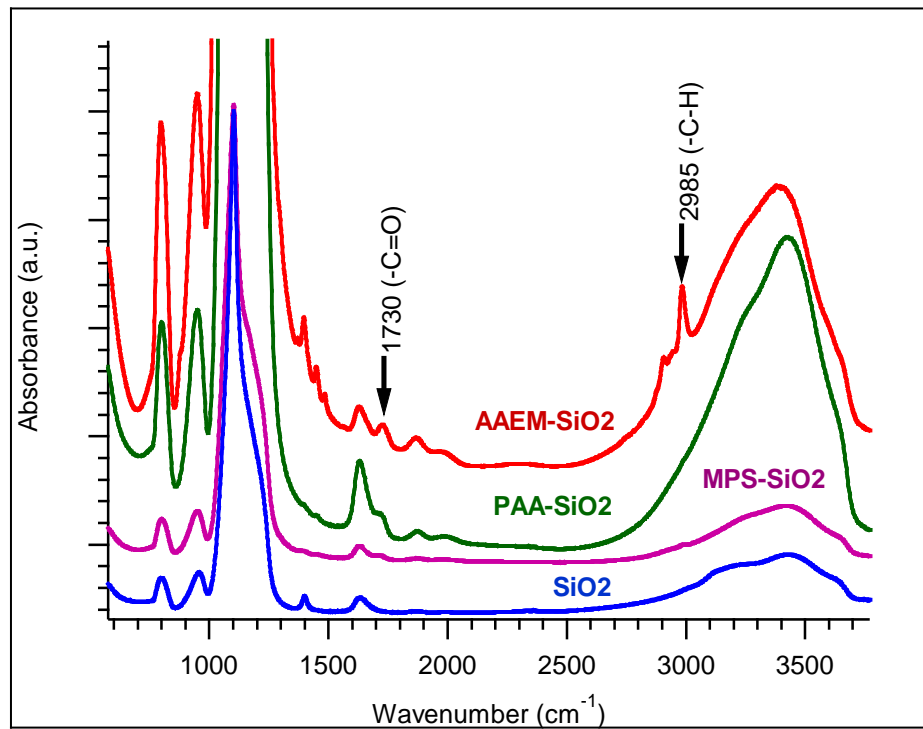
Figure 2.04. FTIR spectra of surface functionalized SiO$_2$ colloids

38
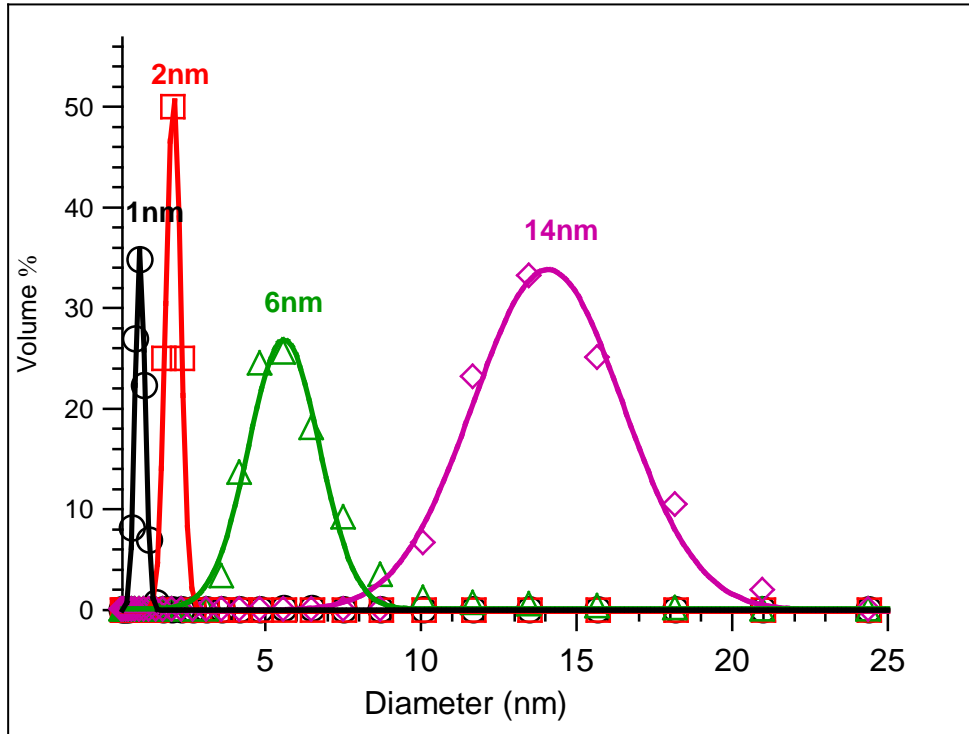
Figure 2.05. DLS of CoO nanoparticles
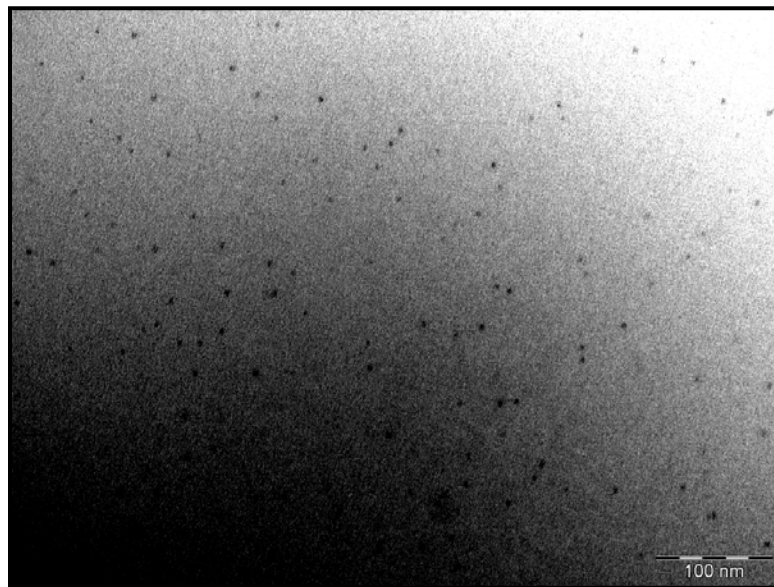
Figure 2.06. TEM image of 2 nm CoO nanoparticles

39
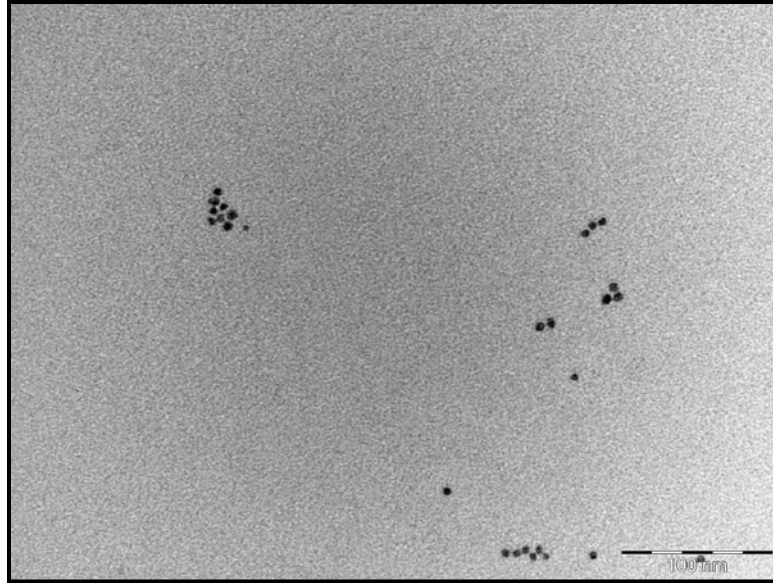
Figure 2.07. TEM images 6 nm CoO nanoparticles
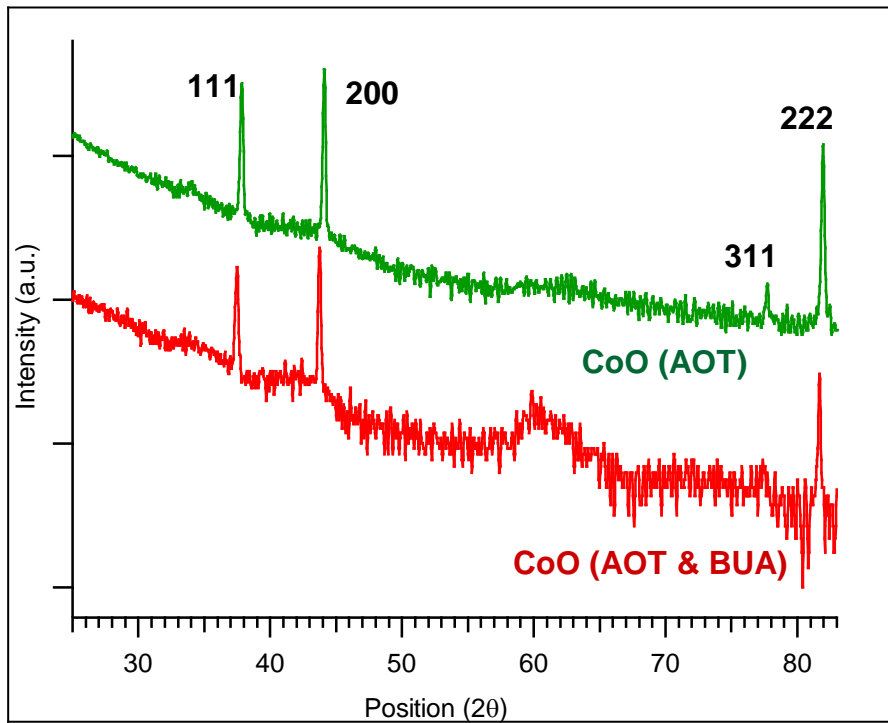
Figure 2.08. XRD of CoO nanoparticles prepared from single and two surfactants
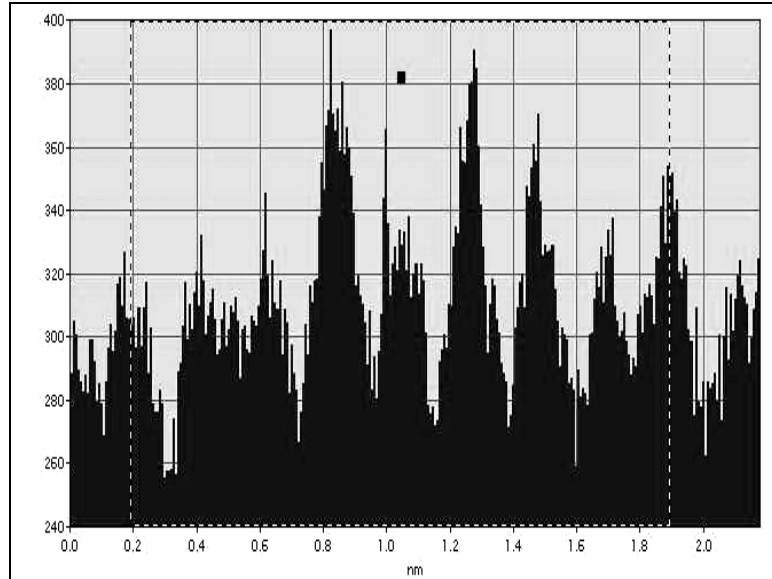
Figure 2.09. Measurement of lattice distance of CoO using an intensity vs. distance plot, obtained across a CoO nanoparticle from a hi-res TEM
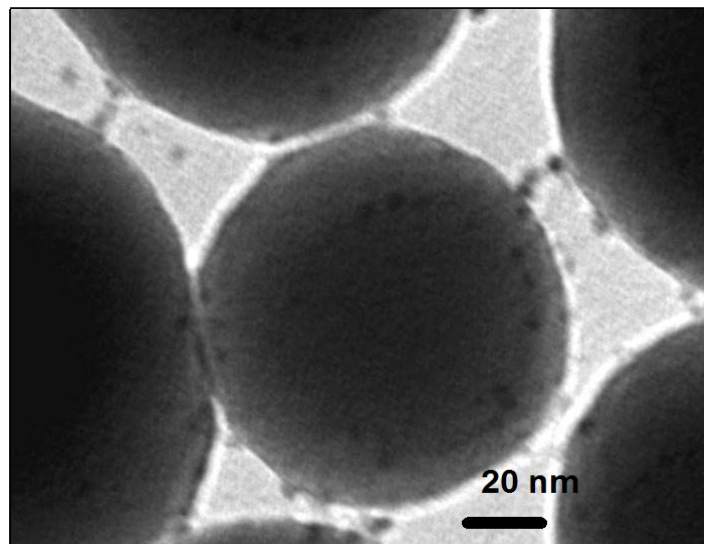
Figure 2.10. TEM image of CoO/MPS-SiO$_2$

41
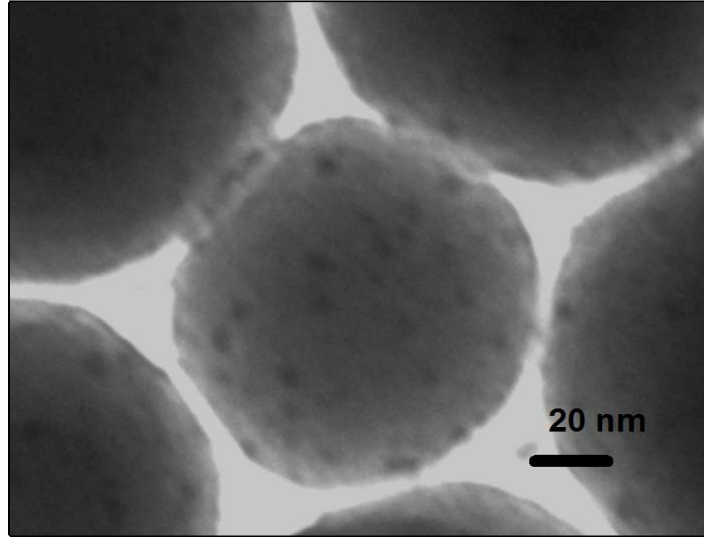
Figure 2.11. TEM image of CoO/AAEM-SiO$_2$
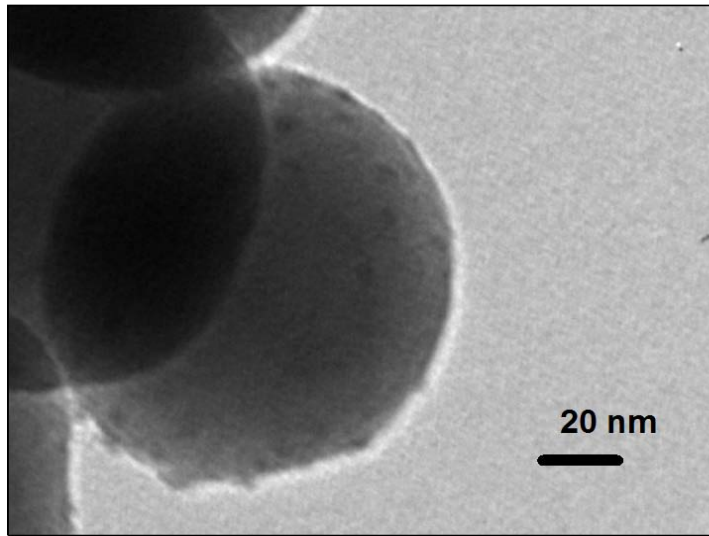
Figure 2.12. TEM image of CoO /PAA-SiO$_2$
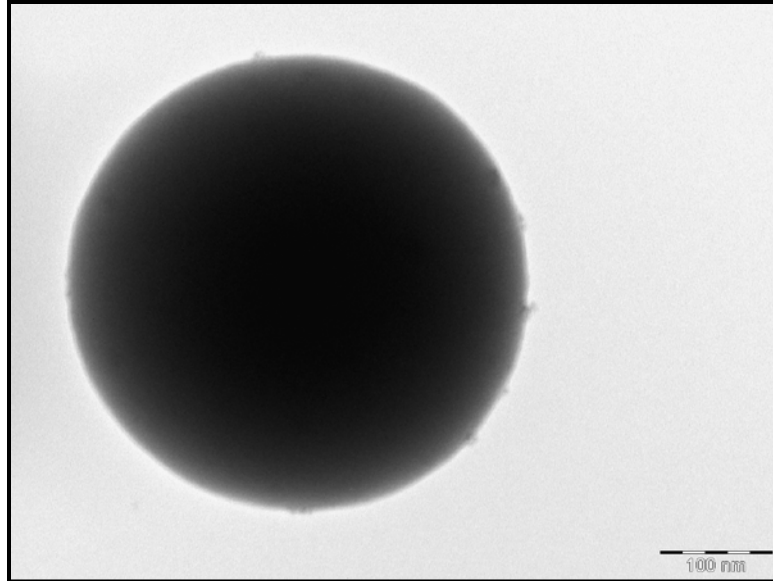
Figure 2.13. TEM of CoO/APDMS-SiO$_2$, where CoO was prepared with two surfactants
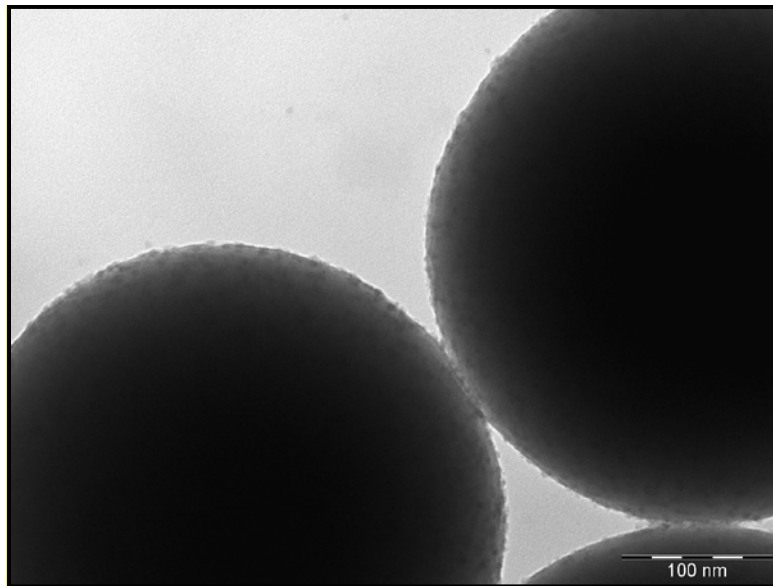
Figure 2.14. TEM 2nm CoO on MPS-SiO$_2$

43
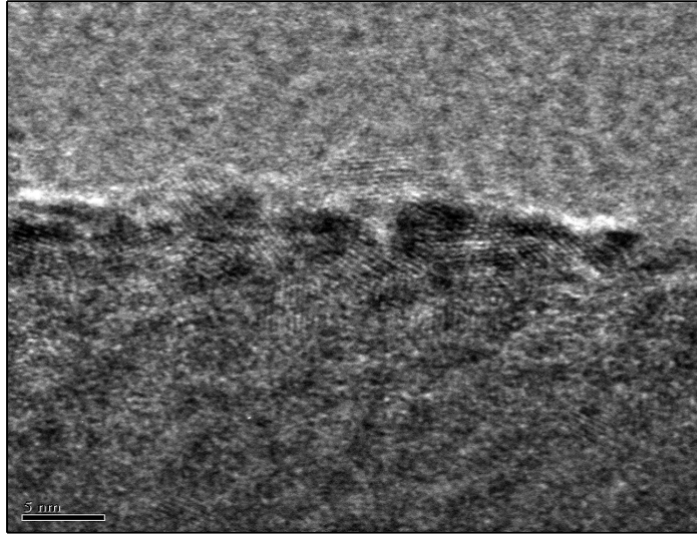
Figure 2.15. Hi-res TEM of CoO/SiO$_2$ with 2 nm CoO size.
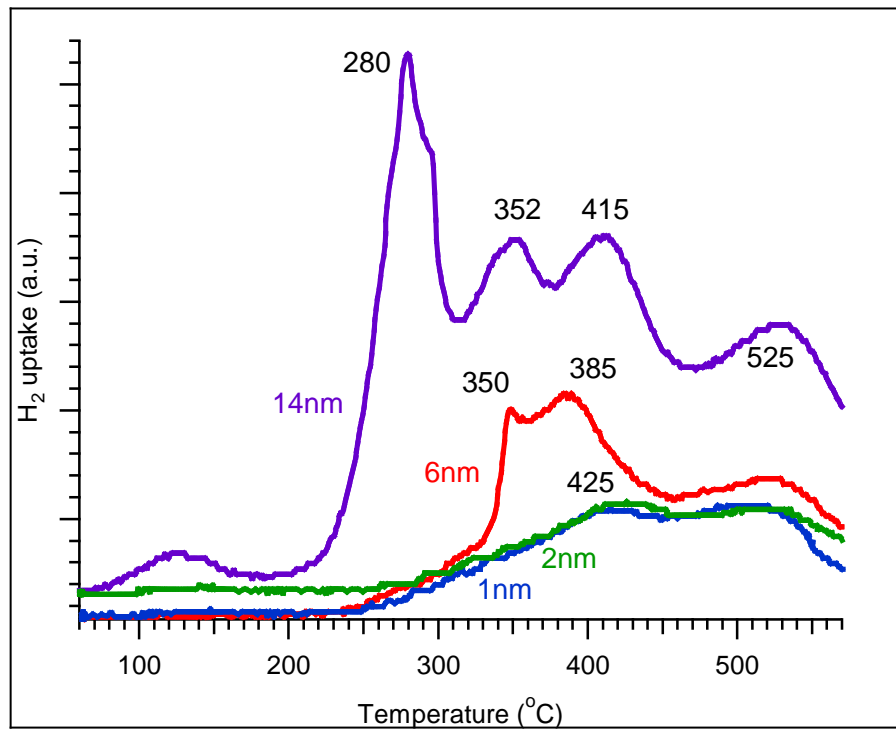
Figure 2.16. TPR profiles of CoO/SiO$_2$ nanocomposites of various CoO sizes

44
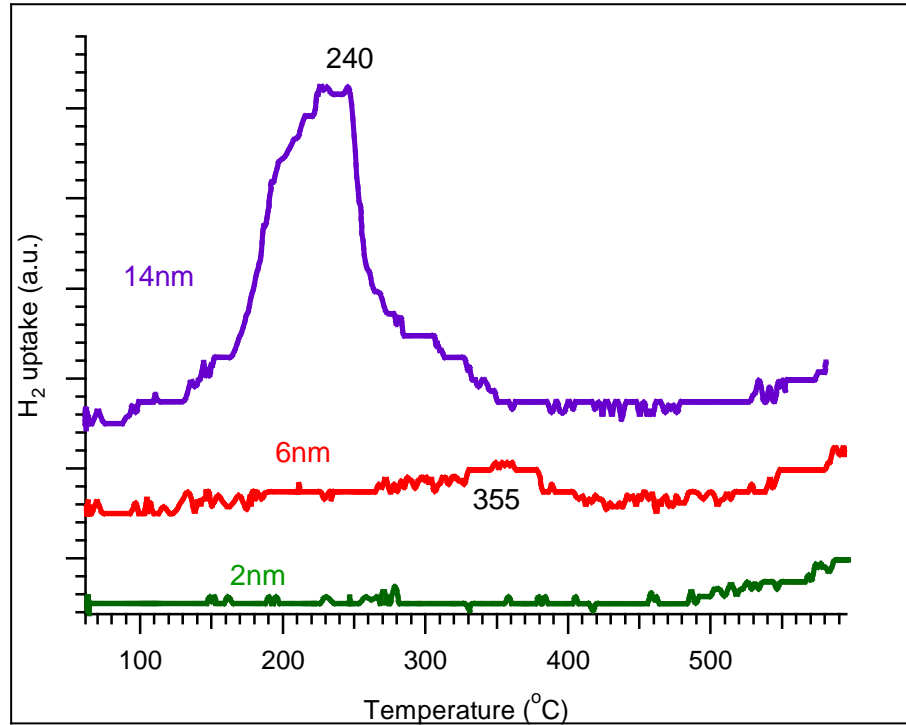
Figure 2.17. TPR profile obtained during the second run on CoO/SiO$_2$ nanocomposites of different sizes
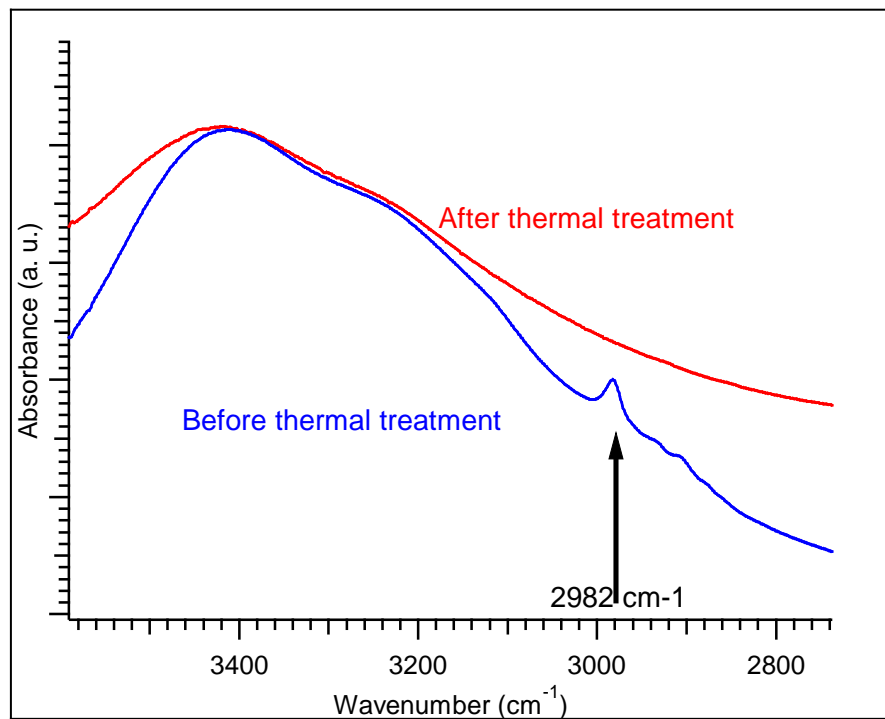
Figure 2.18. FTIR spectrum (2700 – 3600cm^{-1}) of nanocomposites with 6 nm CoO before and after TPR

45
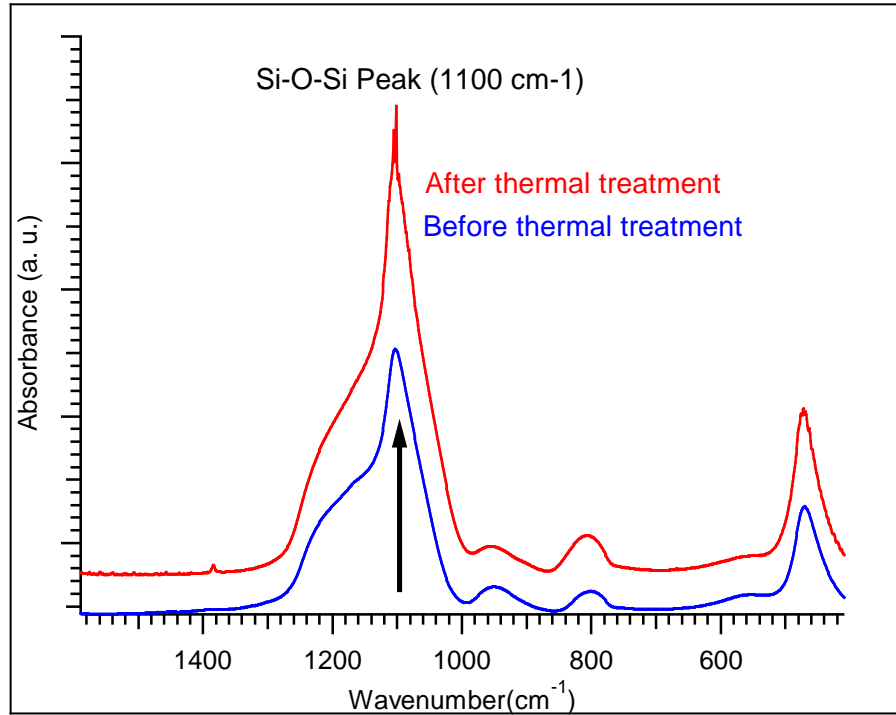
Figure 2.19. FTIR spectra (400 – 1600cm^{-1}) of nanocomposites with 6 nm CoO before and after TPR
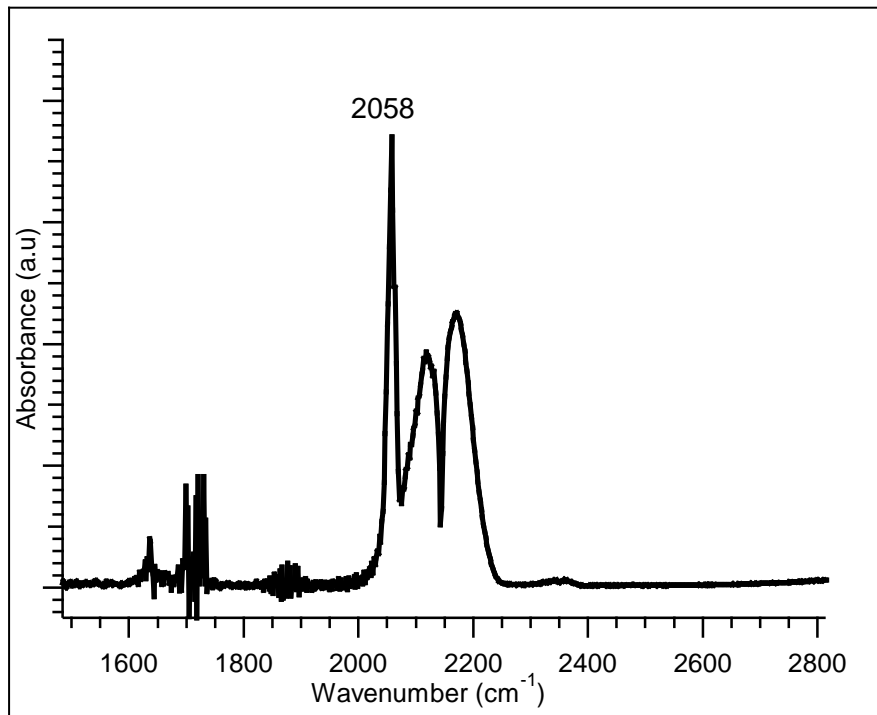
Figure 2.20. FTIR spectrum collected when carbon monoxide and air was introduced into the reactor

46
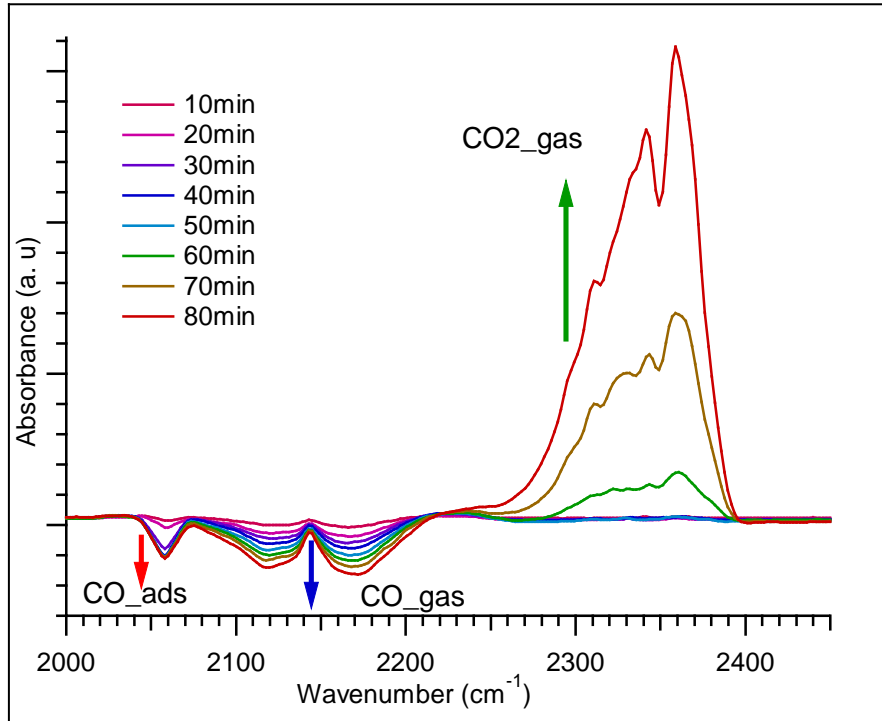
Figure 2.21. FTIR spectra collected at various intervals of time during 4.5°C/min temperature ramp.
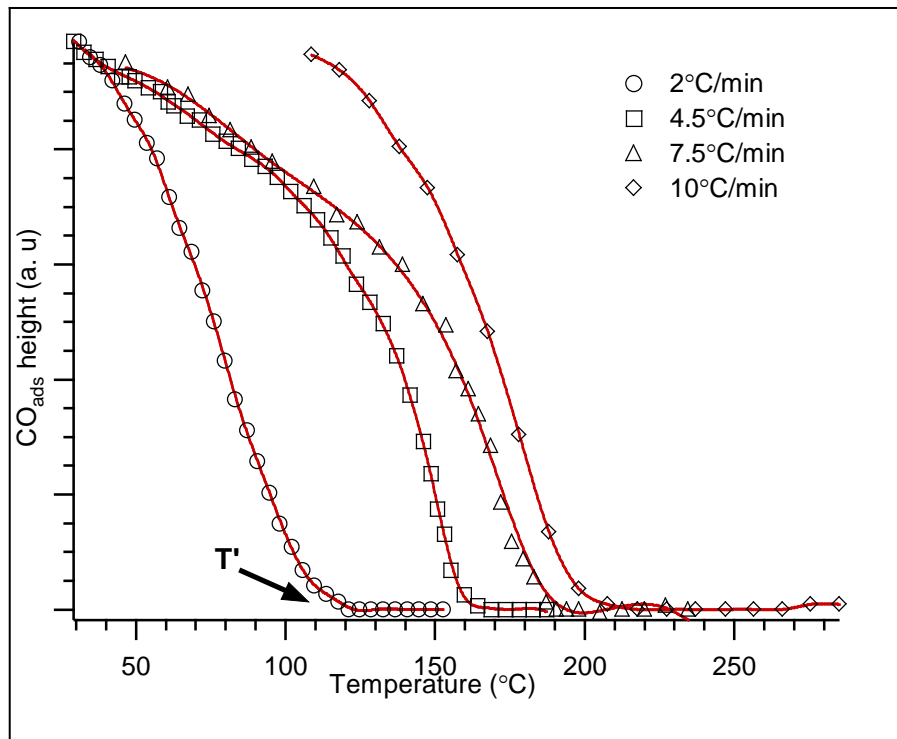
Figure 2.22. The 2058 cm^{-1} peak height recorded at various heating rates for nanocomposite with 14 nm sized CoO nanoparticles

47
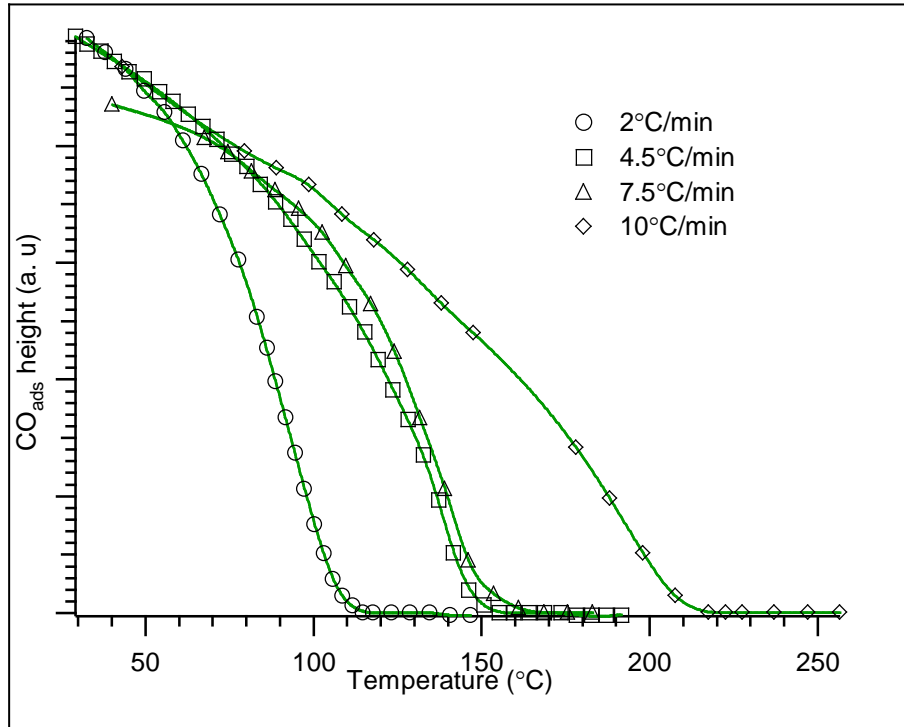
Figure 2.23. The 2058 cm^{-1} peak height recorded at various heating rates for nanocomposite with 6 nm sized CoO nanoparticles
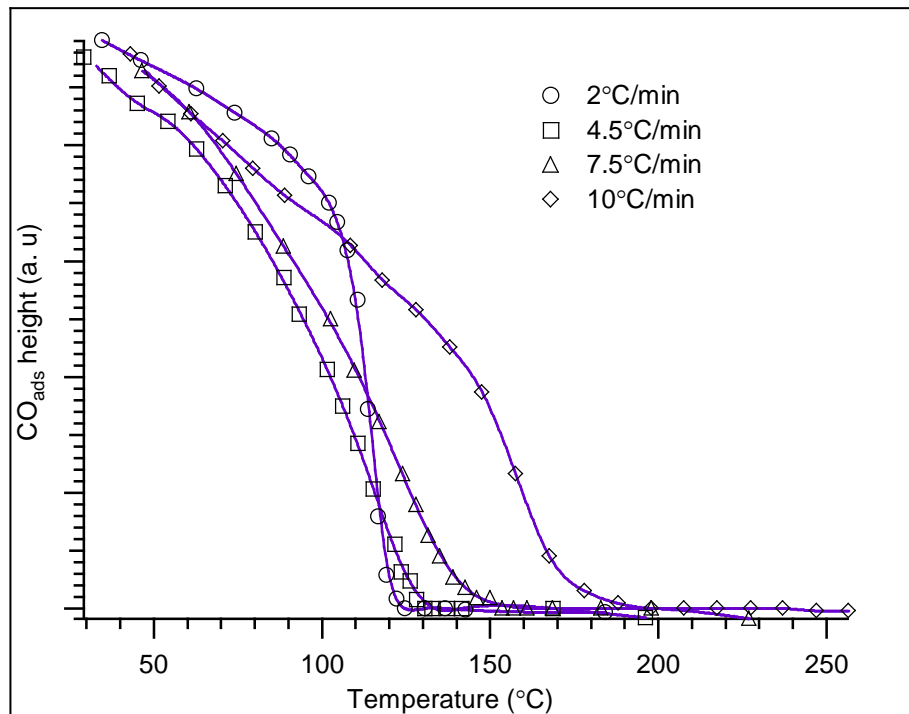
Figure 2.24. The 2058 cm^{-1} peak height recorded at various heating rates for nanocomposite with 2 nm sized CoO nanoparticles

48
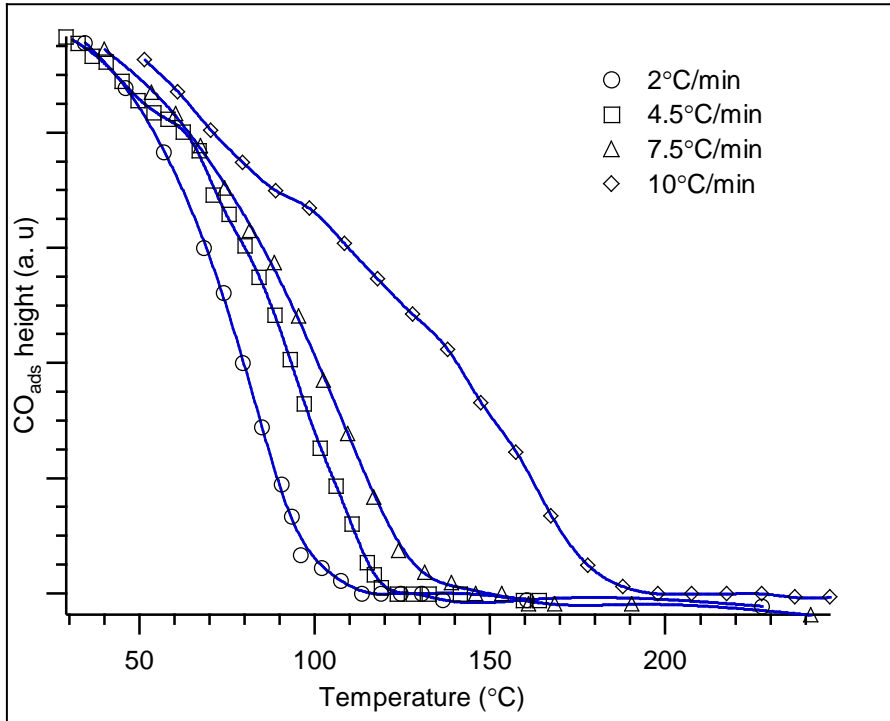
Figure 2.25. The 2058 cm^{-1} peak height recorded at various heating rates for nanocomposite with 1 nm sized CoO nanoparticles
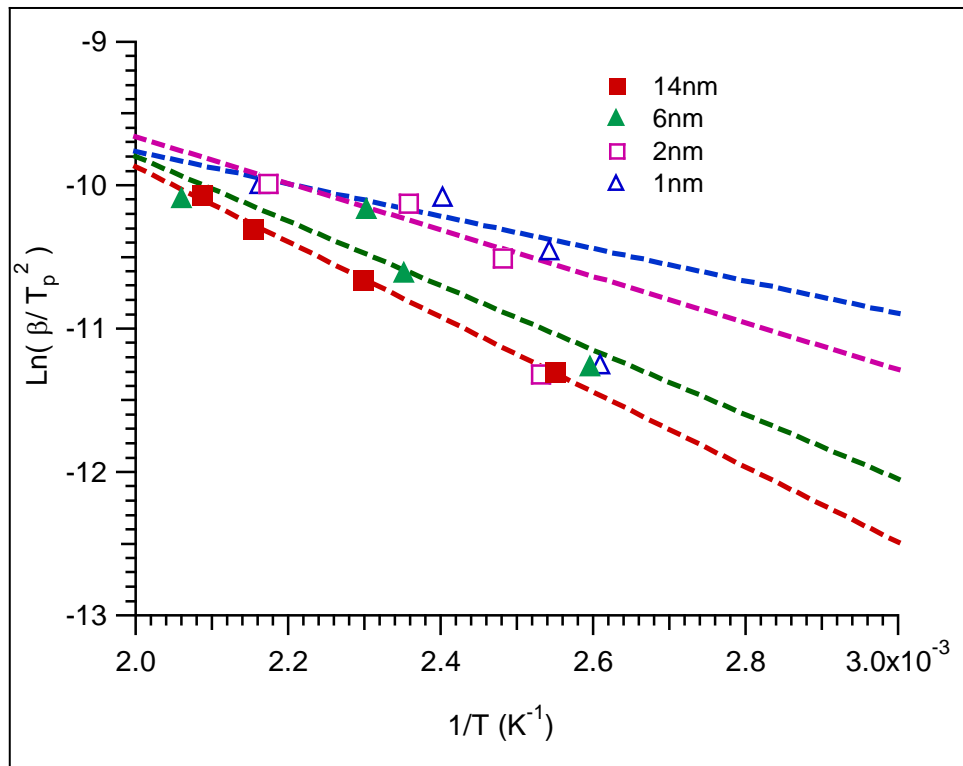
Figure 2.26. Kissinger plot to find E_{step-1} from slope -E/R

49
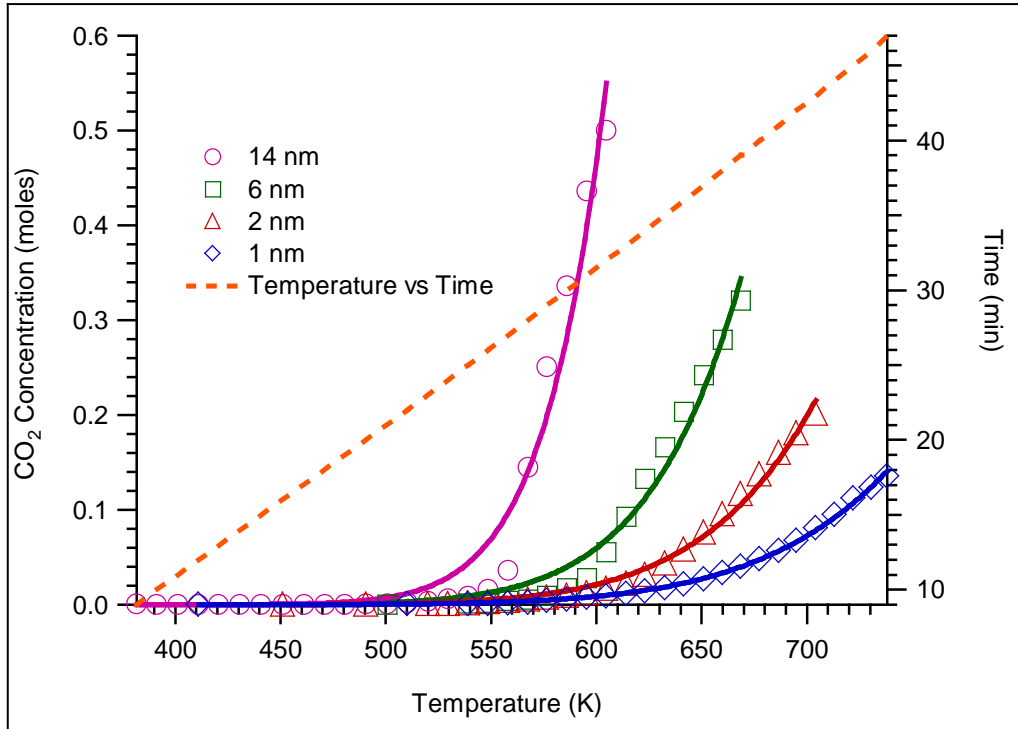
Figure 2.27. CO_2 evolution profile for nanocomposites with different sizes during the heating ramp of 9.7˚C/min
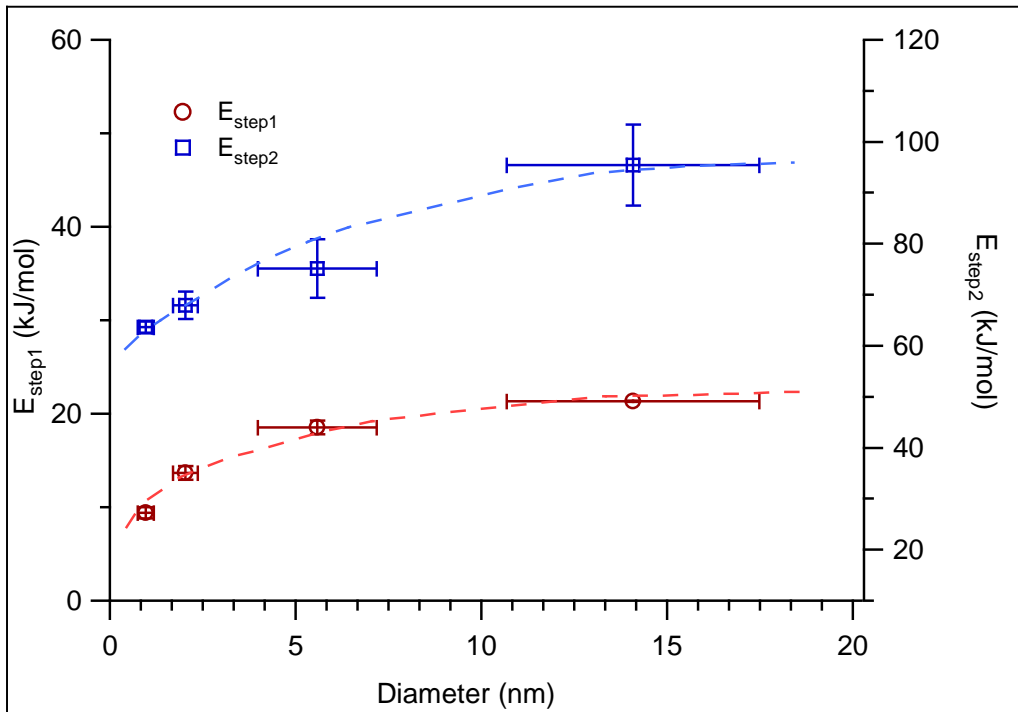
Figure 2.28. Activation energies of step-1 and step-2 for various CoO nanoparticle sizes

50

CHAPTER 3: HIGH SURFACE AREA TITANIA NANOSHELLS FOR CARBON DIOXIDE PHOTOREDUCTION

Increasing surface area is one of the key features that can help enhance product yield in catalytic reactions. In this chapter, a colloidal synthesis approach is described for the preparation of a TiO_2 based photocatalyst with high surface area. Novel TiO_2 nanoshells were created by precipitating different precursors of TiO_2 on polymer-core or SiO_2-core colloidal support materials. Surface modification procedures were used to control precipitation of TiO_2 on the different support materials. A collection of characterization tools were used to understand the physical and chemical characteristics of the novel photocatalytic nanoshells. In this chapter, CO_2 photoreduction reactions performed using a bench scale photo-reactor are also detailed. The performance of the nanoshells is contrasted to a commercial titania powder.

3.1 Experimental details and material characterization

3.1.1 Template synthesis

Different types of support materials or templates were prepared synthesize TiO_2 shells with high surface area by creating template-core/TiO_2 nanostructures. In general templates were two types: (a) polymer core, or (b) SiO_2 core. The surfaces of these colloidal core materials were then functionalized with chemical functional groups that initiated TiO_2 nucleation and growth on the surface of the template. Figure 3.1 depicts a general scheme of steps that were followed for TiO_2 nanoshell preparation. Details on preparation of the polymer and SiO_2 based templates are given below.

51

MPS/poly(NIPAAM-MBAA) colloidal templates is made of a cross-linked copolymer poly(NIPAAM-MBAA) with a siloxane shell around the copolymer core. Typically, 1 gm of NIPAAM monomer was copolymerized with 50 mg of N,N -methylene *bis*(acrylamide) (MBAA) in a 140 ml water bath maintained at 75 C under a N_2 atmosphere. To initiate the polymerization, 200 mg of KPS was added. After 2 h of polymerization, 240µL MPS (25wt% of the NIPAAM monomer used) was added and the reaction was continued for another 4.5 h. This allowed us to create an inner core consisting of copolymerized NIPAAM and MBAA polymers, and the outer shell of the same copolymer with additional interpenetrating siloxane chains as shown in the schematic (Figure 3.1). After the reaction was complete, the solution was cooled to room temperature and centrifuged at 7500 rpm for 30 min. The supernatant was discarded and the precipitate was re-dispersed in water. The purification steps of centrifugation and re-dispersion were repeated two more times. The purified sample was denoted as MPS/poly(NIPAAM-MBAA).

A second type of polymer template synthesized was using AAEM and poly(NIPAAM-MBAA) composites. These templates were prepared in a similar manner as MPS/poly(NIPAAM-MBAA) mentioned above. Here, after 2 h of copolymerization of NIPAAM and MBAA, 180 µL AAEM (16wt% of monomer) was added. The reaction was continued for another 9 h. In these composites, the inner core consists of copolymerized NIPAAM and MBAA polymers and a shell of the same copolymer with additional AAEM chains as depicted in Figure 3.1. The solution was cooled and the particles were purified by centrifugation and washing cycles with water as before. The sample was denoted as AAEM/poly(NIPAAM-MBAA).

52

SiO$_2$-core based templates were composed of a SiO$_2$ core and an outer surface of SiO$_2$ grafted with short polymer chains or ligands such as poly(NIPAAM), poly(acrylic acid) or MPS. These chemical functional groups were grafted on the surface of SiO$_2$ colloids and the preparation procedures are similar to that mentioned earlier in chapter 2, section 2.1.1.

Briefly, SiO$_2$ colloids were synthesized by the hydrolysis of TEOS in an ethanol-water solvent. Grafting of short oligomeric chains was performed by the polymerization of the respective monomer solution in the presence of MPS, a coupling agent that helps to covalently bond the polymer chain and SiO$_2$ surface[88-90]. For instance, to prepare NIPAAM-grafted SiO$_2$, an aqueous based solution containing NIPAAM monomer and MPS was prepared such that the molar concentration of the monomer was approximately 100 times MPS concentration. The solution was heated to 60°C and the polymerization was initiated by 0.6 wt% KPS. After 12 hours, Stöber SiO$_2$ particles were added and stirred at 60 for another 24 hours. The solution was cooled and the particles were purified by centrifugation and washing cycles with water. The colloidal particles were dried and denoted as NIPAAM-SiO$_2$. The preparations of MPS-SiO$_2$ and PAA-SiO$_2$ have been detailed earlier in sections 2.1.2. SiO$_2$-core based and polymer-core based templates were used further for the creation of TiO$_2$ shells via precipitation.

3.1.2 TiO$_2$ nanoshell preparation

Different precursors of TiO$_2$ such as tetrabutyl orthotitanate (TBOT), titanium bis-ammonium lactato dihydroxide (TALH) or titanyl sulfate (TS) were used to create TiO$_2$ nanoshells on the templates that were synthesized. TBOT rapidly hydrolyzes in the presence of water to form TiO$_2$, whereas TALH and TS were water soluble and relatively

53

stable compounds in aqueous solutions at room temperature. Rate of precipitation of TALH & TS can be accelerated by heating the precursor solutions or by adding precipitating agents or by both. Urea and sulfuric acid were added to TALH and TS solutions respectively to initiate the precipitation reaction. Due to the quick precipitating nature of TBOT precursor in water, TBOT precipitation was performed in ethanol rich solvents using SiO_2-core templates functionalized with chemical groups such as MPS, PAA or AAEM and polymer-core templates. Since TALH & TS relatively stable in water, the precipitation of these precursors were performed in water solvent.

To precipitate TBOT to form TiO_2 shells, an ethanol solution containing 2 mM TBOT was prepared containing template material with a concentration of 100 mg/ml for SiO_2-core and 50 mg/ml for polymer-core solutions. 10 ml of template solution was taken and approximately an equal volume of ethanol-water solution with a 90 vol% ethanol concentration was added drop-wise under constant mixing. The solution was kept stirring for another 30 min at room temperature. A basic pH was maintained by adding few drops of 28 wt% NH_4OH during the precipitation reaction to help the deposition of TBOT on the surface of template rather than in the bulk solution. The TiO_2 deposited SiO_2 composites were separated from free TiO_2 in the bulk solution by centrifuging the entire solution at 5,000 rpm. The supernatant rich in free TiO_2 particles was decanted and the final TiO_2/SiO_2 composites were dried at 50°C in the vacuum oven for ~1day.

TS, a water soluble precursor was also used to create TiO_2 shells. Here, a stock solution of TS was prepared by adding 0.0665 g of solid TS to 1.2 ml of 1 M H_2SO_4. To a 30 ml polymer-core colloidal template solution containing approx 50 mg/ml template in water, 200 µL of the TS stock solution prepared earlier was added. The solution was

54

heated to 90°C for ~1 hour until a turbid solution was obtained. The particles were purified by centrifugation and dispersing steps as followed previously.

TALH was precipitated on NIPAAM-SiO$_2$ to synthesize SiO$_2$@TiO$_2$ core-shell structures. The precipitation of TALH was initiated by heating the precursor solution in the presence of urea[174, 175]. Here, 1 gm of PNIPAAM-SiO$_2$ particles were dispersed in aqueous solution of 3 mM TALH and 10 mM urea. After stirring for one hour at room temperature, the solution was refluxed at 100 C for 20 h under N$_2$ atmosphere. TiO$_2$/SiO$_2$ composites were centrifuged at 7,500 rpm for 30 min and supernatant decanted to separate the freely suspended TiO$_2$ particles in the supernatant from the composites. The precipitate was re-dispersed in water and centrifuged again. Purification steps of centrifuging and dispersing in water were done a few times to remove solvents or unreacted chemicals. The final residual precipitate was dried at 50C in the vacuum oven for ~1day.

The composites with a TiO$_2$ shell were calcined at 600 $^{\circ}$C by ramping the temperature from room temperature to 600°C at 2 $^{\circ}$C/min and maintaining at 600°C for 2 hours. The calcination step was performed to remove the polymer chains, grafting agents and other organic residues prior to performing any photocatalytic reactions.

3.1.3 Preparation of co-catalyst Pt nanoparticles

Pt co-catalyst nanoparticles were prepared to enhance in catalytic activity of TiO$_2$ photocatalyst. Composites of TiO$_2$ deposited with metal(s) have been gaining interest in the field of phocatalysis for increasing activity of TiO$_2$ photocatalyst[63, 176, 177]. A co-catalyst metal in contact with a photocatalyst such as TiO$_2$ helps to suppress electron-

55

hole recombination thereby increasing the availability of photo-exited charges to carry out in redox reactions[63, 74-82]. Pt metal have been widely used a co-catalyst in promoting reduction half-reaction during photocatalytic redox reactions[178]. Pt nanoparticles were prepared from $NaBH_4$ reduction method[179]. Typically, 200μL of 112mM $NaBH_4$ was rapidly added to a 10ml of aqueous solution of 1mM K_2PtCl_6 and 3.88mM citric acid, trisodium salt dihydrate. Immediately upon $NaBH_4$ addition, transparent yellow colored solution turned to black color confirming the formation of Pt nanoparticles. Pt nanoparticle colloid solution was mixed with TiO_2 nanoshell composites to prepare Pt deposited TiO_2 nanocomposites for photoreduction experiments. Typically 4ml of Pt colloidal was mixed with 1g of TiO_2 photocatalyst.

3.1.4 Procedure for CO_2 photoreduction

Photoreduction experiments were carried out in an aluminum reactor with two ports for inlet and outlet flow of gases. The reactor had three optical windows - one glass window at the top for photoirradiation and two ZnSe windows on two sides for infrared measurements. The detailed mechanical drawings and design measurements of the photo-reactor and other components are given in figures 3.2-3.8.

The transmission range of the glass window ranged from 330nm to 670nm to allow irradiation in the long UV and visible wavelengths. A cylindrical insert made of Teflon® was placed inside the photo-reactor to reduce the reactor volume and thereby, increase the concentration of species in the gas phase. Approximately 1gm of the different photocatalyst was filled and leveled into a circular Teflon dish with 1 mm depth. The final exposed cross-sectional area of the photocatalyst bed exposed to the incident radiation was 9mm^2.

56

During the testing, the reactor was evacuated for 5-10 min using a vacuum pump set for 20 inches Hg vacuum pressure. CO_2 gas saturated with water was allowed to flow into the evacuated reactor. These evacuate-fill cycles were repeated 4 more times to eliminate any remnant ambient gases and other impurities. CO_2 gas bubbled through water was then continuously purged through the reactor for 1.5 h at ambient temperature and pressure to saturate the contents of the reactor and the photocatalyst. The reactor pressure was first increased to 10 psi by closing the outlet valve and then the inlet flow was also stopped. Photo-irradiation was performed in a batch mode for 6 h using a 100 W Hg lamp placed vertically downward on a wooden stand as a light source. The hydrocarbon formation inside the photo-reactor was measured using FTIR. Two sets of control experiments were conducted. Experiments were conducted in dark in the presence of reactant gases and photocatalyst samples. The second set of experiments was conducted using N_2 gas in the place of CO_2 under UV-light conditions.The infrared absorption was recorded on a Magna-R 860 spectrometer (Nicolet, WI, USA). The peak responses of CH_4 and CO from FTIR analysis were obtained using a separate calibration of the FTIR signal to known quantities of CH_4 and CO.

3.2 Results and discussion

The structural and chemical characteristics of TiO_2 shell nanocomposites were studied using different characterization tools and techniques. To verify TiO_2 shell formation on different templates, TEM images of just the template-core were taken and compared with the TEM images after TiO_2 precipitation on the core.

3.2.1 DLS and TEM analysis of templates

MPS/poly(NIPAAM-MBAA) and AAEM/poly(NIPAAM-MBAA) hybrid template materials were analyzed using DLS and TEM to characterize the size, shape and thermal responsiveness of the hybrid core. Poly(NIPAAM) is a thermally responsive material, i.e. it undergoes a physical change in the presence of thermal stimuli. Heskins and Guillet[180] were the first to investigate the thermal responsive nature of poly(NIPAAM) and found the lower critical solution temperature (LCST) of the polymer to be 32°C.

Figure 3.9 and 3.10 displays the variation in hydrodynamic size of these hybrid materials as a function of solution temperature. The analysis shown was performed using DLS at different temperatures ranging from 20°C to 40°C for samples with a concentration of ~0.001 wt% template-core material in water. The size of MPS/poly(NIPAAM-MBAA) varies from ~430 nm below LCST and ~310nm above LCST as depicted in figure 3.9. In comparison, the size of hybrid AAEM/poly(NIPAAM-MBAA) changes from ~600 nm below LCST and ~370 nm above LCST as shown in figure 3.10. TEM images shown in figures 3.11-3.13 suggest that polymer templates were approximately spherical in shape and fairly uniform in size. The TEM images of SiO_2-core based templates such as MPS-SiO_2, PAA-SiO_2 and NIPAAM-SiO_2 (figure 3.14) were also analyzed. In contrast to the denser, cross-linked polymer cores, the short oligomers or ligands that were grafted on SiO_2 could not be visualized in TEM.

3.2.2. TEM analysis of TiO_2 precipitation on templates

The precipitation of TBOT precursor on different templates rich in –C=O were verified by TEM analysis. Figure 3.15 shows a thin layer of TiO_2 formed after the

58

precipitation of TiO₂ on MPS-SiO₂ template. In contrast to MPS, AAEM is a diketone and has two –C=O groups per molecule. Figure 3.16 shows that TiO₂ shell coverage and thickness was improved when AAEM-SiO₂ was used when compared to MPS-SiO₂. The precipitation of TiO₂ on SiO₂-template surface can also be initiated with the addition of acetonitrile. Figure 3.17 shows a TEM image of TiO₂ shells precipitated on AAEM-SiO₂ in the presence of 3-4 drops of acetonitrile as compared to NH₄OH in figure 3.16. It was observed that without the presence of small amounts of NH₄OH or acetonitrile the TiO₂ tends to precipitate in the bulk solution than on the template surface. In contrast to the small molecule ligands MPS and AAEM, TBOT precipitation was also successful on PAA-SiO₂ in the presence of NH₄OH to form a thin layer of TiO₂. TEM of TiO₂ shell on PAA-SiO₂ is shown in figure 3.18. TBOT precipitation on NIPAAM-SiO₂ was not observed which may be due to the hydrophobic nature of TBOT and the hydrophilic nature of NIPAAM. These results illustrate that a thin shell of TiO₂ can be precipitated using TBOT precursor on SiO₂-core based templates by applying suitable surface modification treatments to initiate nucleation and growth of TiO₂ on the surface of the template.

The precipitation of TBOT on polymer-core based templates was also examined. Figures 3.19 and 3.20 depicts the polymer-core based composite MPS/poly(NIPAAM-MBAA) obtained after TBOT precipitation. The composites obtained using AAEM/poly(NIPAAM-MBAA) are shown in figures 3.21 and 3.22. The morphology of this composite was different from MPS based hybrid template. Here, the TiO₂ nanoparticles were largely uniform in size and were decorated around the polymer core. We believe that a reason for this type of arrangement could be the strong interaction between diketone chemical groups of AAEM and TiO₂ particles formed during precipitation.

59

However, a complete shell of TiO_2 was not formed plausibly due to the quick nucleation and precipitation of TBOT. Figure 3.23 shows the TEM image of TS precipitated on a MPS/poly(NIPAAM-MBAA) polymer-core template. At the end of this reaction, clumps of white precipitate were observed at the bottom of the flask. From the TEM analysis, it is clear that TS and TBOT were not good choices as precursors for TiO_2 shell creation on the polymer-core templates.

TALH is a stable and water soluble precursor that hydrolyzes slowly. This property was useful to tune the precipitation and deposition of TiO_2 on NIPAAM modified templates. The precursor TALH did not hydrolyze in water at ambient conditions. The hydrolysis of TALH was driven by OH^- free radicals. A slow release of OH^- radicals was achieved by adding urea which hydrolyzes TALH slowly at room temperature but more rapidly at high temperatures. Figures 3.24 and 3.25 shows the TEM image of TALH treated with MPS/poly(NIPAAM-MBAA) and NIPAAM-SiO_2. It was seen from TEM image of MPS/poly(NIPAAM-MBAA) that there was higher contrast in the inner core rather than on the MPS rich outer surface of the polymer template. This may be because TALH prefers to bind with the hydrophilic inner core of poly(NIPAAM-MBAA) than hydrophobic MPS rich outer surface.

In the case of precipitation of TALH on NIPAAM-SiO_2, rough TiO_2 shells were created on NIPAAM-SiO_2 templates as shown in figure 3.25. Figure 3.26 reveals that these rough and high surface area nanoshells were maintained after calcinations of the composites at $500°C$ for 2 h. The morphological structure of TiO_2 was maintained even after high temperature calcinations and is indicative of good thermal stability of TiO_2

60

shells against rupture. The rough morphology with high surface area can be a beneficial feature for catalytic applications.

Pt nanoparticles synthesized via NaBH$_4$ reduction method, were analyzed using DLS and TEM as shown in figures 3.27 and 3.28. In figure 3.27, the intensity plot shows that there are two populations of nanoparticles one with ~4 nm and the other with ~50 nm average hydrodynamic diameter. The volume% plot in figure 3.27 and the TEM image in figure 3.28 suggest that the majority of the nanoparticles are in the 4 nm range and the 50 nm size observed in DLS measurements could be due to aggregation of Pt nanoparticles. Figure 3.29 displays TEM image of Pt deposited SiO$_2$@TiO$_2$. There was no significant difference in the TEM images of bare SiO$_2$@TiO$_2$ and Pt deposited SiO$_2$@TiO$_2$ due to the low TEM resolution that failed to discern the small nanoparticles. Another reason for the lack of verification of Pt deposition on the surface of SiO$_2$@TiO$_2$ composites could be the low percentage of Pt in the sample, which was roughly estimated to be 0.05% on total weight basis. Visual inspection revealed that the sample was however, slightly grayish in color after the Pt addition.

3.2.3. Diffuse reflectance, BET and XRD of TiO$_2$ nanoshells

BET of TiO$_2$ nanoshells created using NIPAAM-SiO$_2$ and TALH precursor were performed to estimate the surface area of nanoshell composites. Calcined samples were degassed at 80°C for ~4 hours prior to performing BET analysis on Autosorb-1. The total surface area of TiO$_2$ nanoshell composites prepared from precipitation of TALH on NIPAAM-SiO$_2$ was found to be 34.95 m^2/gm. The total surface area of Stöber SiO$_2$ was only 12.68 m^2/gm, which suggests a significant increase in surface area accompanies the creation of nanoshells structures on SiO$_2$ colloids.

The UV-Vis diffuse reflectance spectra of the TiO_2 nanoshell composites were also measured to investigate the optical response of the photocatalyst composite. The position of $SiO_2@TiO_2$ spectra is blue shifted from commercially available P25 TiO_2 signifying a higher band gap energy than P25 TiO_2 as shown in figure 3.30. This blue shift may be due to the smaller crystal size of TiO_2 in the $SiO_2@TiO_2$ composites than compared to P25 TiO_2[181, 182]. The crystallinity of TiO_2 was analyzed using XRD as shown in figure 3.31. The broadening of peaks in the XRD patterns can also be due to the smaller crystalline size of TiO_2[183].

3.2.4 Results on CO_2 photoreduction

FTIR spectra were collected at different intervals of time during photoreduction experiments through the ZnSe windows. TiO_2 nanoshell composites and nanoshells deposited with Pt were compared with commercially available Degussa[TM] P25 TiO_2 and Pt deposited P25 TiO_2. The conversion of CO_2 to CH_4 and CO is shown in FTIR spectra in figures 3.32-3.35. The peak at 3015 cm^{-1} in figures corresponds to CH_4 and the two peaks at 2172 cm^{-1} and 2143 cm^{-1} corresponds to CO.

We found an increase in production of CO and CH_4 as a function of time. Peak heights of CH_4 and CO were measured for all samples after 6 h of photoreduction reaction. The peak heights were correlated to molar concentrations of CH_4 and CO by plotting a calibration curve from known concentrations of CH_4 and CO. The calibration plots are shown in figures 3.36 and 3.37 for CH_4 gas and CO gas respectively. Figure 3.38 displays the photocatalytic yields of TiO_2 nanoshells and Pt deposited TiO_2 nanoshell composites, and their comparison with P25 TiO_2. Figure 3.38 also shows a total electronic yield calculated based on the theoretical number of electrons required for

62

the formation of one molecule of CH_4 or CO per molecule of CO_2. From redox potential diagrams[184, 185], it can be found that the theoretical number of electrons required for the reduction of one molecule of CO_2 to form one molecule of CH_4 or CO is 8 or 2 electrons respectively.

The catalytic activity of $SiO_2@TiO_2$ composites was comparatively lower than commercial Aeroxide P25 TiO_2. It was observed that the product yield is lower for TiO_2 nanoshell composites without the presence of Pt co-catalyst. The low yields may be due to the type of precursor used for this study that created an anatase phase of TiO_2 that was different from crystalline features of P25 TiO_2. [181, 183] Similar lower yields were obtained by Lee and coworkers[186] when they used photocatalysts prepared from TALH and reported lower activity than commercially available P25. Another possibility of lower yields may be due to higher electron-hole recombination or large build-up of photo-excited charges without proceeding in redox reactions. There have been some reports in the past studying this phenomena and possible ways to measure this factor quantitatively[187-189]. However, using our setup qualitatively comparison was not feasible. Pt deposited TiO_2 nanoshells showed improved catalytic activity compared to commercially available TiO_2. This is an indication that Pt helps to reduce electron-hole recombination and build-up of photo-excited charges on the surface of TiO_2.

3.3 Summary

We have shown here a colloidal approach to synthesize high surface area catalyst and establish its role in catalysis. Colloidal preparation techniques were used to prepare different template materials to create TiO_2 shells. TALH precursor was found to be optimal for the creation of novel core-shell TiO_2 composites. The nanoshell structure

63

led to increase in surface area. An added advantage of TiO_2 shells over TiO_2 nanoparticles was that the core-shell composites were relatively heavier than TiO_2 nanoparticles and therefore settled to the bottom. This may be beneficial in industrial applications to easily recover the catalyst from a liquid suspension after the reaction has ended, without resorting to expensive centrifugation methods. Material characterizations such as TEM, DLS, BET and UV-Vis reflectance spectroscopy were performed to understand the physical and chemical properties of the nanocomposites. CO_2 photoreduction experiments were carried out in a home built photoreactor. The catalytic performance testing showed that high surface area TiO_2 nanoshells have better catalytic activity when a co-catalyst such as Pt was deposited.
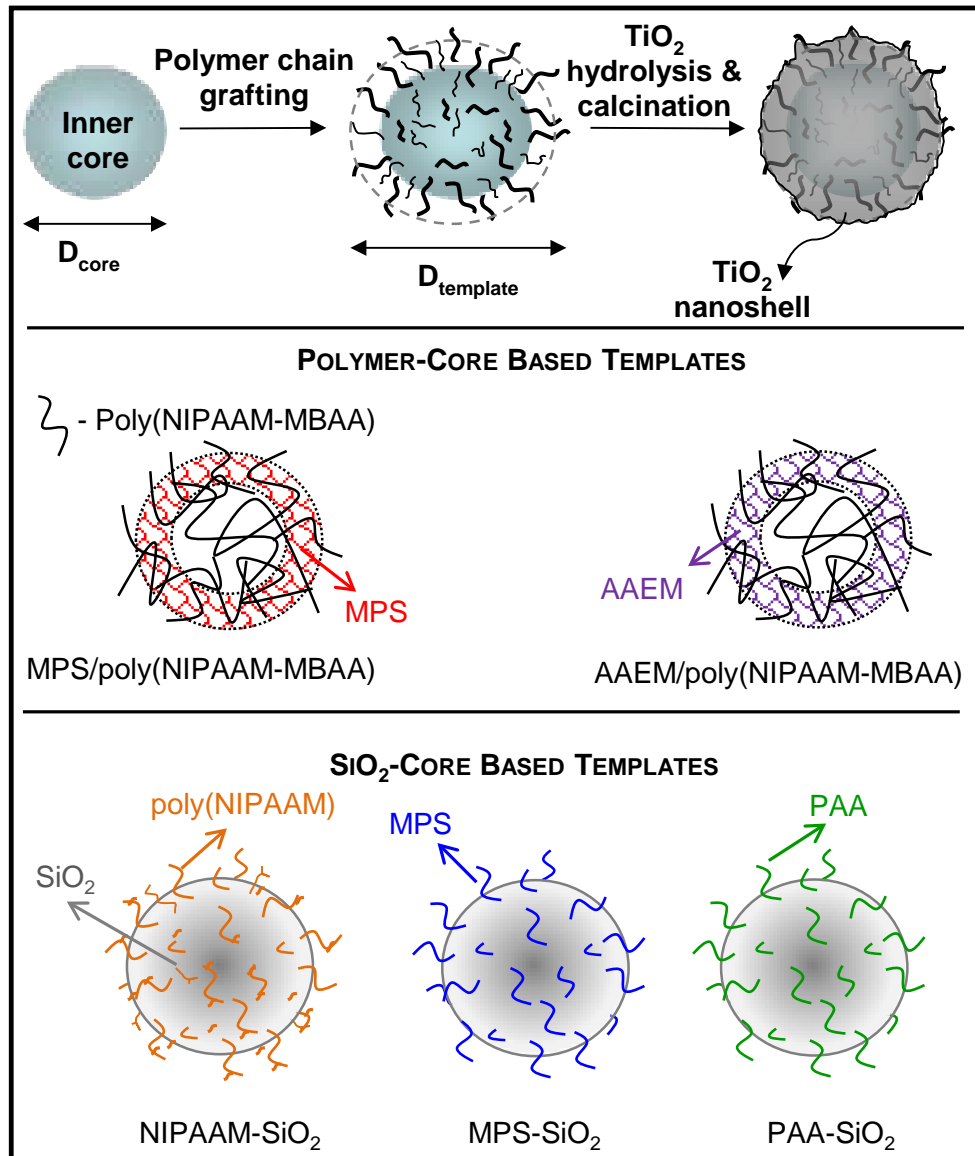
Figure 3.01. Schematic of TiO$_2$ nanoshells preparation on templates

Figure 3.02. A photograph of photoreactor, cylindrical block made of Delrin and sample dish made of Teflon

66

TOP VIEW

PHOTO-REACTOR

50mm
outer dia

25 mm

14 mm

14 mm

100 mm

70 mm

FRONT VIEW

SIDE VIEW

20 mm

25 mm

¼" NPT

70 - 100 mm

100 mm or less

BOTTOM VIEW
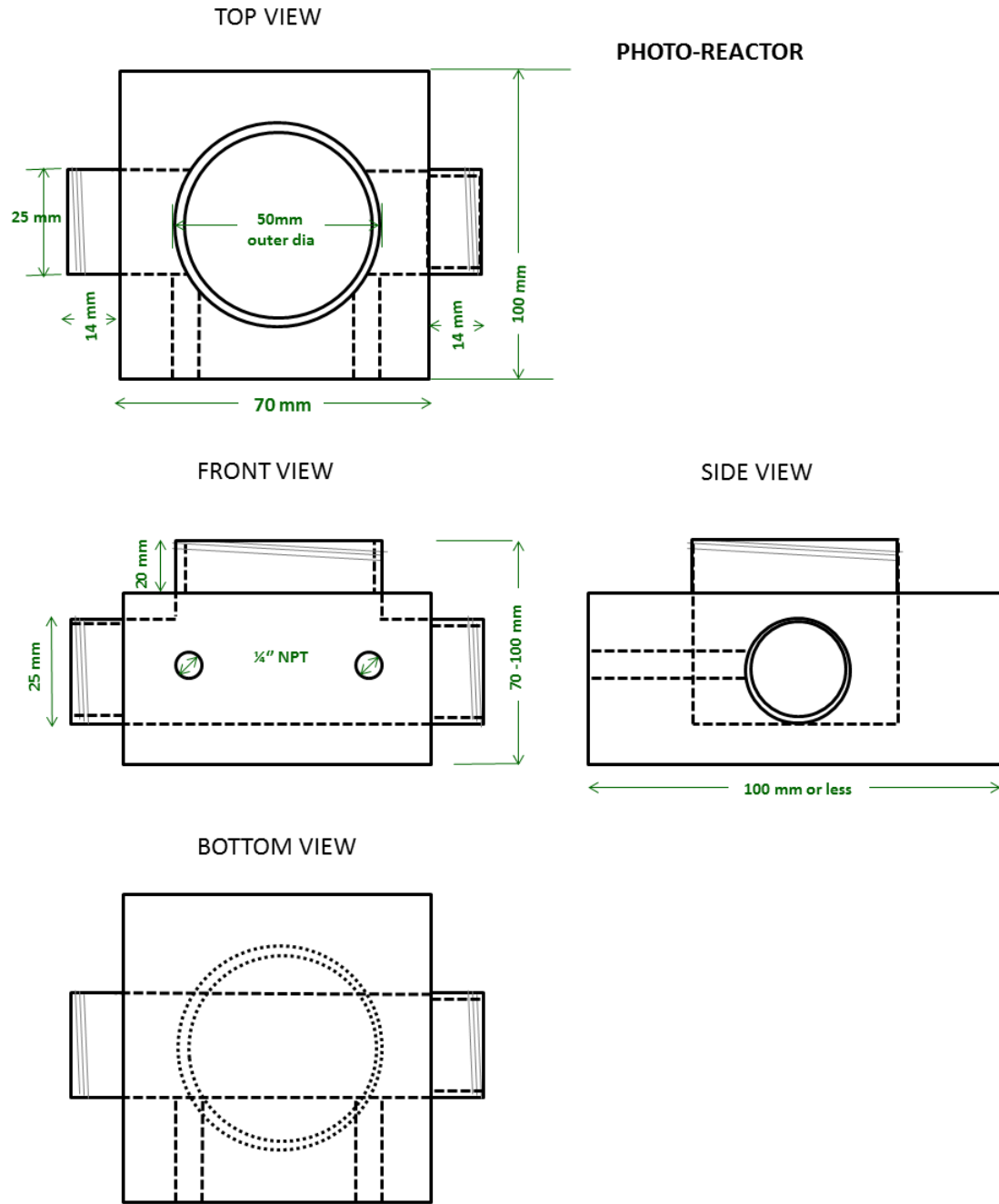
Figure 3.03. Mechanical drawings detailing the design of photoreactor body

FRONT VIEW
of reactor

END CAP

Description:
• Shows the arrangement of gaskets, windows, o-rings and end screw caps are assembled on the gas photo-reactor
•Material : aluminum

20 mm

25 mm

¼" NPT

Transparent window 3mm
(NT68-493)

O-ring - 0.103"
9559K163

PTFE Gasket 1/32"
(part # 1063T11)

Screw cap
with a hole
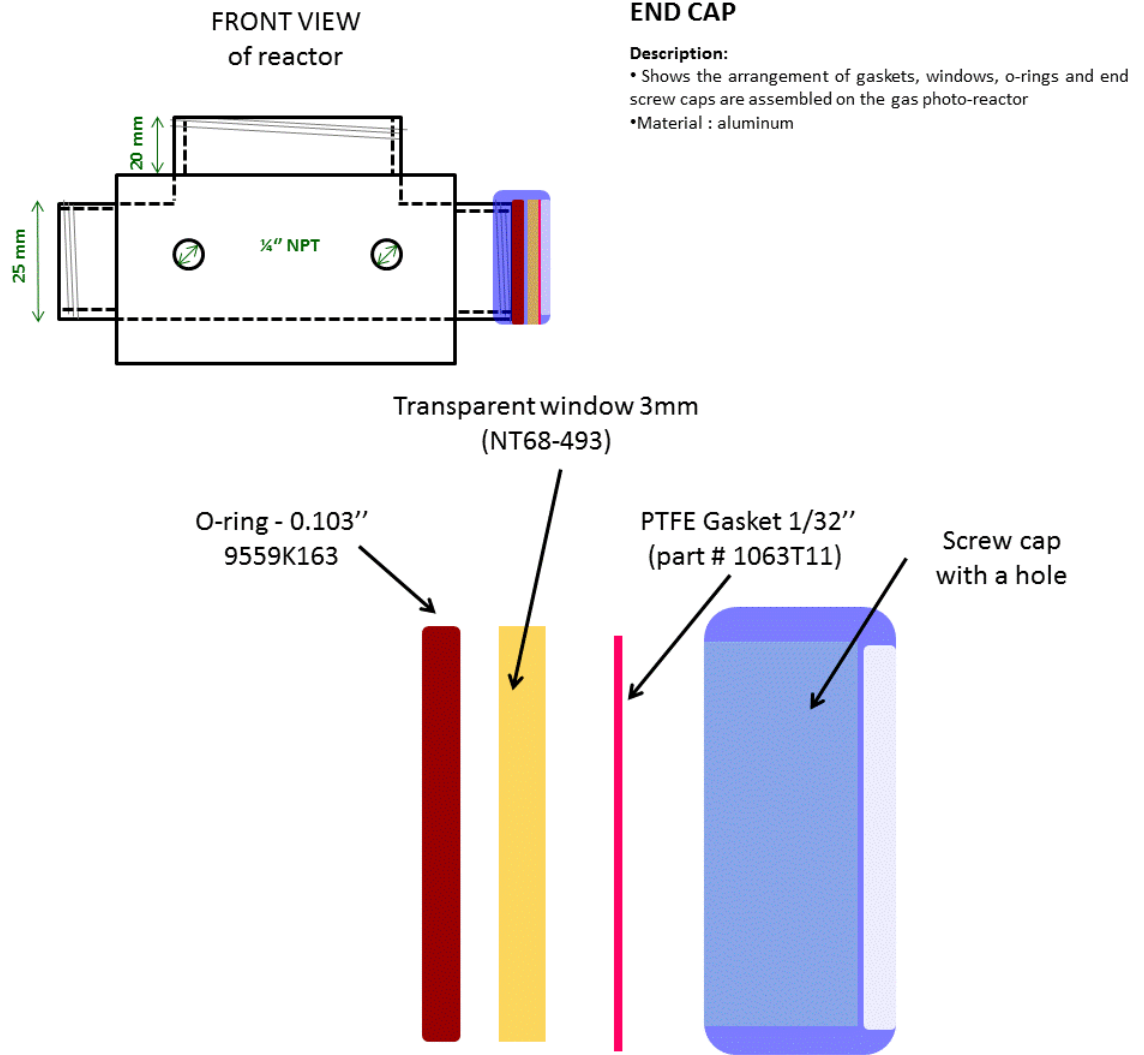
Figure 3.04. Design of end cap design used for the three windows in the of photoreactor

TOP VIEW

HOLDER

Description:
•Material : aluminum

Less than/equal
to 2.15 mm thick

FRONT VIEW

SIDE VIEW

75 mm

80 mm

40 mm

50 mm

BOTTOM VIEW

40 mm

Screws

80 mm
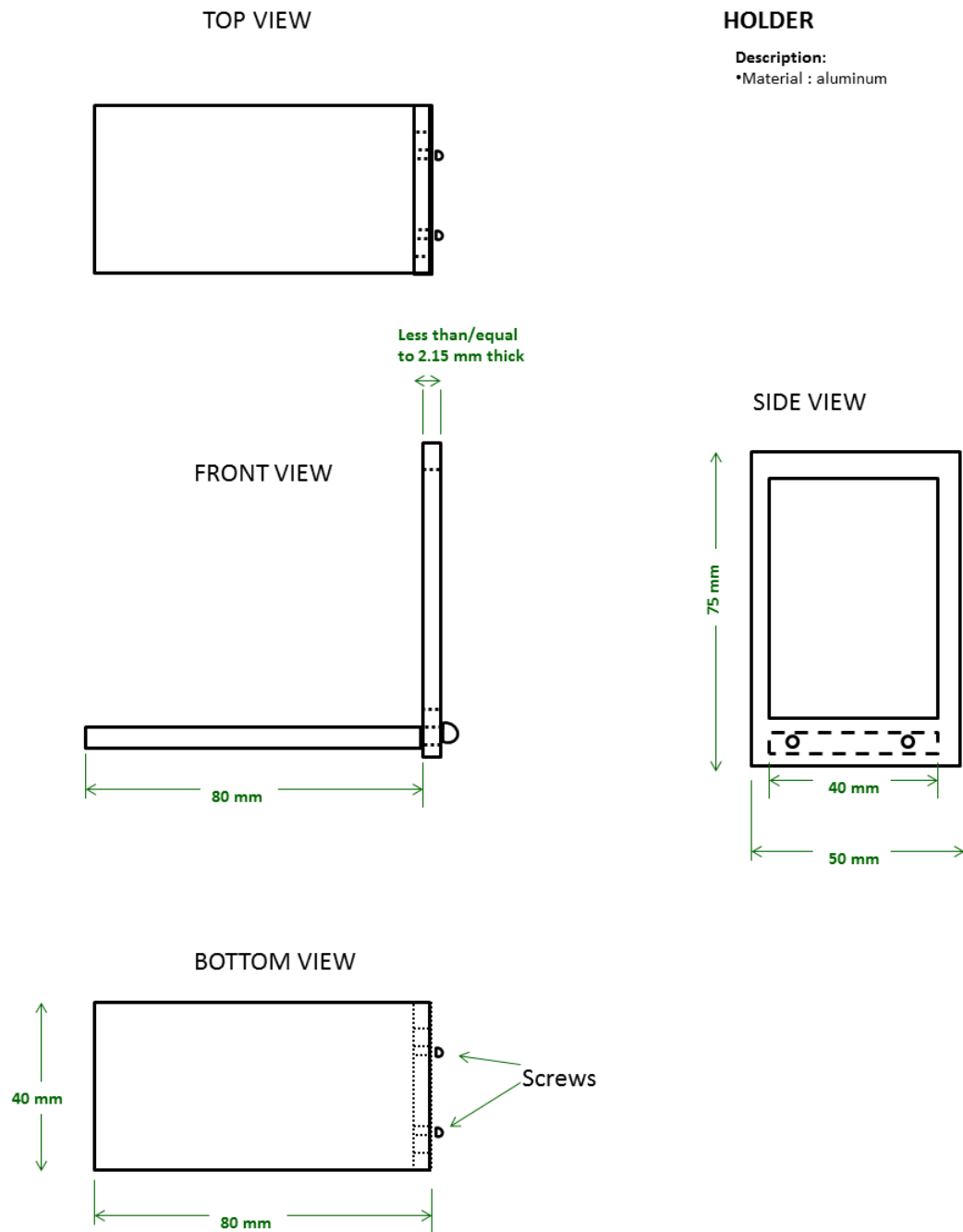
Figure 3.05. Schematic drawing of the holder used to place the photoreactor inside the FTIR setup

TOP VIEW
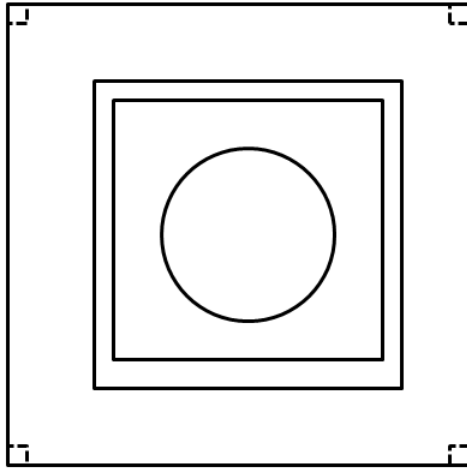
STAND

Description:

• 4 Legged table (7″ tall) with a circular hole in the center (dia =3.35″)

• a square fence (inner side = 4″) around the circular hole

FRONT/SIDE VIEW

4″

3.35″

7″
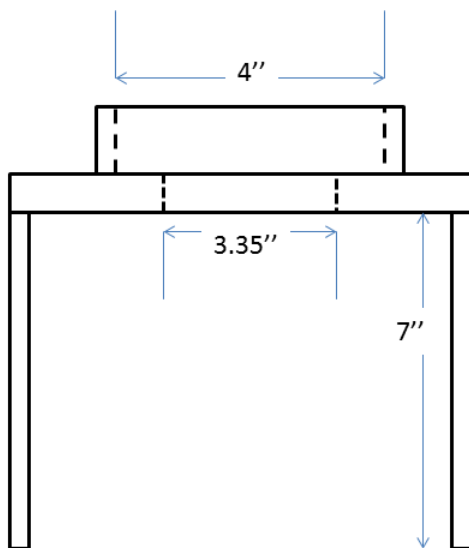
Figure 3.06. Sketch of the wooden stand used to place the UV lamp in a vertically downward position

TOP VIEW

~2 mm
thick

40 mm

~44 mm
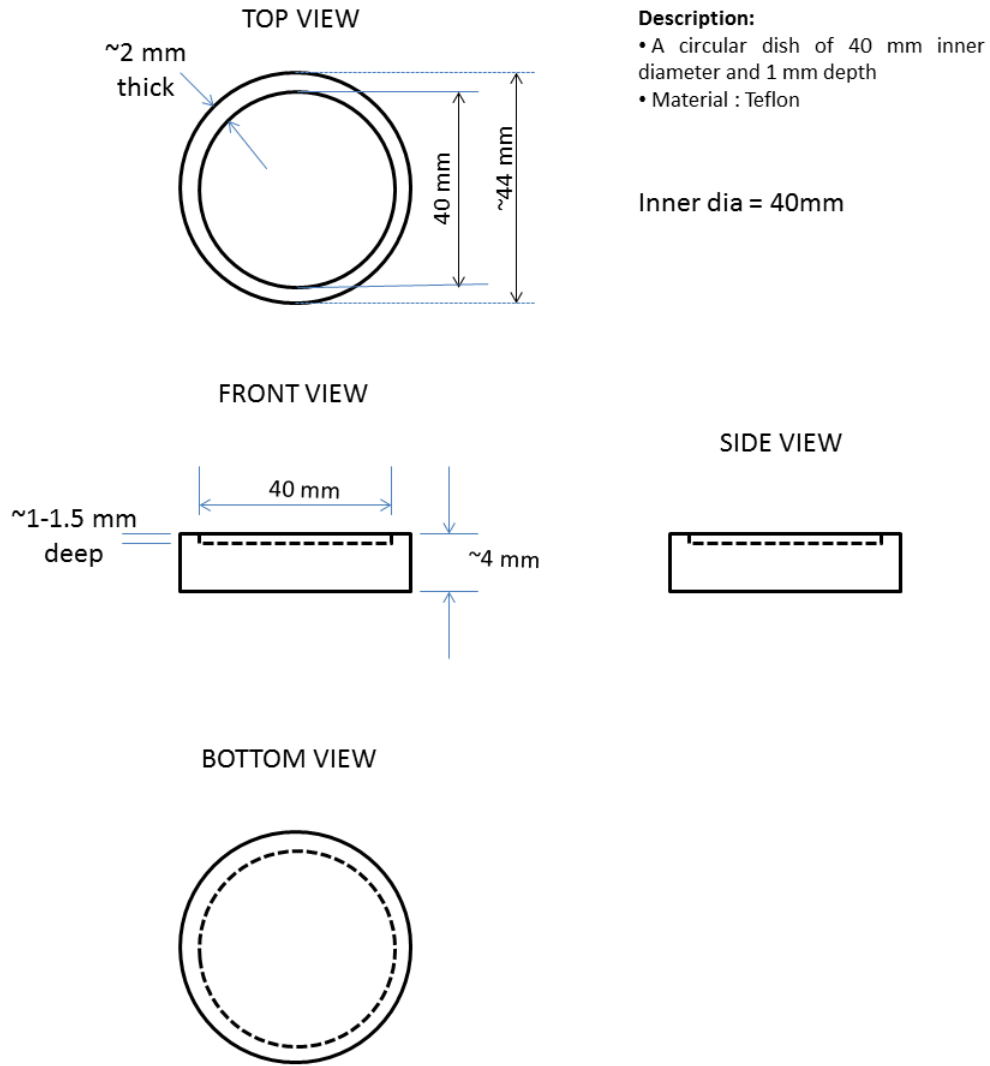
Description:
• A circular dish of 40 mm inner diameter and 1 mm depth
• Material : Teflon

Inner dia = 40mm

FRONT VIEW

40 mm

~1-1.5 mm
deep

~4 mm

SIDE VIEW

BOTTOM VIEW

Figure 3.07. Sketch of the sample dish used to place the photocatalyst powder

TOP VIEW
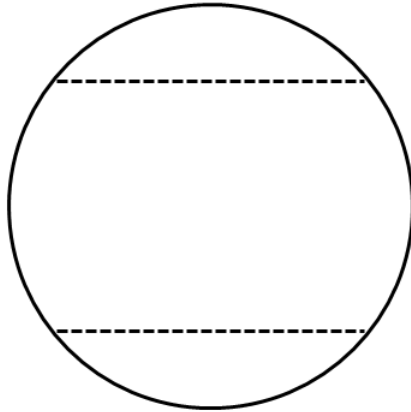
INSERT:
• A cylindrical shaped insert that was placed inside the photoreactor. This helped to reduce the overall reactor volume
• Material: Teflon

Inner dia = 40mm

FRONT VIEW
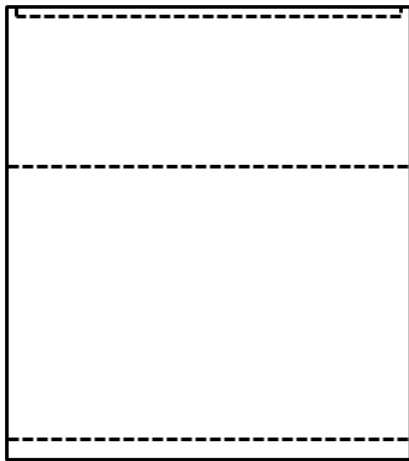
SIDE VIEW
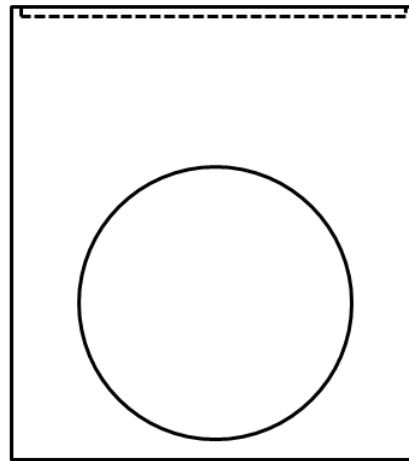
Figure 3.08. Drawing of the cylindrical block made of Delrin placed inside the photoreactor to reduce reactor volume
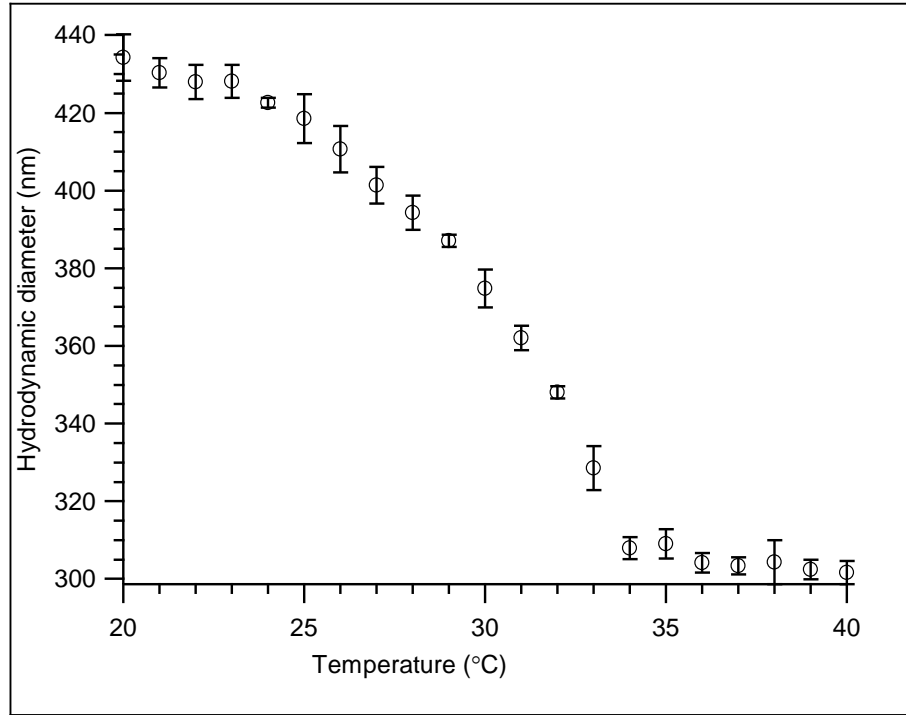
Figure 3.09. Temperature responsive of MPS/poly(NIPAAM-MBAA)
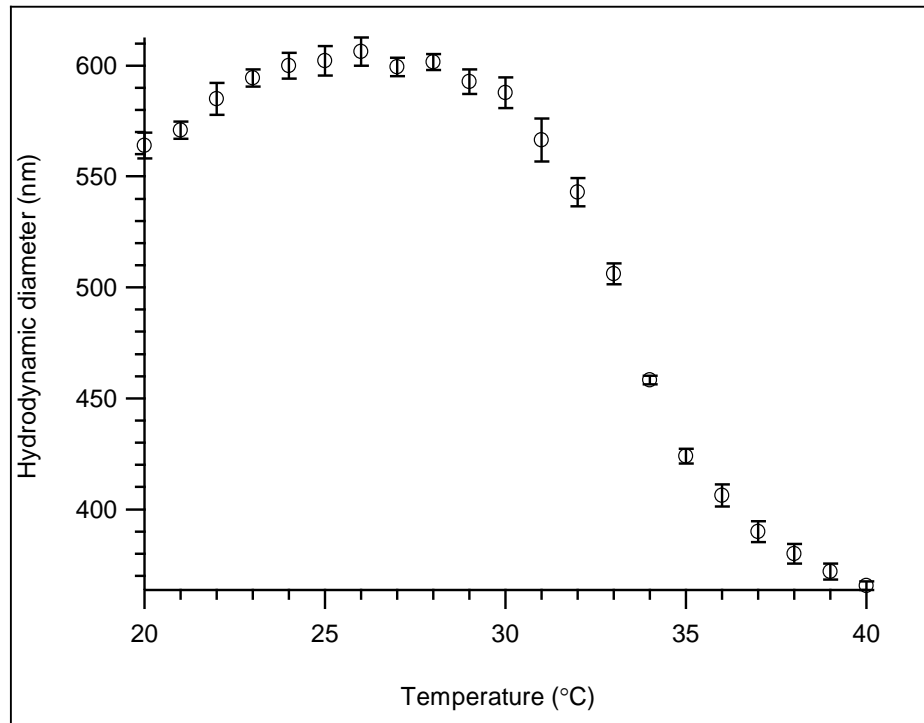
Figure 3.10. Temperature responsive behavior of AAEM / poly(NIPAAM-MBAA

73
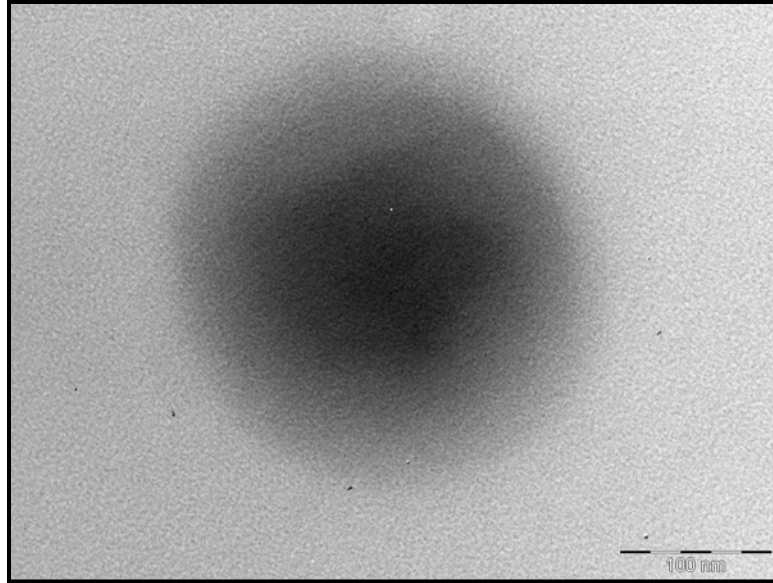
Figure 3.11. TEM image of MPS-poly(NIPAAM-MBAA)
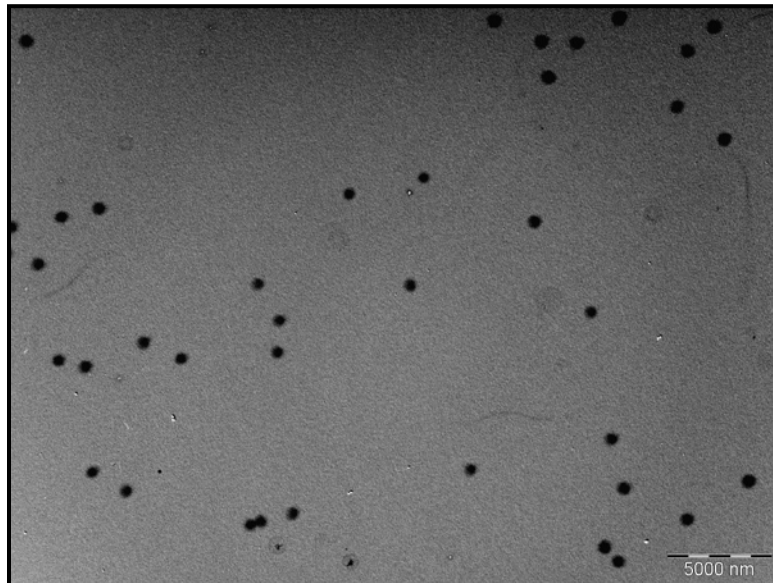
Figure 3.12. TEM image of AAEM-poly(NIPAAM-MBAA) (low magnification)

74
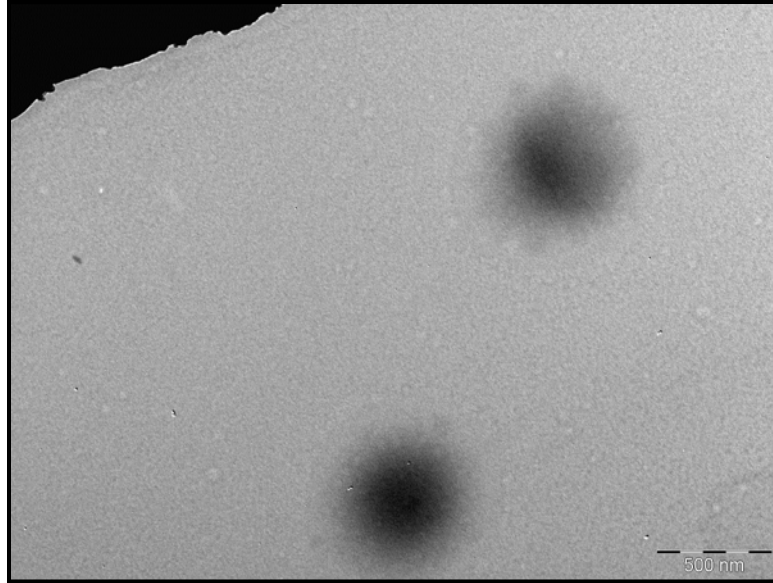
Figure 3.13. TEM image of AAEM-poly(NIPAAM-MBAA) (high magnification)
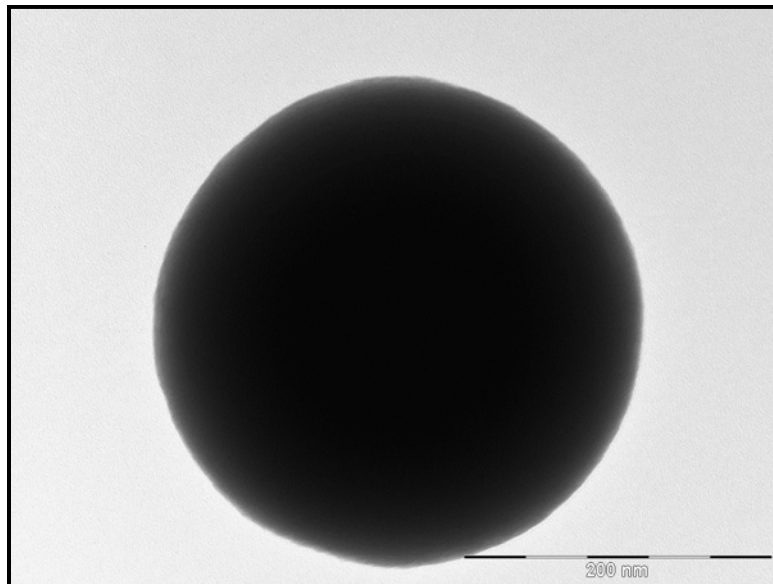
Figure 3.14. TEM image of NIPAAM-SiO$_2$

75
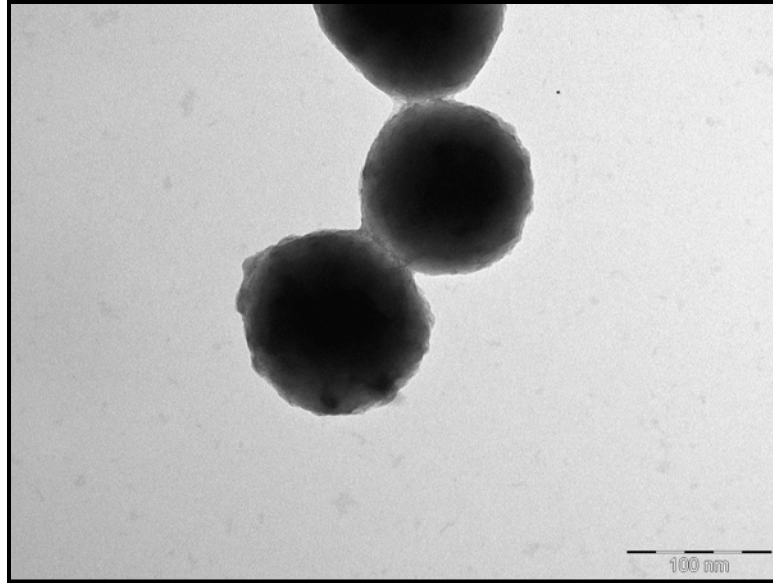
Figure 3.15. TiO$_2$ shell on MPS-SiO$_2$ using TBOT precursor
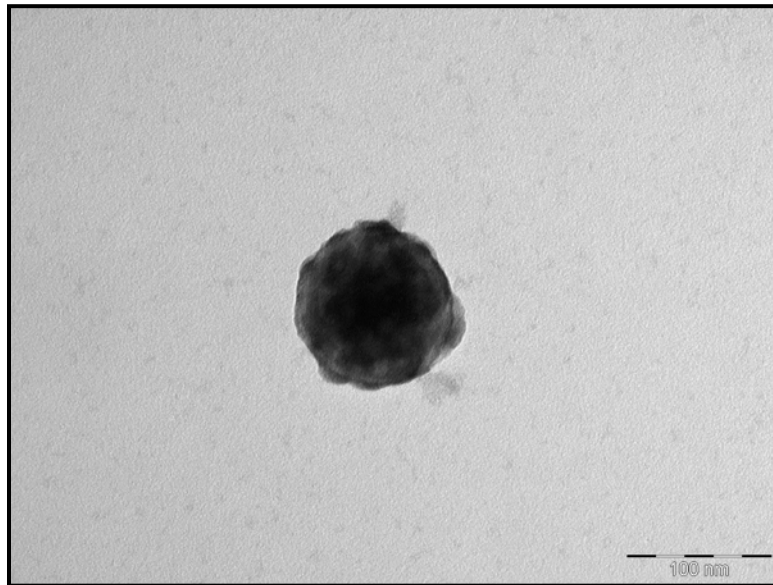
Figure 3.16. TiO$_2$ shell on AAEM-SiO$_2$ using TBOT precursor in the presence of NH$_4$OH

76
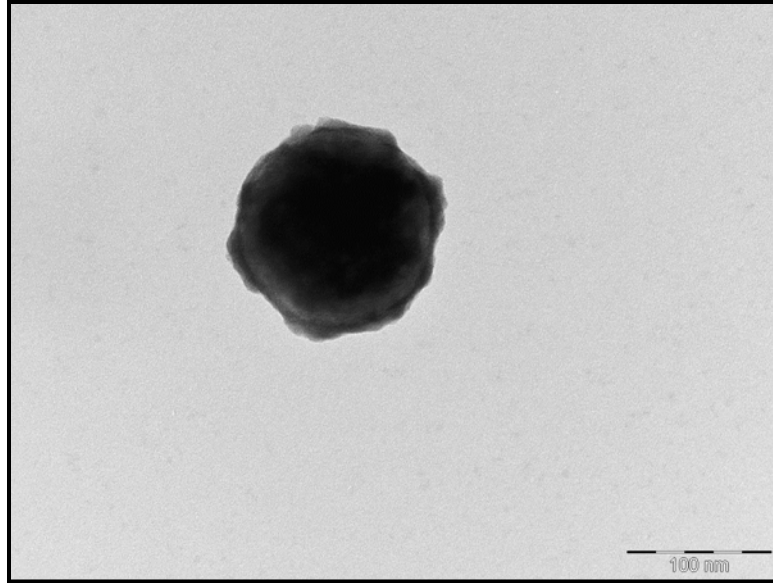
Figure 3.17. TiO$_2$ shell on AAEM-SiO$_2$ using TBOT precursor in the presence of acetonitrile
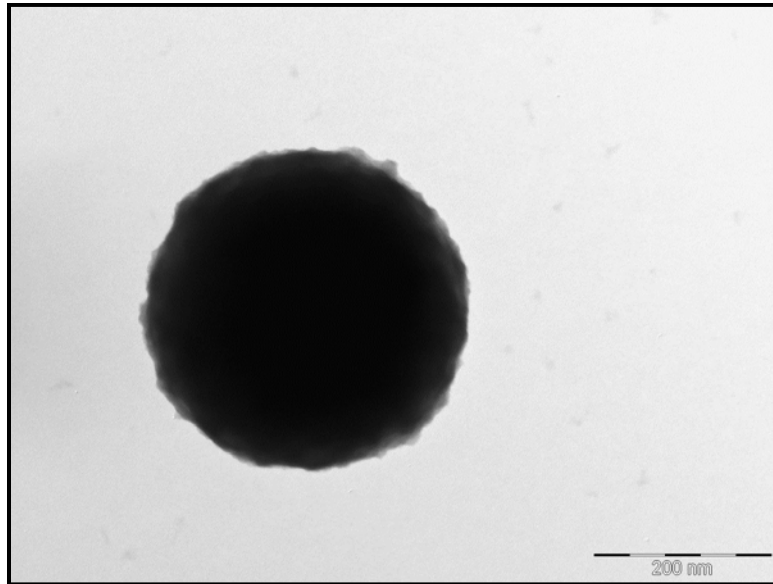
Figure 3.18. TiO$_2$ shell on PAA-SiO$_2$ using TBOT precursor in the presence of NH$_4$OH

77
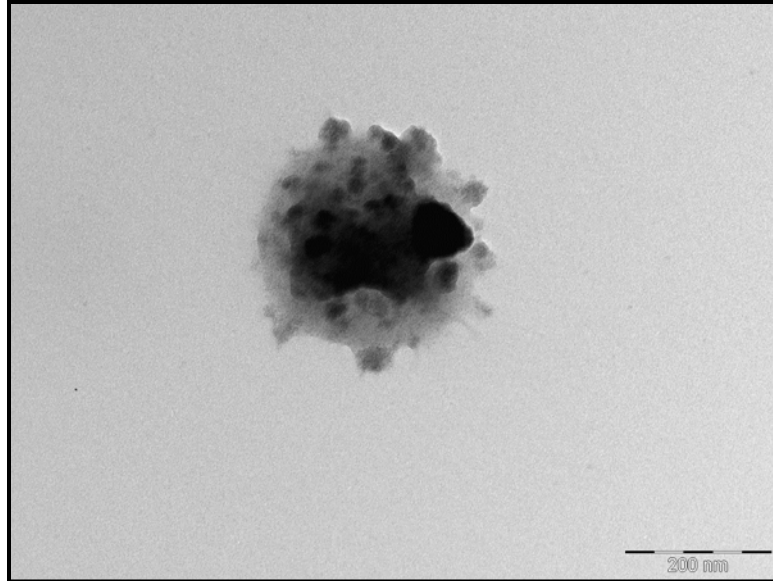
Figure 3.19. TEM of TiO$_2$ shell on MPS-poly(NIPAAM-MBAA) using TBOT
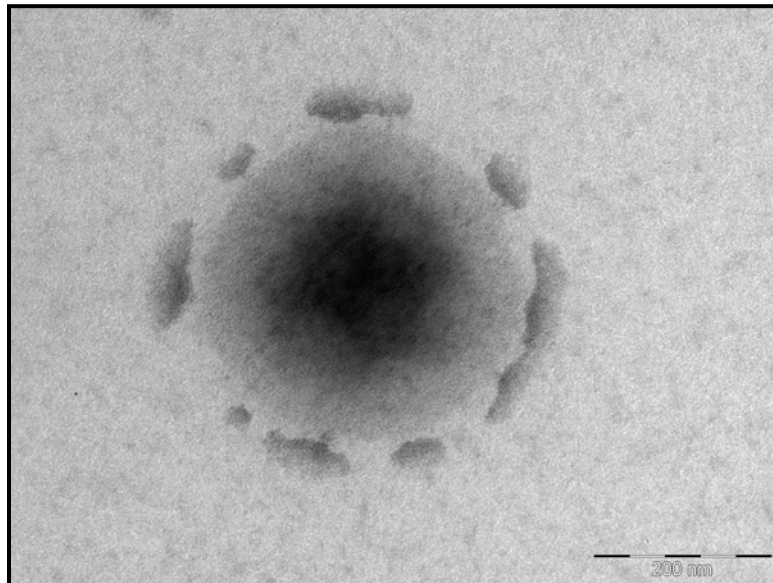
Figure 3.20. TEM of TiO$_2$ shell on MPS-poly(NIPAAM-MBAA) using TBOT
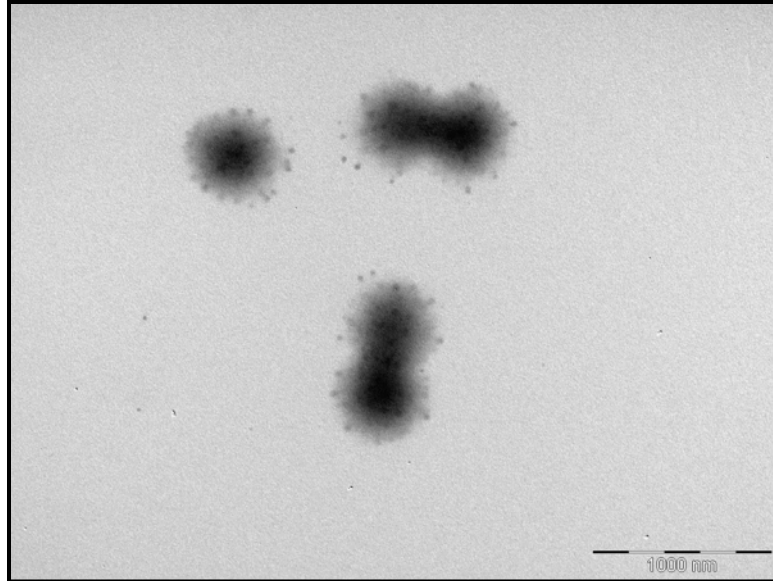
Figure 3.21. TEM of TiO_2 shell on AAEM -poly(NIPAAM-MBAA) using TBOT (low magnification)
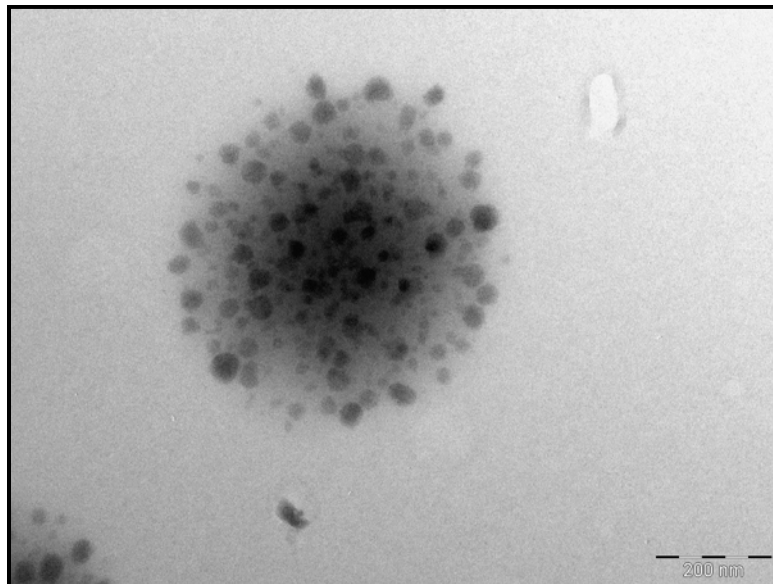
Figure 3.22. TEM of TiO_2 shell on AAEM -poly(NIPAAM-MBAA) using TBOT (high magnification)

79
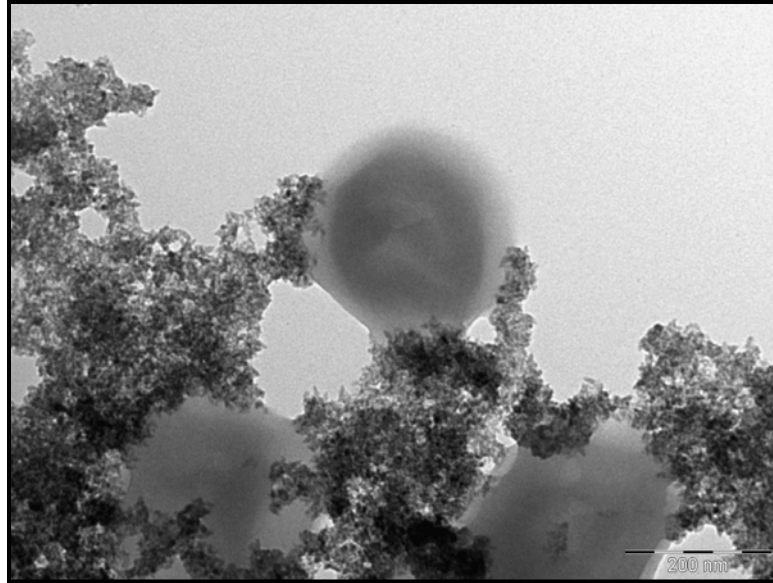
Figure 3.23. TEM of TS precipitation on MPS-poly(NIPAAM-MBAA) template
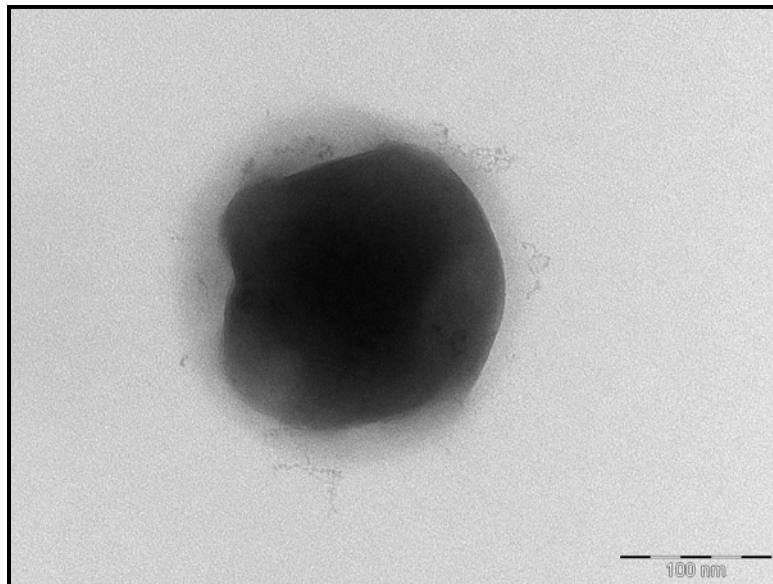
Figure 3.24. TEM of MPS-poly(NIPAAM-MBAA) template treated with TALH

80
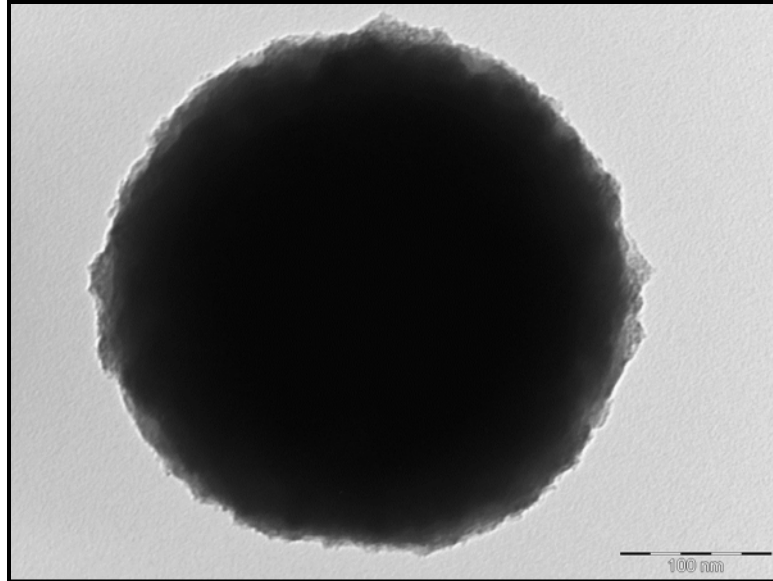
Figure 3.25. TEM of TiO_2 nanoshells prepared from TALH precursor and NIPAAM-SiO_2
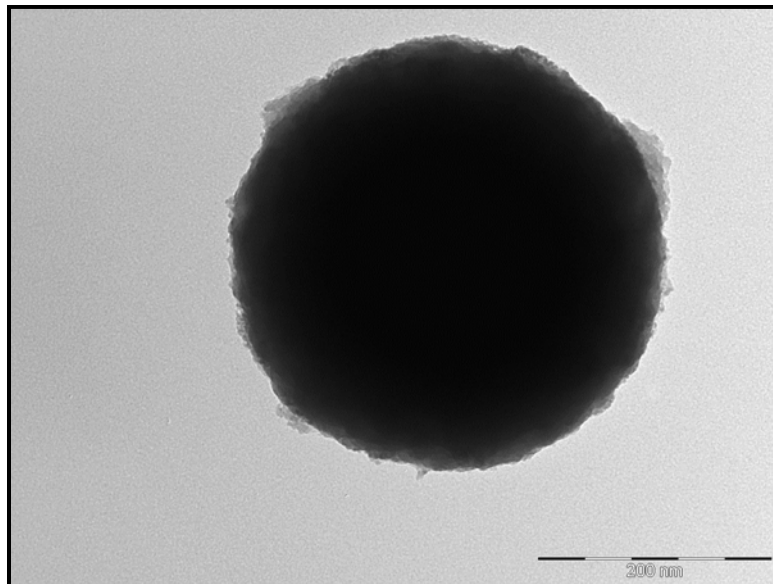
Figure 3.26. TEM of TiO_2 nanoshells prepared from TALH precursor and NIPAAM-SiO_2 after calcination
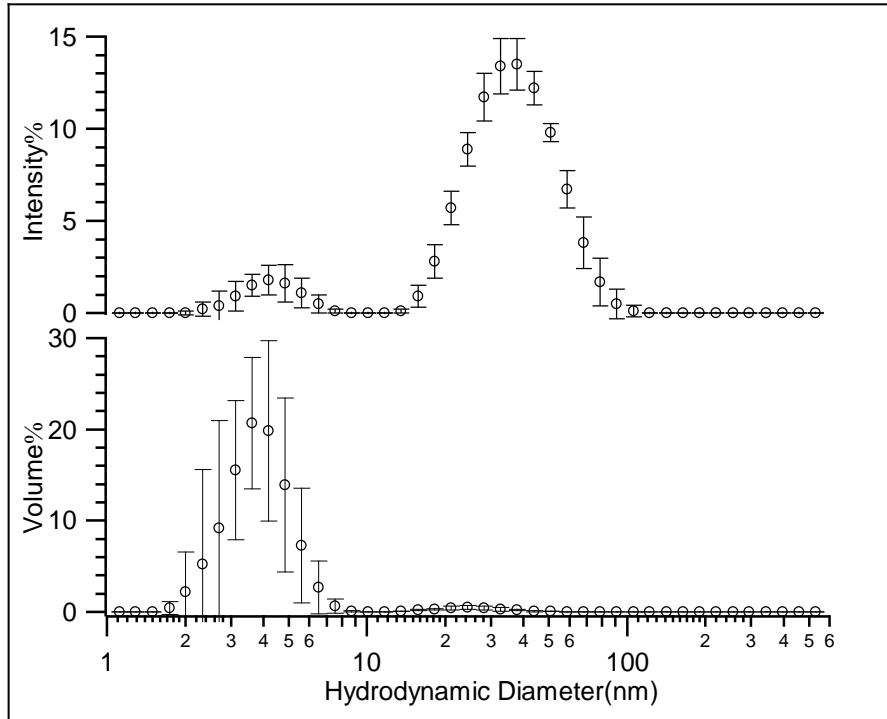
Figure 3.27. Size distribution of Pt nanoparticles from dynamic light scattering measurements
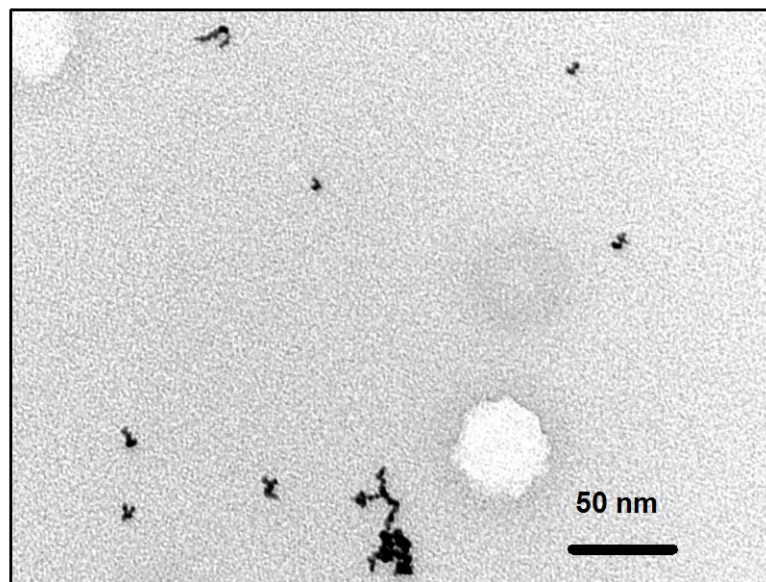
Figure 3.28. TEM image of Pt nanoparticles

82
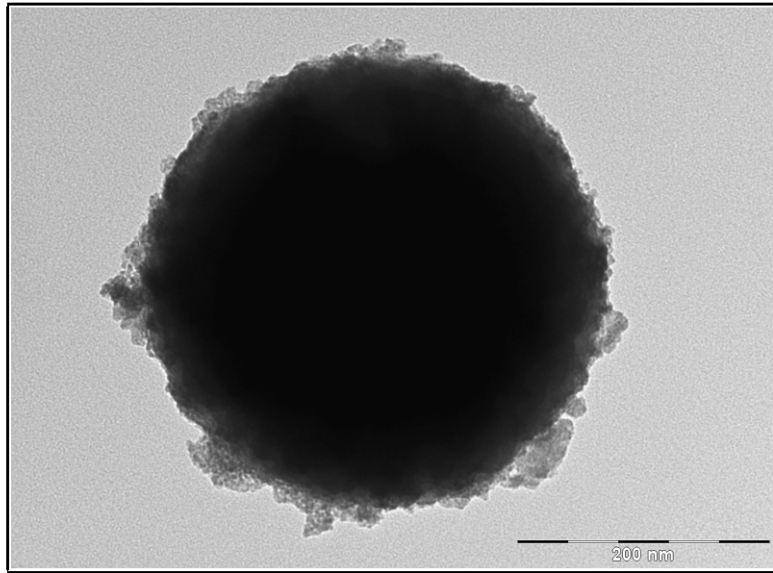
Figure 3.29. TEM image of Pt deposited TiO$_2$ nanoshells
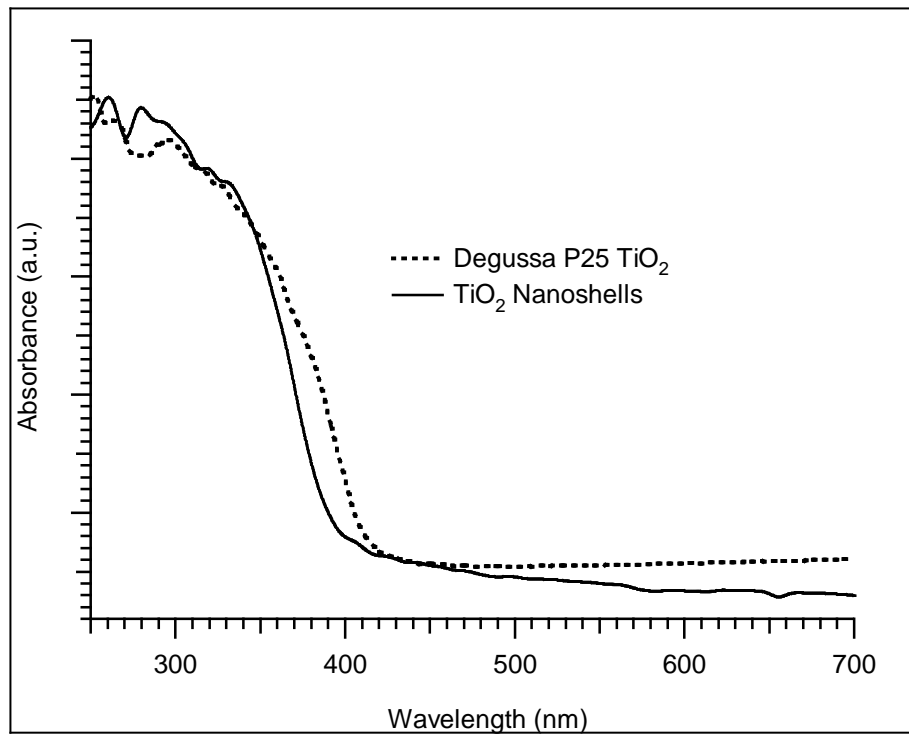
Figure 3.30. UV-Vis diffusive reflectance spectrum of the TiO$_2$ nanoshells

83
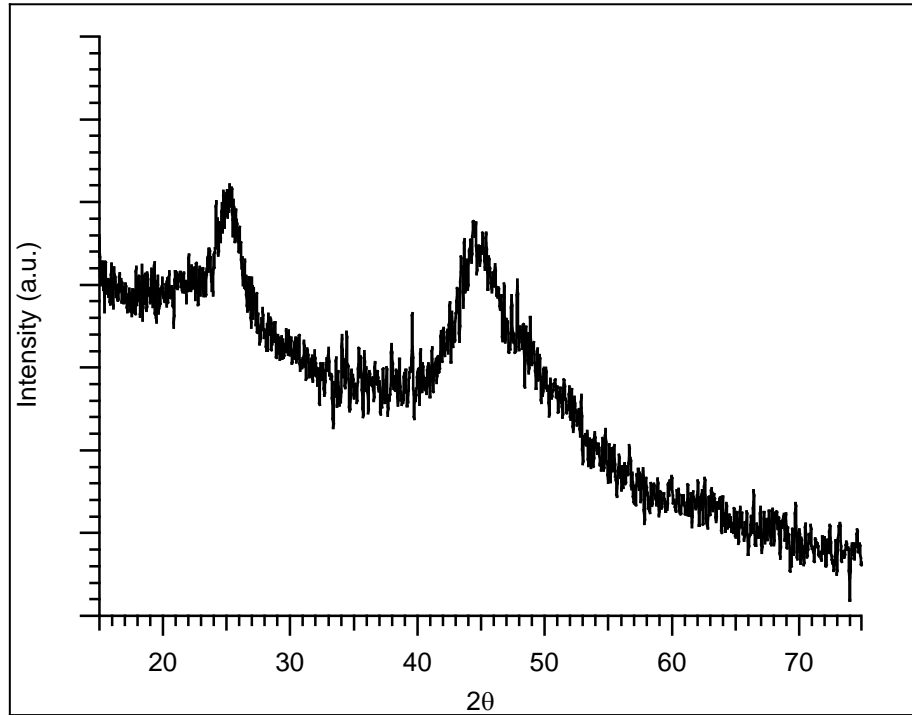
Figure 3.31. XRD diffraction pattern of TiO_2 nanoshell composites prepared on NIPAAM-SiO_2
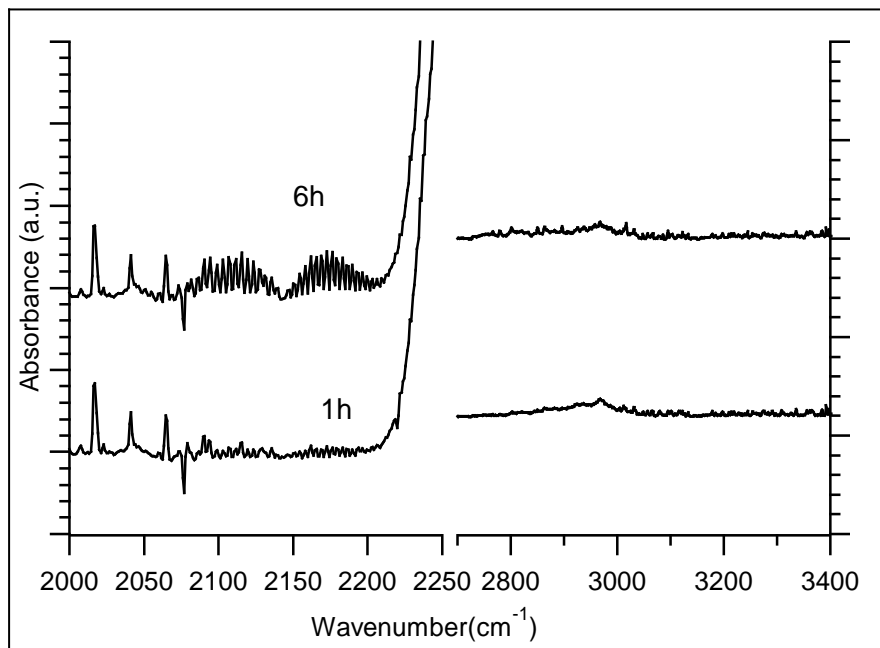
Figure 3.32. FTIR spectra of CH_4 and CO formation observed for TiO_2 nanoshell composite. A split x-axis is used for the wavenumber scale.

84
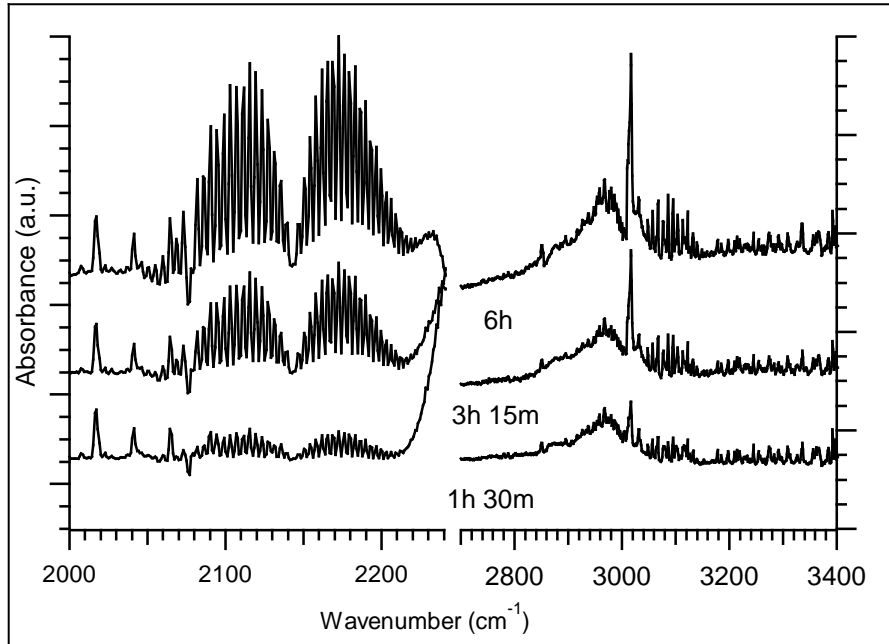
Figure 3.33. FTIR spectra of CH_4 and CO formation observed for Pt deposited TiO_2 nanoshell composite. A split x-axis is used for the wavenumber scale.
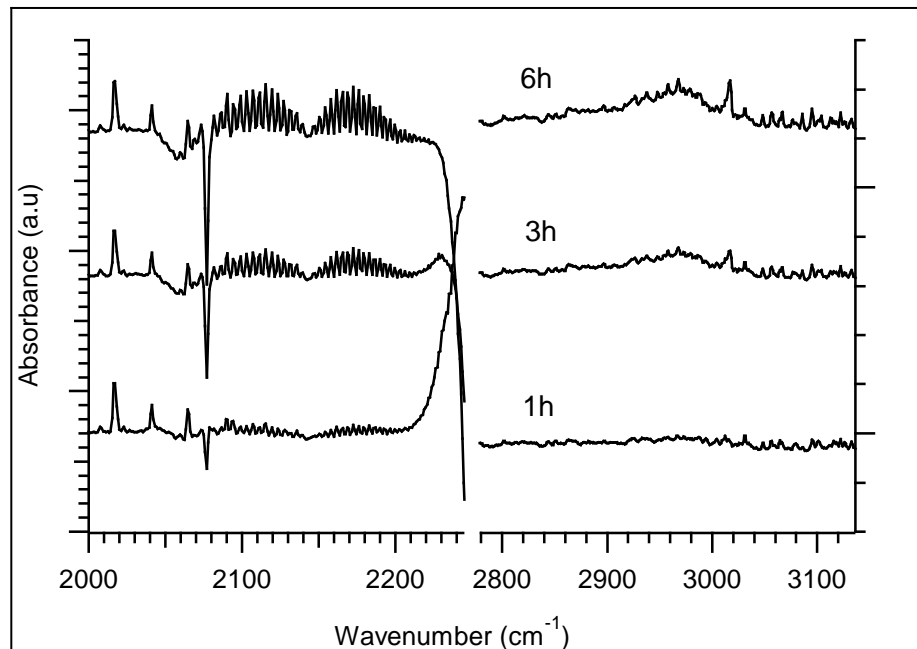
Figure 3.34. FTIR spectra of CO and CH_4 formation for P25 TiO_2 during photoreduction. A split x-axis is used for the wavenumber scale.

85
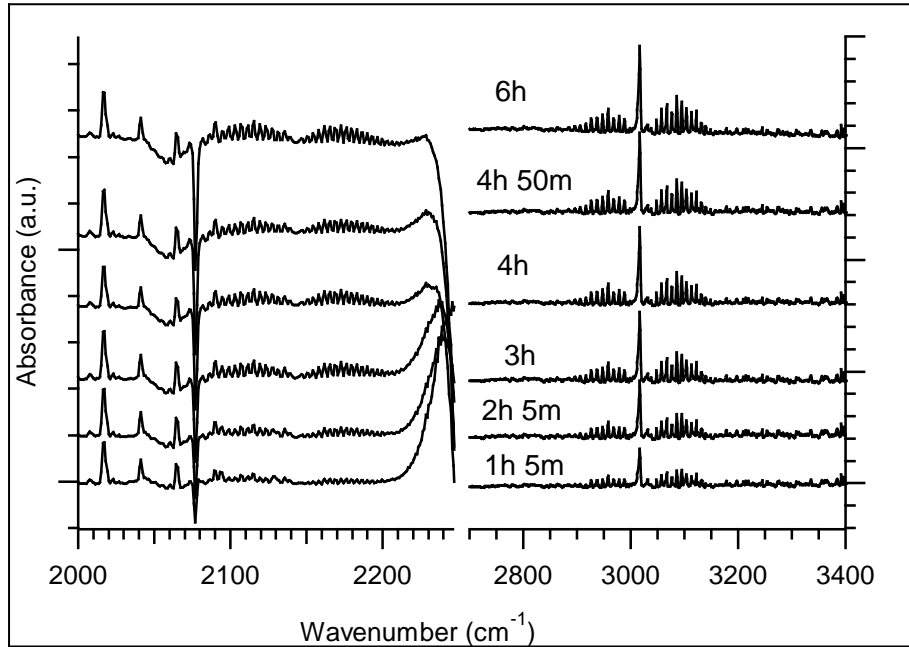
Figure 3.35. FTIR spectra of CO and CH4 formation from Pt deposited P25 TiO_2 during photoreduction. A split x-axis is used for the wavenumber scale.
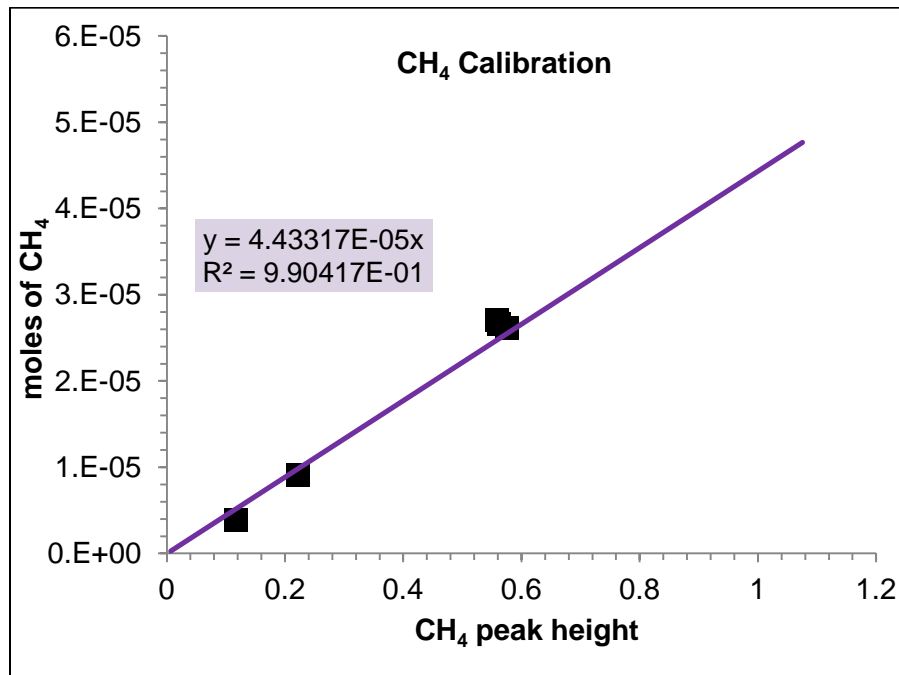
Figure 3.36. Calibration curve for relating CH_4 concentration to 3015 cm^{-1}peak height in a FTIR spectrum

86
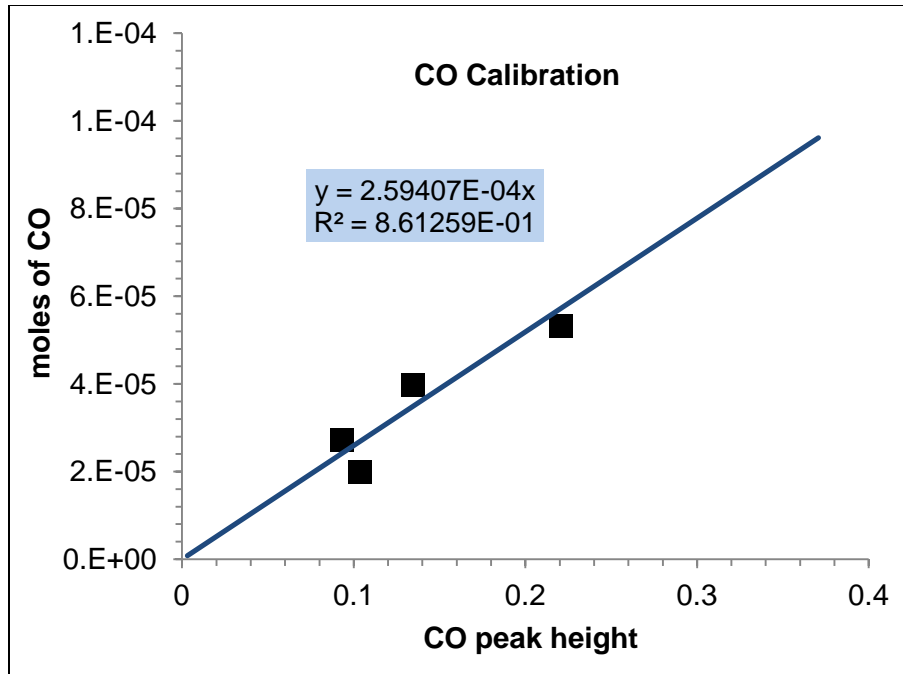
Figure 3.37. Calibration curve for relating CO gas concentration to 2172 cm^{-1} peak height in a FTIR spectrum
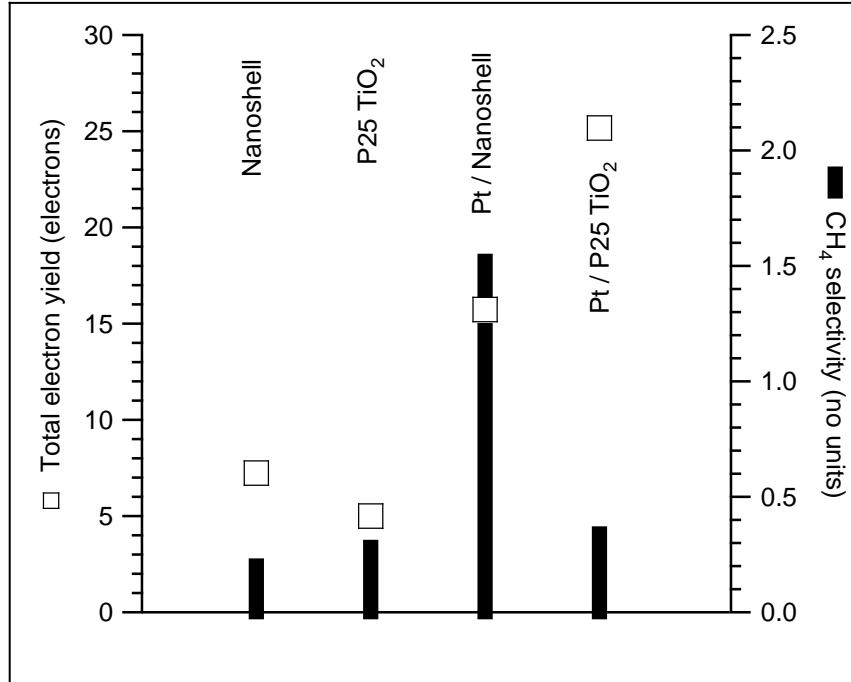
Figure 3.38. Photocatalytic performance of composites of TiO$_2$ nanoshells and P25 TiO$_2$

87

CHAPTER 4: BIMETALLIC AND CORE-SHELL PLASMONIC NANOPARTICLES TO ENHANCE CARBON DIOXIDE PHOTOREDUCTION

In this chapter, we describe syntheses and characterization of nanoparticles with different composition and structure that has unique physical, chemical and optical properties. Ag, Pt and bimetallic Ag-Pt nanoparticles, and $Ag@SiO_2$ core-shell nanoparticles were prepared to understand the role of structure-property relationships for catalytic photoreduction of CO_2. Commercially available P25 TiO_2 was used as the primary photocatalyst and its performance was enhanced by deposition of co-catalytic and plasmonic nanoparticles on its surface. These nanoparticles comprised of Ag, Pt or bimetallic Ag-Pt nanoparticles and $Ag@SiO_2$ core-shell nanoparticles. Various characterization tools were used to study the properties of nanoparticles. CO_2 photoreduction reactions were performed using a home built photo-reactor and the results are presented to establish principles for rational design of nanoparticles that can enhance photoreduction of CO_2 with titania, which is a widely available and stable material.

4.1 Experimental details and material characterization

4.1.1 Synthesis of Ag, Pt and Ag-Pt nanoparticles

In this chapter, we have explored Ag and bimetallic Ag-Pt co-catalyst nanoparticles for two reasons. First, even though Pt metal has been used widely in the past for a multitude of catalytic reactions, Pt is approximately 50 times more expensive

88

than Ag[83]. Secondly, Ag and bimetallic Ag-Pt nanoparticles lead to distinct optical properties. For example, Ag nanoparticles have characteristic absorbance band in the near UV region whereas the bimetallic Ag-Pt nanoparticles can show absorbance in the visible spectrum depending on the composition of the particles.

Ag nanoparticles were synthesized by adding 200μL of freshly prepared 112 mM $NaBH_4$ to a 10 ml aqueous solution of 1 mM $AgNO_3$ and 3.1 mM citric acid, trisodium salt dihydrate[179]. The color of solution turned dark green-yellow immediately after the addition of reducing agent $NaBH_4$. Approximately 240 mg of polyvinylpyrrolidone, a stabilizing agent was added. The contents were stirred continuously and left overnight to allow residual $NaBH_4$ to decompose completely.

Another method known as Turkevich method was also used to prepare Ag nanoparticles[190, 191]. Typically, 20 ml silver salt solution of 1 mM $AgNO_3$ concentration was heated to 110°C. When the solution started to bubble 0.4 ml of 38.8 mM sodium citrate solution was added rapidly[192]. The solution was refluxed under N_2 gas for 1 h.

Pt nanoparticles were prepared from $NaBH_4$ reduction method similar to Ag nanoparticle preparation mentioned above. Typically, 200 μL of 112 mM $NaBH_4$ was rapidly added to a 10 ml of aqueous solution containing 1 mM K_2PtCl_6 and 3.88 mM citric acid, trisodium salt dehydrate. The reduction of Pt salt to metallic nanoparticles of Pt was confirmed from the change in solution color upon $NaBH_4$ addition.

89

To prepare Ag-Pt bimetallic nanoparticles, a specific volume of 1 mM K_2PtCl_4 was mixed with Ag nanoparticle colloids such that the initial volume percentage of Pt salt was set to four different values: 4, 6.7, 10 and 20.   The resulting particles are referred to as Ag-Pt(4), Ag-Pt(6.7), Ag-Pt(10), and Ag-Pt(20).

When Pt salt was added, silver atoms on the surface of Ag nanoparticles were replaced by Pt ions according to the galvanic replacement reaction[193] as shown below.

$$PtCl_{6(aq)}^{2-} + 4\,Ag_{(s)} \rightarrow Pt_{(s)} + 4Ag_{(aq)}^{+} + 6Cl_{(aq)}^{-}$$
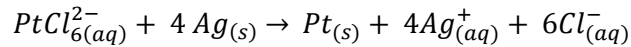
Since four Ag atoms are replaced by one Pt atom, a non-epiaxial growth of Pt layer proceeded resulting in a partially covered Pt shell around the Ag core with lower Pt concentration, and to a fully covered shell as Pt concentration was increased. Careful control over the Pt salt addition is necessary in this synthesis as an increase in Pt salt can cause the shell to dissolve into islands of Pt when diffusion of Pt and Ag ions takes place along the Pt shell[194, 195].

Ag, Pt, and bimetallic Ag-Pt nanoparticles were analyzed using TEM and UV-Vis absorbance spectroscopy to characterize nanoparticle size, shape and optical behavior.

4.1.2 Core-shell Ag@SiO₂ plasmonic nanoparticle synthesis

To create a SiO_2 shell on Ag nanoparticles, TEOS diluted in ethanol was added immediately after Ag nanoparticles were prepared (approximately 5-10 min after the green-yellow color was observed when the Ag nanoparticles were synthesized). The

90

deposition of SiO_2 coating was initiated by the addition of dimethylamine into the solution[196]. The final concentrations of TEOS, DMA and water (from Ag colloids) were approximately 7 mM, 0.6 M and 14 M respectively. To create a SiO_2 shell on the Ag nanoparticles prepared using Turkevich method, heating was stopped during the Ag particle preparation and the hot Ag nanoparticle colloidal solution was allowed to cool to room temperature. Then 10 ml silver nanoparticle colloid was added to a 28 ml ethanol bath containing 70 µL TEOS. After 1-2 min of stirring the contents well, 1.75 ml of DMA was added. The core-shell $Ag@SiO_2$ nanoparticles were analyzed using TEM and UV-Vis absorbance spectroscopy.

4.1.3 Preparation of TiO_2 photocatalyst nanocomposite

Commercially available Aeroxide^{TM} P25 TiO_2 was used for all experiments. Co-catalyst deposited TiO_2 photocatalyst composites were prepared by adding 4ml of Ag, Pt or Ag-Pt colloid solutions to ~1 gm of TiO_2. The contents were sonicated 15 min and vortex mixed for 6 h. To separate out the solvent, the sample was centrifuged at 8,500rpm for 40min. The supernatant was decanted and the nanocomposites were redispersed in water. The purification steps of redispersing and centrifuging were repeated three more times. The final precipitate was dried in vacuum and stored in dark to avoid interaction with ambient light.

To prepare TiO_2 photocatalyst composite containing plasmonic $Ag@SiO_2$, samples were prepared by mixing 7.5ml of $Ag@SiO_2$ colloidal solution with the above photocatalyst composites. Purification steps were done 3-4 times to remove remnant organic residues of PVP and solvents.

91

4.1.4 CO_2 photoreduction experimental setup

Photoreduction experiments were carried out in the home-built aluminum reactor described in chapter 3 (section 3.1.4). Only a brief description of the reactor features will be mentioned in this chapter. For detailed drawings, refer to chapter 3, figures 3.2-3.8. The aluminum reactor has two ports for inlet and outlet flow for gases. The reactor had three optical windows - one glass window at the top for photoirradiation and two ZnSe windows on two sides for infrared measurements. Approximately 1gm of the photocatalyst was filled and leveled into a circular Teflon dish. All other reaction parameters and pretreatment conditions were similar to the photoreduction experiments mentioned in chapter 3. Photo-irradiation was performed in a batch mode for 6 h using a 100 W Hg lamp. The hydrocarbon formation inside the photo-reactor was measured using a Magna-R 860 FTIR spectrometer (Nicolet, WI, USA). The peak responses of CH_4 and CO from FTIR analysis were obtained using a separate calibration of the FTIR signal to known quantities of CH_4 and CO. The calibration curves are given in figures 3.36 and 3.37.

4.2 Results and discussion

4.2.1 TEM, DLS and UV-Vis analysis of nanoparticles

When Ag nanoparticles were formed, the transparent, colorless solution changed to a yellow-green color. Ag nanoparticles were measured to be ~10nm in size from TEM images as shown in figure 4.1. Figures 4.2 and 4.2 are TEM images of Ag-Pt bimetallic nanoparticles synthesized by adding different amounts of Pt salt into the Ag hydrosol. These TEM images suggest that there were structural changes to Ag nanoparticles when Pt salt was added. The TEM image in figure 4.3 shows dotted circular features that

92

may be due to the dissolution of the Ag atoms in the core during the galvanic replacement process. Similar observations have been reported previously. [194, 195]

DLS was used to measure the hydrodynamic diameter of Ag, Pt and bimetallic Ag-Pt nanoparticles. Figures 4.4 and 4.5 depict size distribution of particles for Ag and Ag-Pt nanoparticles. From the intensity distribution plots shown in figure 4.4, we can see that the particle sizes are in two ranges; one in the 10nm range and the other in the 100nm range. The volume% plot in figure 4.5 suggests that the colloidal solutions are fairly uniform in size with only a small population of particles in the 100nm range. The two figures can be also used to understand how the addition of Pt salt modifies the particle structure. From figure 4.4 it was observed that the peak maximum of first peak was centered at 6.5 nm for Ag nanoparticles. As Pt was added, there was initially a slight increase in nanoparticle size. For the Ag-Pt(10) sample, we observe a small shoulder peak at 4 nm suggesting nanoparticles are beginning to rupture to smaller sizes. However, the intensity% plot in figure 4.5 suggests that the percentage of nanoparticles in the 4 nm size range was fairly negligible.

Pt nanoparticle size and morphology were characterized similarly using TEM and DLS. The TEM and DLS characterization of Pt nanoparticles are detailed in chapter 3. Figure 3.27 show the intensity% and volume% plots obtained from DLS analysis. These plots suggest that the average nanoparticle size of pure Pt nanoparticles were ~5 nm. The second peak at ~50nm in the figure 3.27 may be due to aggregation of Pt nanoparticle. The aggregations of Pt nanoparticles into lumps of 40-100nm sizes were also observed from TEM analysis as seen in figure 3.28.

93

The optical responses of Ag, Pt and bimetallic Ag-Pt nanoparticles were measured using UV-Vis spectroscopy. Figure 4.6 depicts the absorbance measured for these colloidal nanoparticles. As Pt content increased, there was a red-shift of the peak maximum as well as a decrease in the intensity of absorption. Pure Pt nanoparticles show no peaks in the near UV or visible regions. The optical band of Ag nanoparticles synthesized via $NaBH_4$ reduction method is centered at 386nm. The peak maximum shifts by ~30 nm and the intensity of the peak dropped by 50% for sample prepared from Pt salt solution of 10 vol% in the Ag colloidal solution. For samples with 20% Pt salt concentration, the absorbance intensity decreases by a factor of ~4. Therefore, we observe different optical properties of bimetallic Ag-Pt nanoparticles compared to pure Ag or Pt nanoparticles.

The TEM and UV-Vis spectra were analyzed for $Ag@SiO_2$ nanoparticles to understand the nanoparticle size, morphology and absorbance bands. Figures 4.7 and 4.8 depict TEM images of Ag-core SiO_2 shell nanoparticles. The shell thickness was ~75nm for the $Ag@SiO_2$ nanoparticles with the Ag nanoparticle core size of ~10nm prepared earlier via $NaBH_4$ reduction method. Figure 4.9 depicts UV-Vis spectra shows a comparison of Ag nanoparticles and $Ag@SiO_2$ nanoparticles. The UV-spectra of $Ag@SiO_2$ had red-shifted by ~20nm.

Figure 4.10 shows the TEM analysis of Ag nanoparticles synthesized via Turkevich method. The silver nanoparticles formed are larger than nanoparticles synthesized via $NaBH_4$ reduction method. DLS measurements of these larger Ag samples prior to SiO_2 shell creation is depicted in figure 4.11. The DLS analysis suggests that there are two peaks where second peak was centered at ~50nm.

94

Therefore, there is reasonable agreement between the DLS and the TEM results. The UV-Vis absorbance spectra of Ag@SiO$_2$ synthesized is shown in figure 4.12. It was observed a shell causes a ~30nm red-shift in the peak of Ag@SiO$_2$ core-shell particles relative to the peak for pure Ag nanoparticles.

4.2.2 Photocatalytic performance of nanocomposites

The FTIR spectra were collected at various intervals of time during photoreduction inside the aluminum reactor. FTIR spectra obtained for P25 TiO$_2$ at different time intervals are depicted in Figure 4.13. The formation of CO was observed from bands at 2140 and 2170 cm^{-1} and formation of CH$_4$ was confirmed by the peak at 3017 cm^{-1}. It was observed that the primary product from P25 TiO$_2$ was CO. Similar FTIR spectra obtained from TiO$_2$ composites prepared by mixing TiO$_2$ with Pt, Ag, bimetallic Ag-Pt(4), Ag-Pt(6.7) and Ag-Pt(10) are shown in figures 4.14-4.18. It was evident from the FTIR analysis that the product yields and the selectivity of products were different when co-catalysts of different elemental composition were used. Figures 4.19-4.23 shows the FTIR spectra of CO and CH$_4$ obtained using plasmonic Ag@SiO$_2$ core-shell nanoparticles mixed with above mentioned samples such as P25 TiO$_2$, and P25 TiO$_2$ with Ag, Pt, bimetallic Ag-Pt(6.7) and Ag-Pt(10). In all cases, the CO and CH$_4$ formation increased with time.

The yields obtained after 6 h of photo-irradiation are summarized in figure 4.24. The total electronic yields in figure 4.24 suggest that plasmonic Ag@SiO$_2$ core-shell nanoparticles have enhanced photocatalytic activity. We believe that plasmonic Ag@SiO$_2$ increases the overall yield by generating electron-hole pairs to participate in redox reactions. P25 TiO$_2$ forms CO as a primary product during CO$_2$ photoreduction.

95

With the addition of plasmonic nanoparticles, there was an increase in CO production on P25 TiO_2. On the other hand, when a metal such as Ag or Pt is in contact with a semiconductor, there is a tendency for the electrons from the TiO_2 conduction band to flow towards Ag (or Pt) surface. In the case of core-shell nanoparticles, this electron flow was reduced by the SiO_2 coating. Photo-reactions thus occurred on TiO_2 semiconductor surface alone. This could have been the reason for similar product selectivity for P25 TiO_2 and Ag@SiO_2 on TiO_2. When Ag, Pt and bimetallic Ag-Pt nanoparticles are used, the photo excited electrons in the TiO_2 conduction band are pulled by the metal nanoparticles due to their co-catalytic nature. For bimetallic Ag-Pt co-catalyst, an improvement in yield was observed compared to pure Pt or Ag, as shown in figure 4.24.

By combining plasmonic effect and co-catalytic effect we observe an 8-fold increase in electronic yield compared to P25 TiO_2. Lower yields were observed for Ag co-catalysts or Ag co-catalysts combined with plasmonic nanoparticles than their Pt counterparts. This is because, due to the plasmonic nature of Ag, quantized charging was induced by the incident light that results in accumulation of conduction electrons. [188, 189] As a consequence, the overall Fermi level equilibrates to a quasi-level altering overall energetics of reaction. In other words, photo-electrons tend to accumulate on the catalyst surface that comprises of Ag co-catalyst. On the other hand, Pt behaves like an ohmic contact[189] where photo-excited charges transferred rapidly from catalyst surface to an electrolyte. A schematic showing plausible electron-hole excitations and pathways are shown in figure 4.25.

Similar photoreduction experiments were conducted by replacing the glass window on top of photo-reactor with a quartz window. The quartz window transmitted

96

UVC to infrared light whereas, the transmission of glass window was restricted within UVA to visible region. The transmission spectra of glass and quartz windows used is given in figure 4.31. The FTIR spectra showing CO and CH_4 produced during these photoreduction experiments are shown in figures 4.26-4.29. Summary of photocatalytic performance based on total electronic yield and CH_4 selectivity during deep UV photo-irradiation is depicted in figure 4.30. In this case, we find that co-catalyst addition was not beneficial for improvement in yield. However, methane yield was slightly improved for P25 TiO_2 with added co-catalyst. This is similar to UVA photoirradiation results mentioned earlier where bimetallics showed a better performance than pure Ag or Pt for experiments with quartz window.

4.3 Summary

Ag, Pt, bimetallic Ag-Pt and Ag@SiO_2 core-shell nanoparticles were synthesized. Co-catalytic Ag, Pt and bimetallic nanoparticles helped in transfer of photo-excited electrons from photocatalyst nanocomposite to electron donating molecule such as CO_2. The role of Ag@SiO_2 core-shell nanoparticles was to induce plasmonic effect to increase the generation of electron-hole pairs. CH_4 selectivity was improved greatly when bimetallic Ag-Pt co-catalytic nanoparticles were used. We found there was a significant increase in catalytic activity when both co-catalytic and plasmonic nanoparticles were used in combination.

97
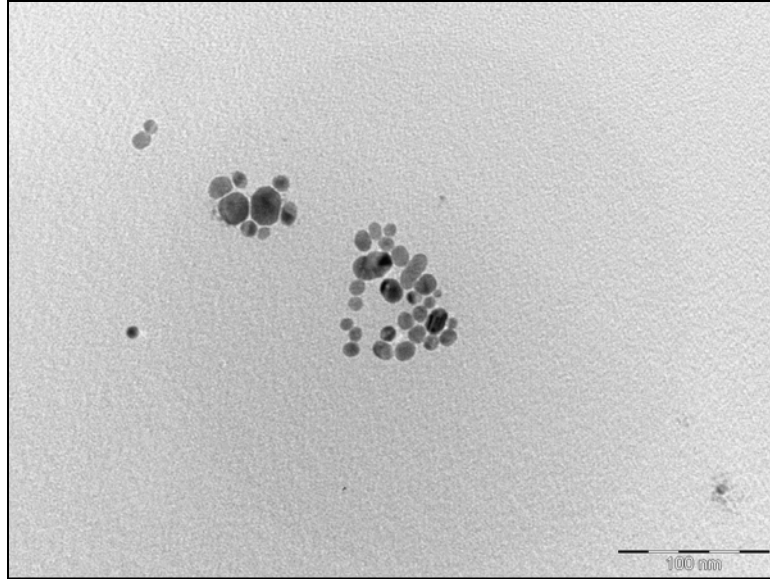
Figure 4.01. TEM of Ag nanoparticles
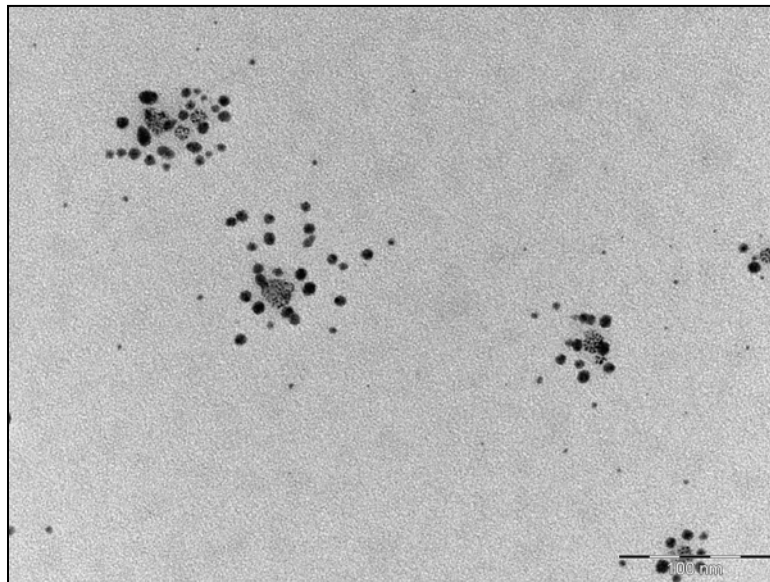
Figure 4.02. TEM of bimetallic Ag-Pt(10)
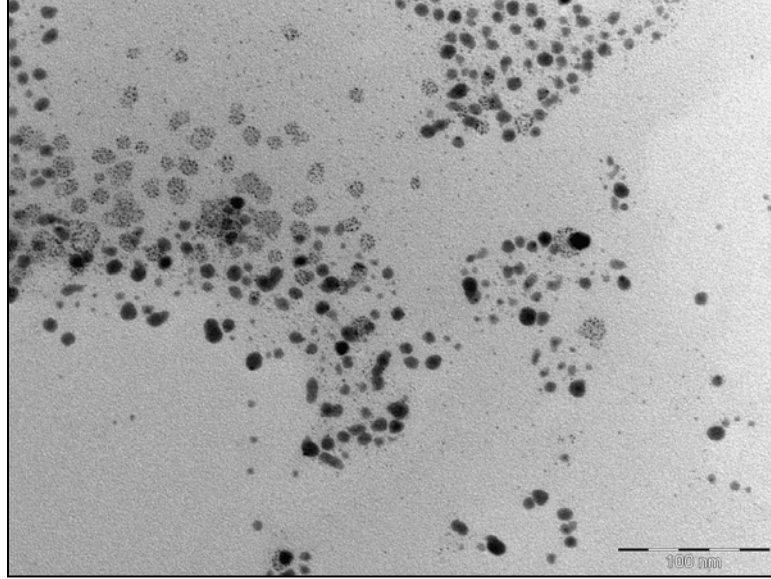
Figure 4.03. TEM of bimetallic Ag-Pt(20)
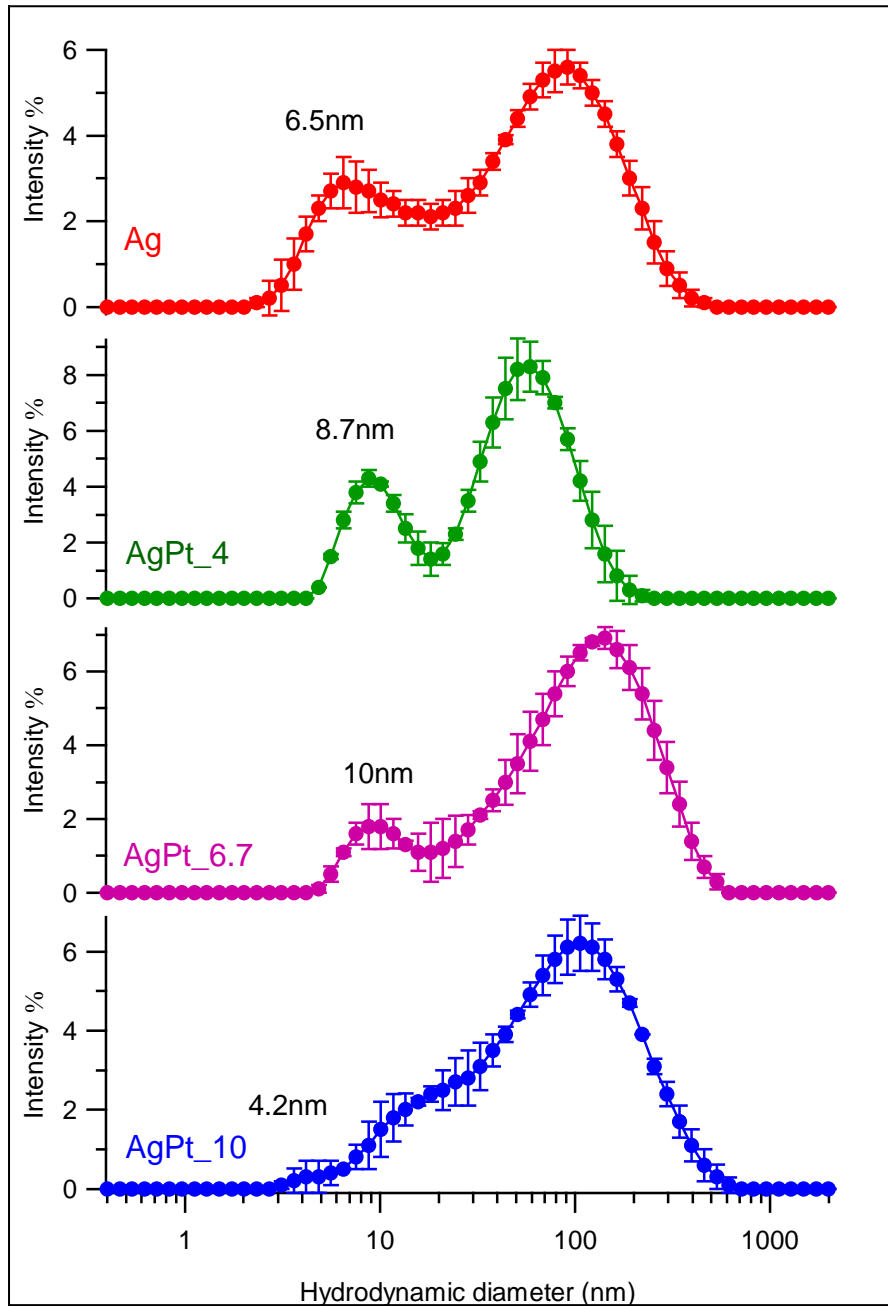
Figure 4.04. Size distribution of Ag and bimetallic Ag-Pt nanoparticles: intensity% obtained from DLS analysis
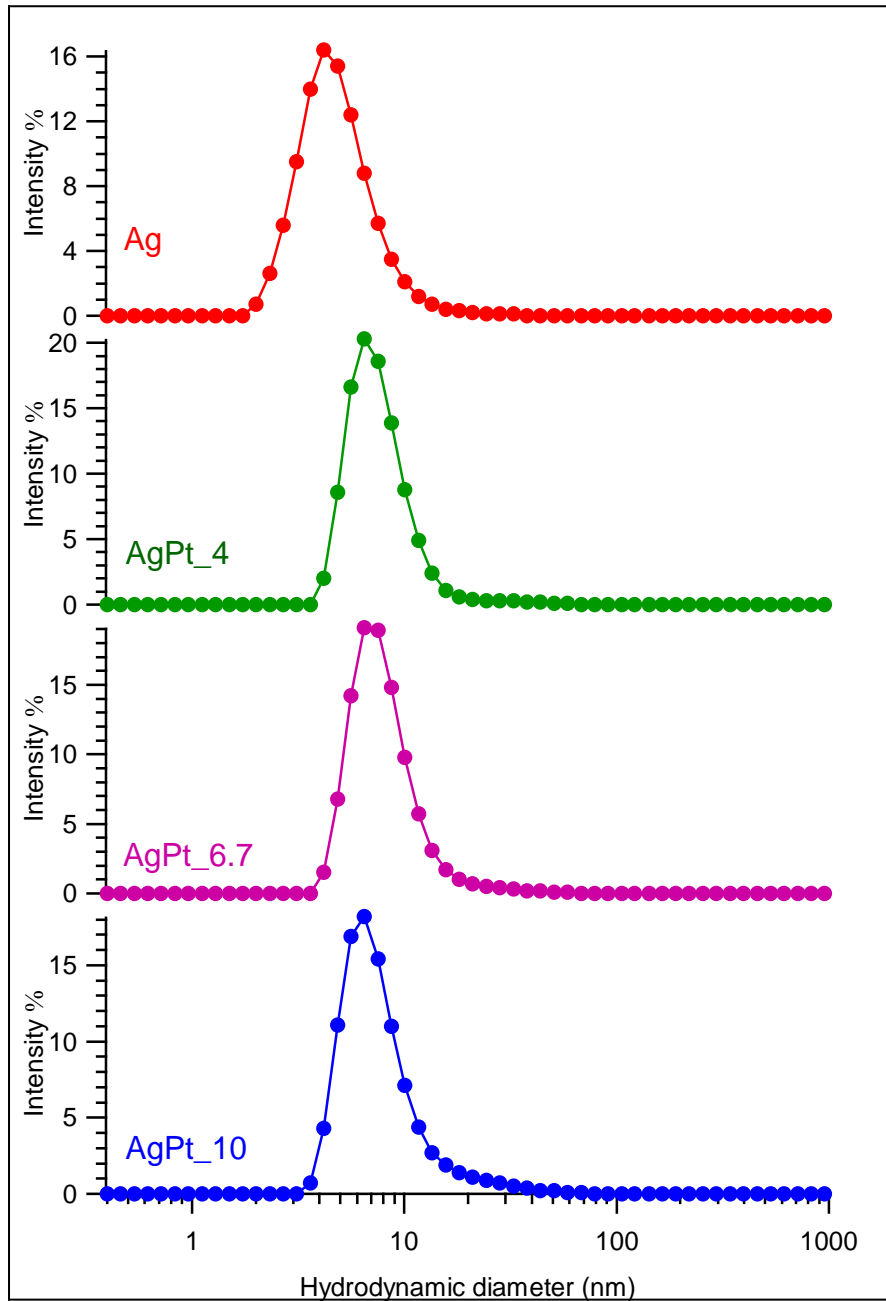
Figure 4.05. Size distribution of Ag and bimetallic Ag-Pt nanoparticles: volume% obtained from DLS analysis

101
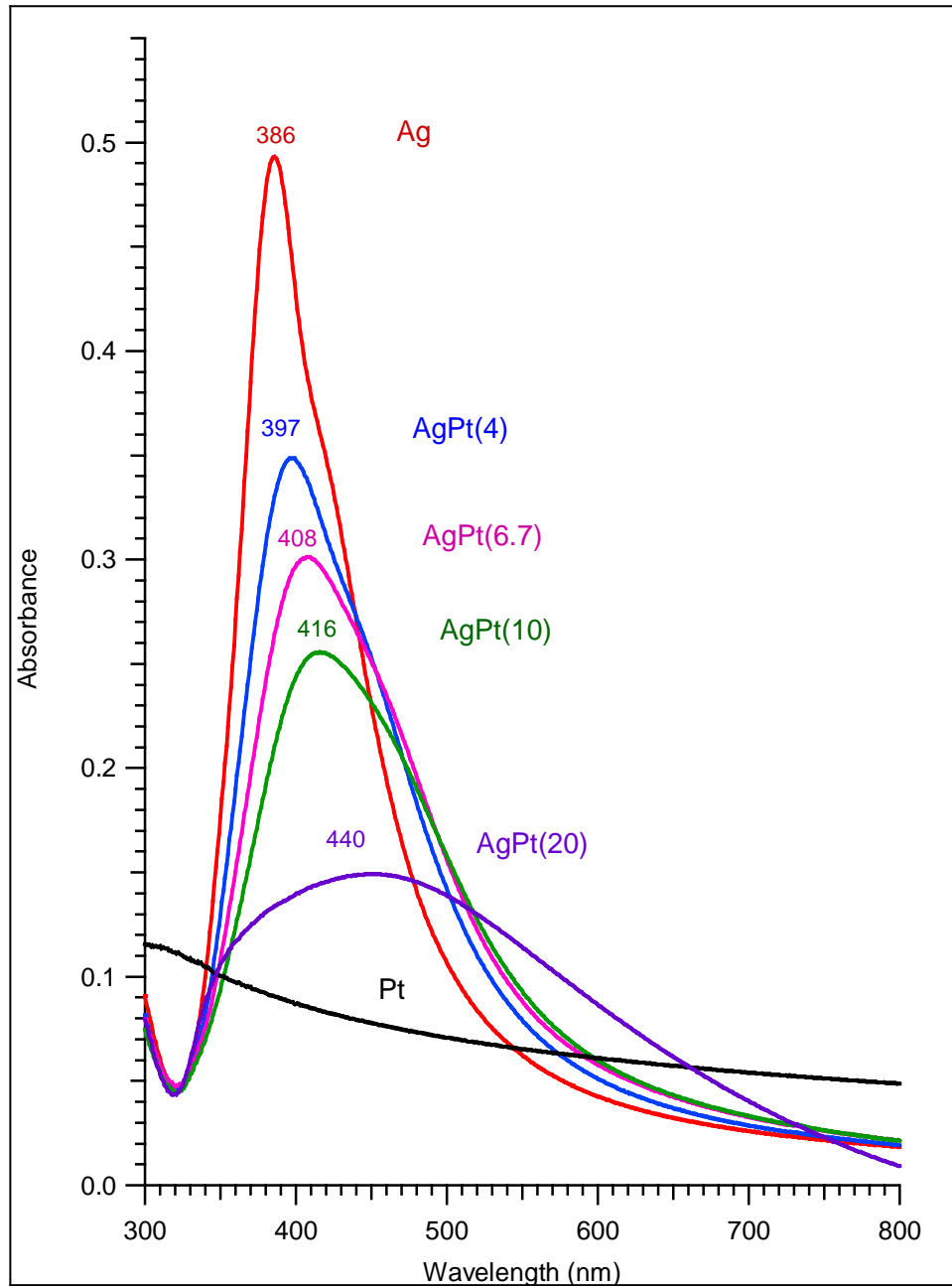
Figure 4.06. UV-Vis absorbance spectra of Ag, Pt and bimetallic Ag-Pt nanoparticles with different Pt concentrations
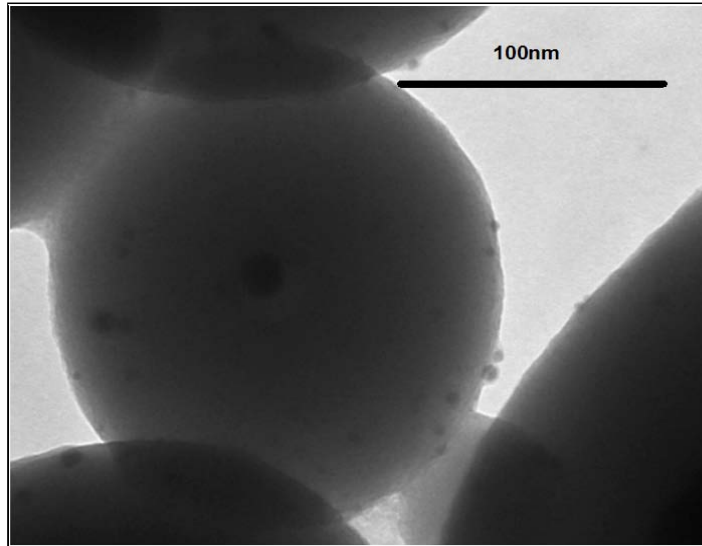
Figure 4.07. TEM of Ag&SiO$_2$ for Ag nanoparticle prepared using NaBH$_4$ reduction method
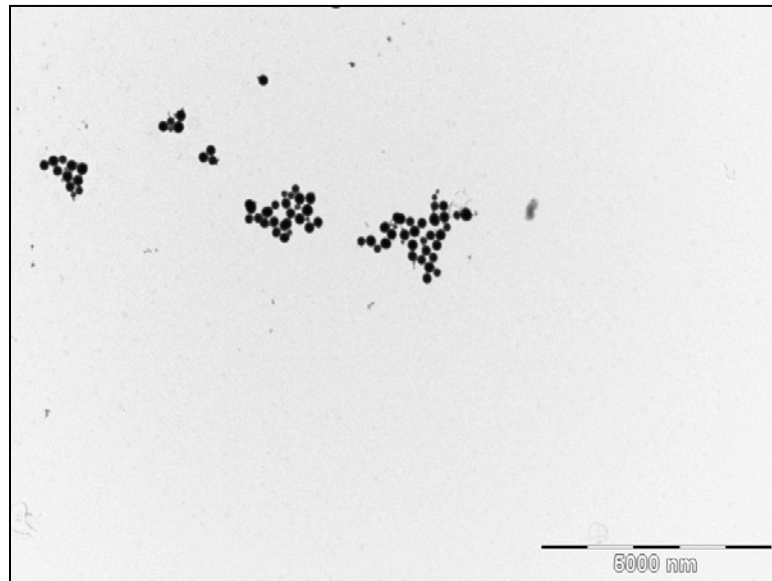
Figure 4.08. Low magnification TEM image of Ag&SiO$_2$ for Ag nanoparticle prepared using NaBH$_4$ reduction method

www.manaraa.com
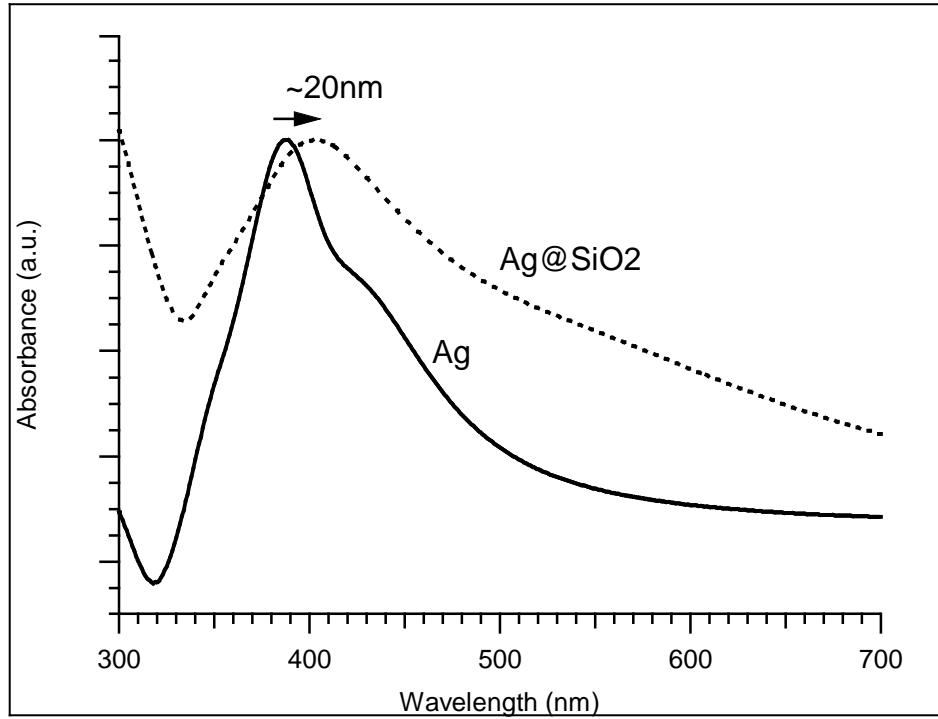
Figure 4.09. UV-Vis absorbance spectra of Ag@SiO$_2$ and Ag nanoparticles prepared using NaBH$_4$ reduction method.
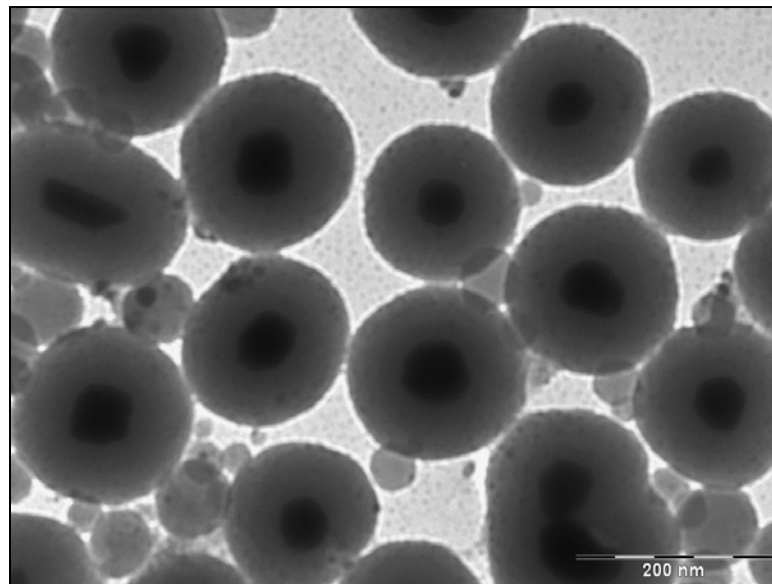
Figure 4.10. TEM image of Ag&SiO$_2$ using Ag nanoparticle prepared via Turkevich method

104
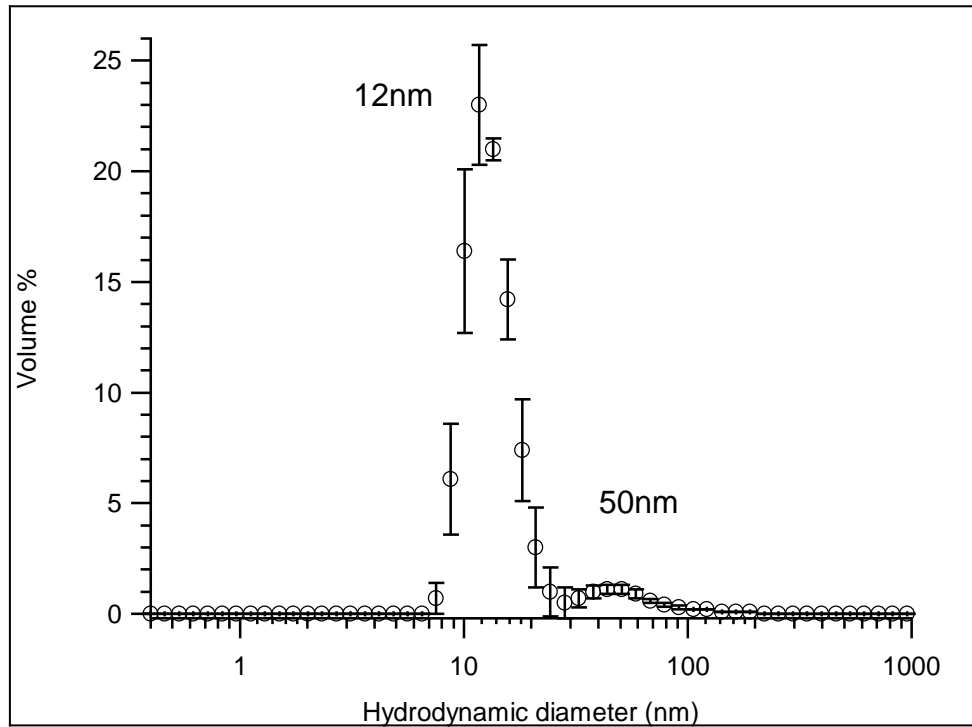
Figure 4.11. DLS of Ag nanoparticles synthesized via Turkevich method
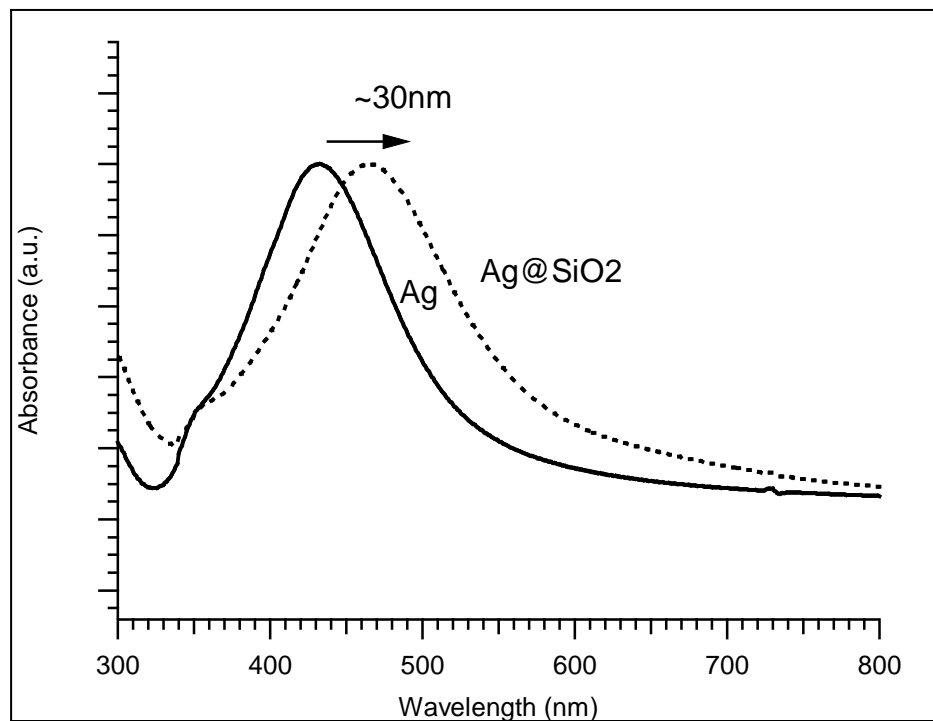
Figure 4.12. UV-Vis spectrum of Ag and Ag@SiO₂, where Ag was prepared using Turkevich method

105
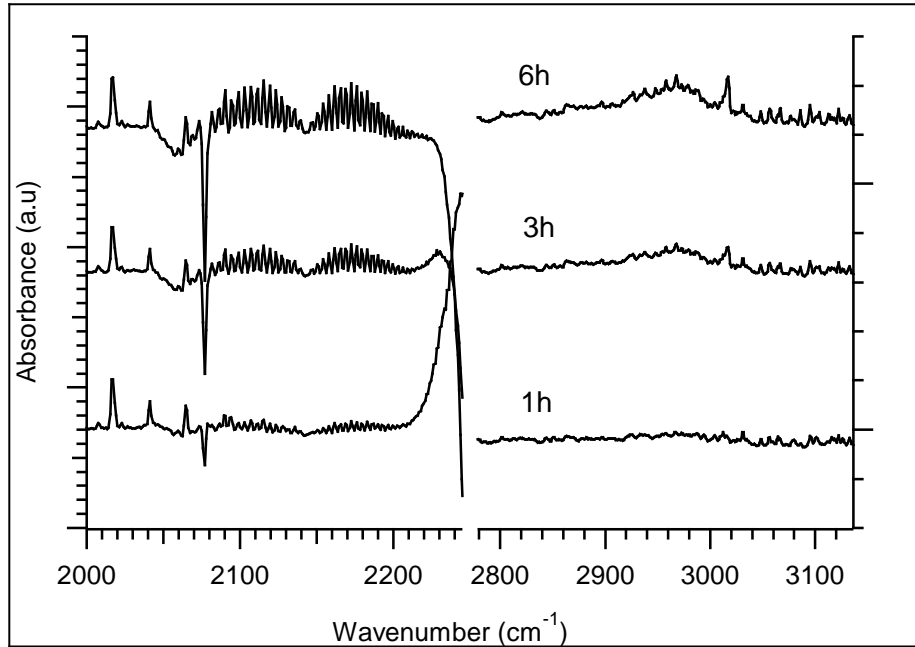
Figure 4.13. FTIR spectra of CO and CH$_4$ formation from native TiO$_2$ during photoreduction. A split x-axis is used for the wavenumber scale.
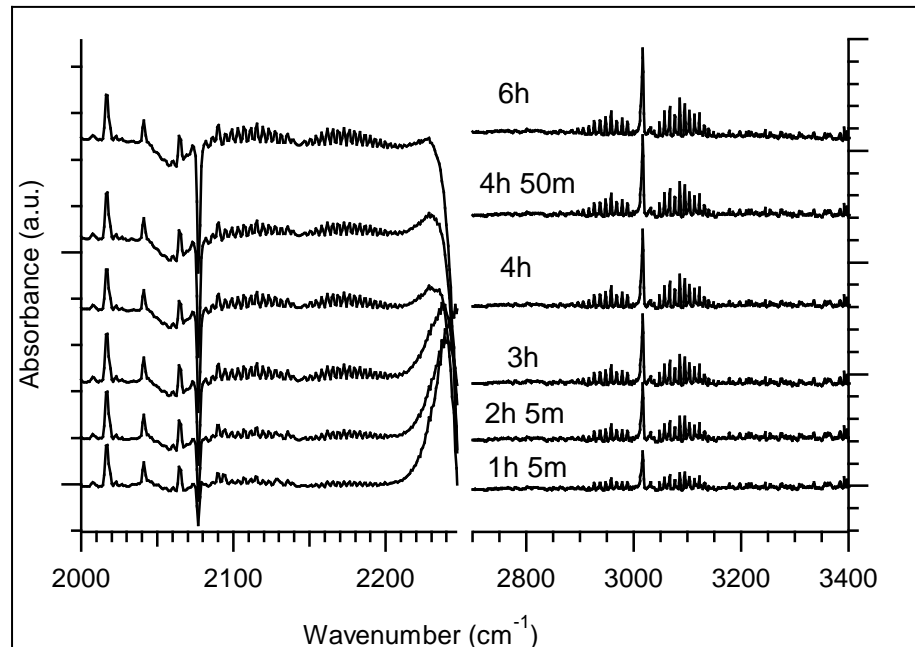
Figure 4.14. FTIR spectra of CO and CH$_4$ formation from Pt/TiO$_2$ during photoreduction. A split x-axis is used for the wavenumber scale.

106
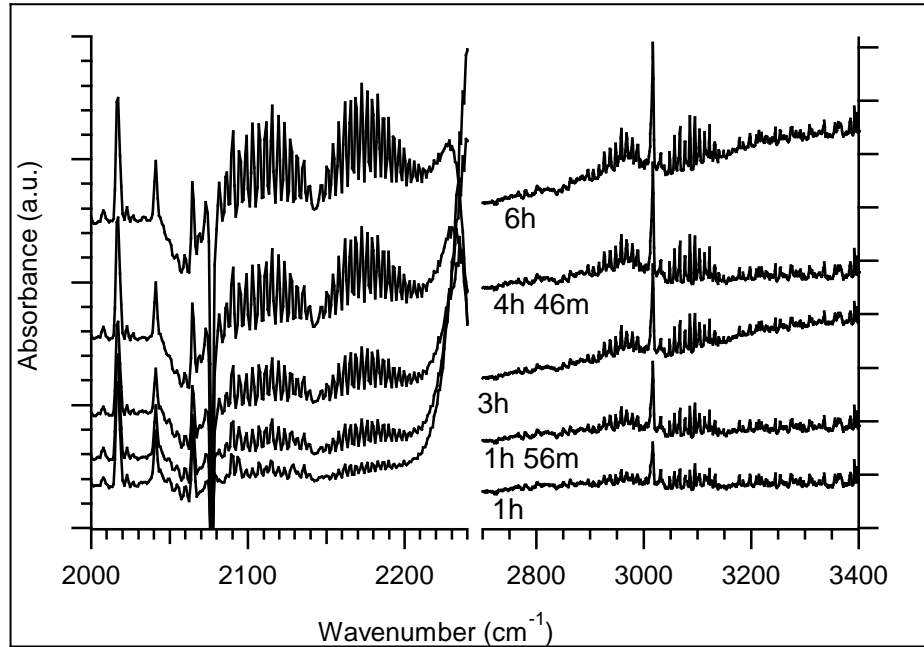
Figure 4.15. FTIR spectra of CO and CH$_4$ formation from Ag/TiO$_2$ during photoreduction. A split x-axis is used for the wavenumber scale.
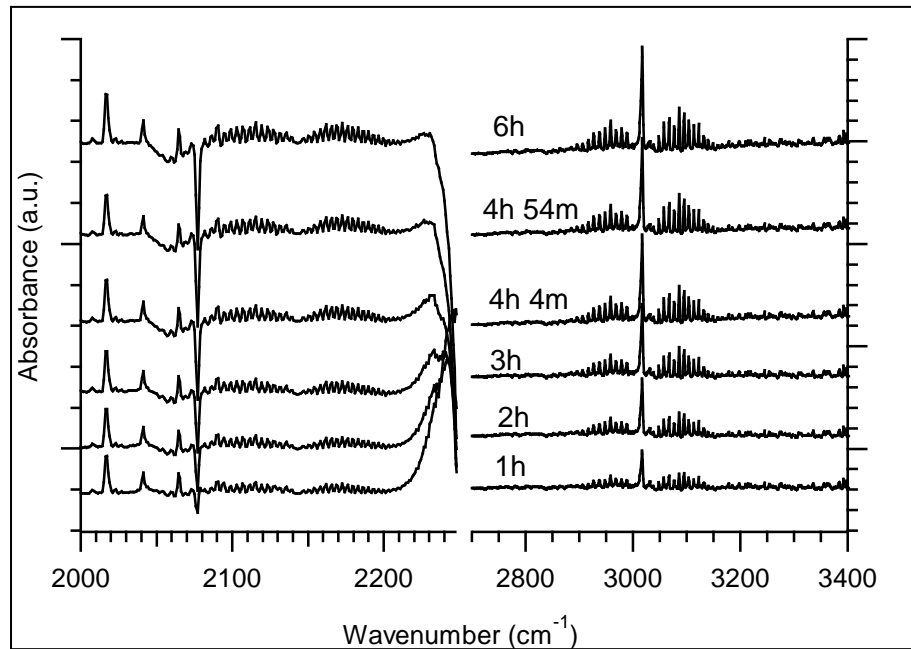
Figure 4.16. FTIR spectra of CO and CH$_4$ formation from Ag-Pt(4)/TiO$_2$ during photoreduction. A split x-axis is used for the wavenumber scale.
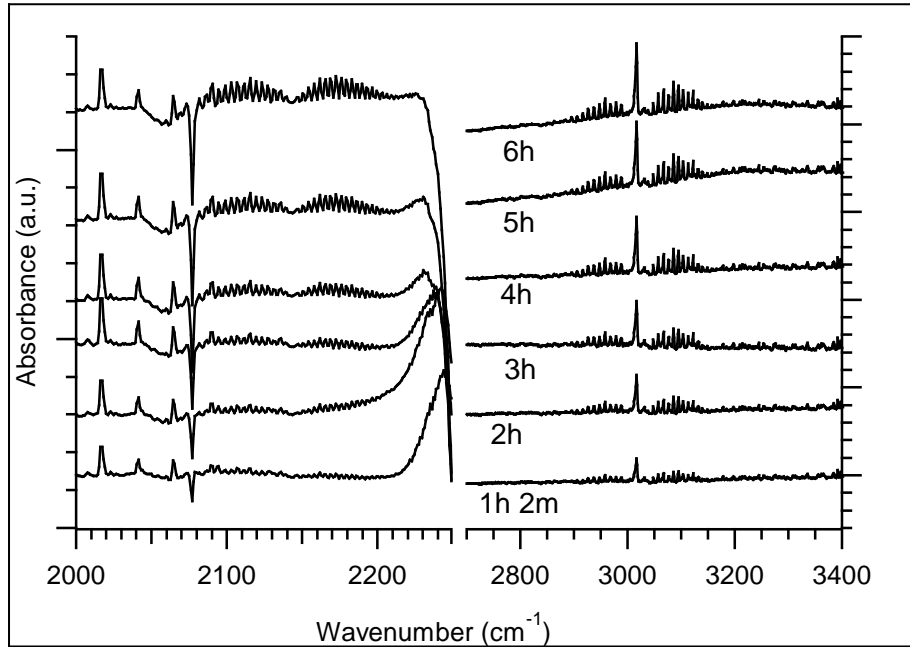
Figure 4.17. FTIR spectra of CO and CH$_4$ formation from Ag-Pt(6.7)/TiO$_2$ during photoreduction. A split x-axis is used for the wavenumber scale.
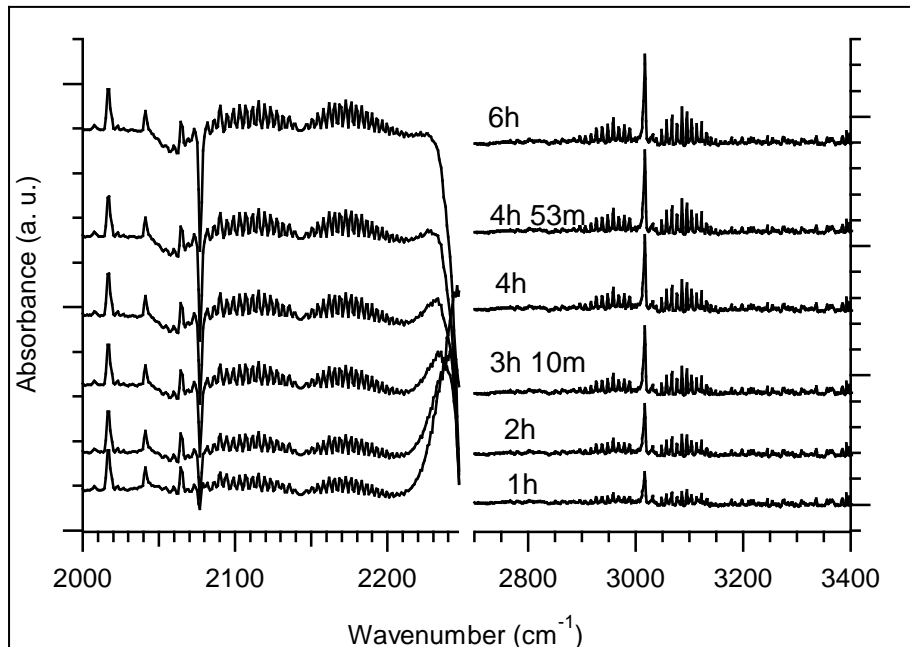
Figure 4.18. FTIR spectra of CO and CH$_4$ formation from Ag-Pt(10)/TiO$_2$ during photoreduction. A split x-axis is used for the wavenumber scale.

المنارة للاستشارات

www.manaraa.com
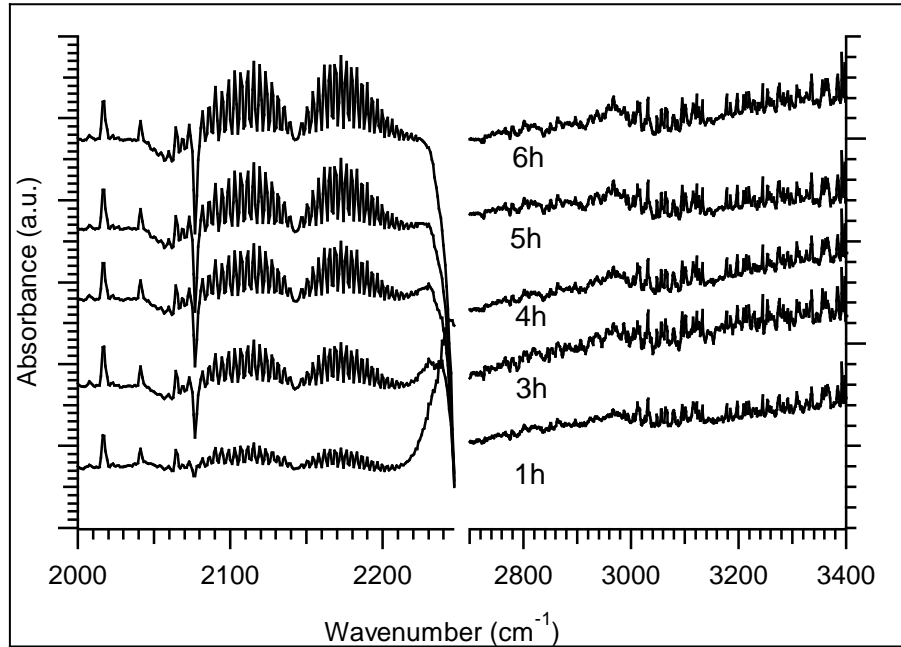
Figure 4.19. FTIR spectra of CO and CH$_4$ formation from Ag@SiO$_2$/TiO$_2$ during photoreduction. A split x-axis is used for the wavenumber scale.
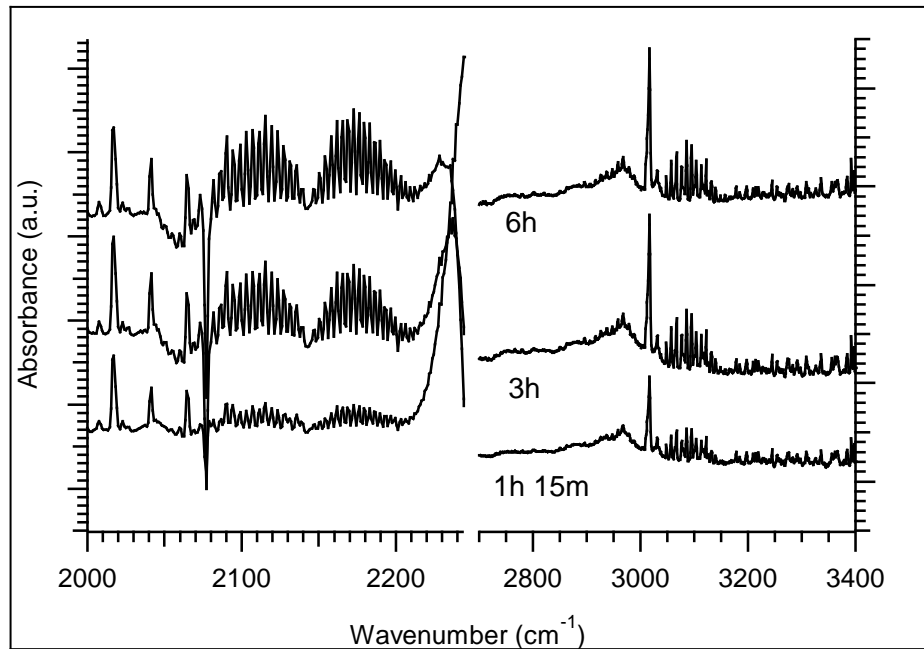
Figure 4.20. FTIR spectra of CO and CH$_4$ formation from Ag@SiO$_2$/Ag/TiO$_2$ during photoreduction. A split x-axis is used for the wavenumber scale.

109
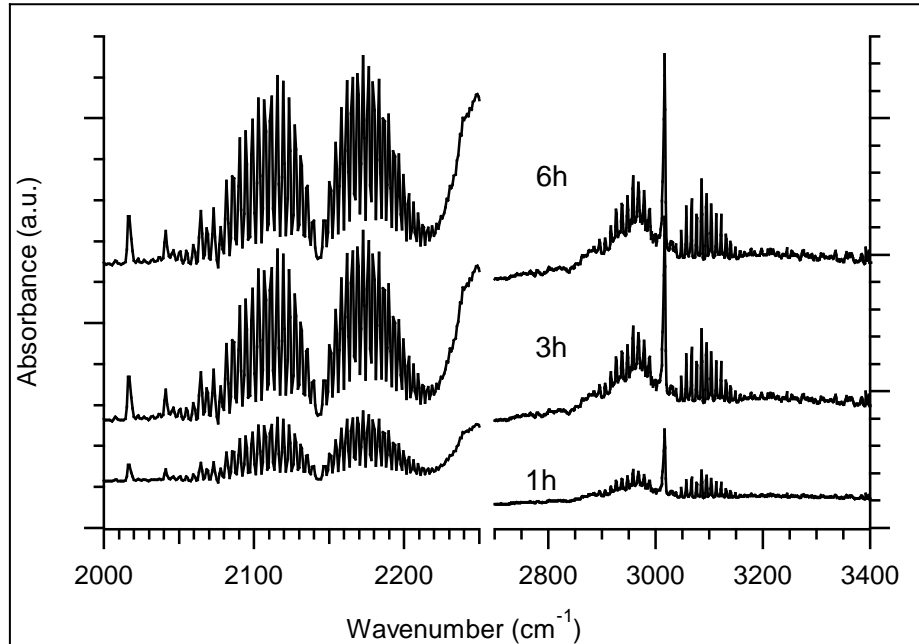
Figure 4.21. FTIR spectra of CO and CH₄ formation from Ag@SiO₂/Pt/TiO₂ during photoreduction. A split x-axis is used for the wavenumber scale.
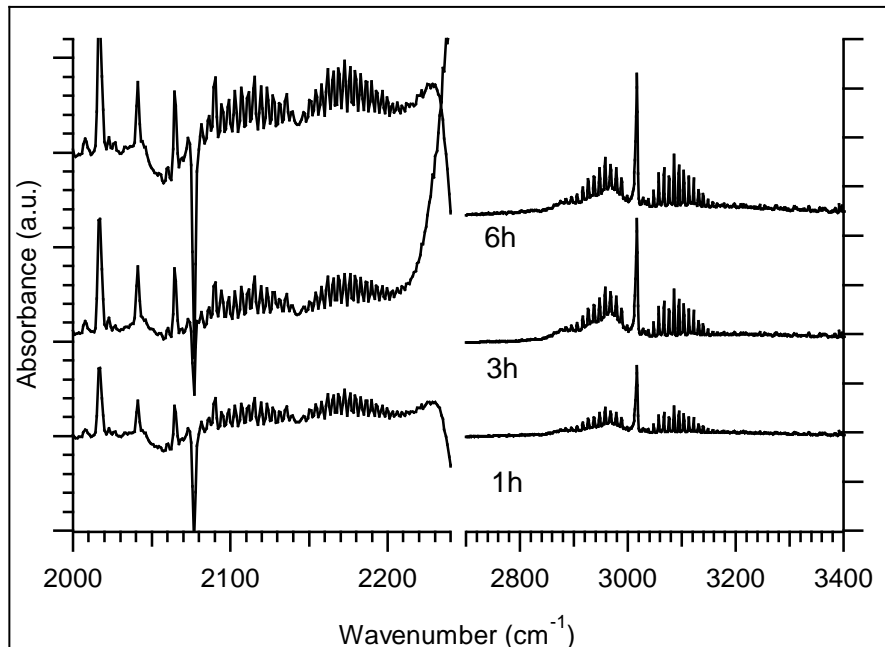
Figure 4.22. FTIR spectra of CO and CH₄ formation from Ag@SiO₂/Ag-Pt(6.7)/TiO₂ during photoreduction. A split x-axis is used for the wavenumber scale.

110
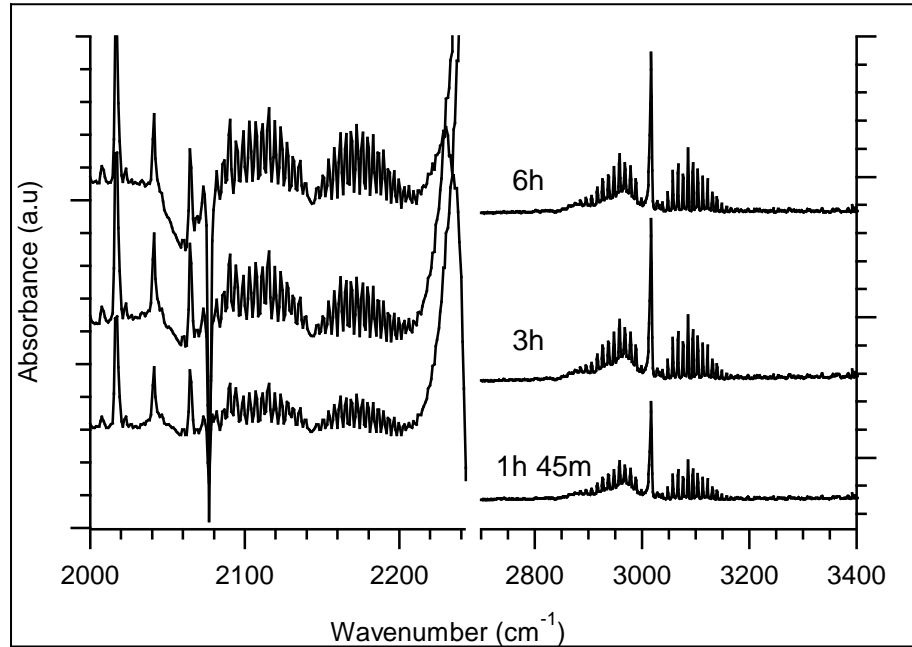
Figure 4.23. FTIR spectra of CO and CH$_4$ formation from Ag@SiO$_2$/Ag-Pt(10)/TiO$_2$ during photoreduction. A split x-axis is used for the wavenumber scale.
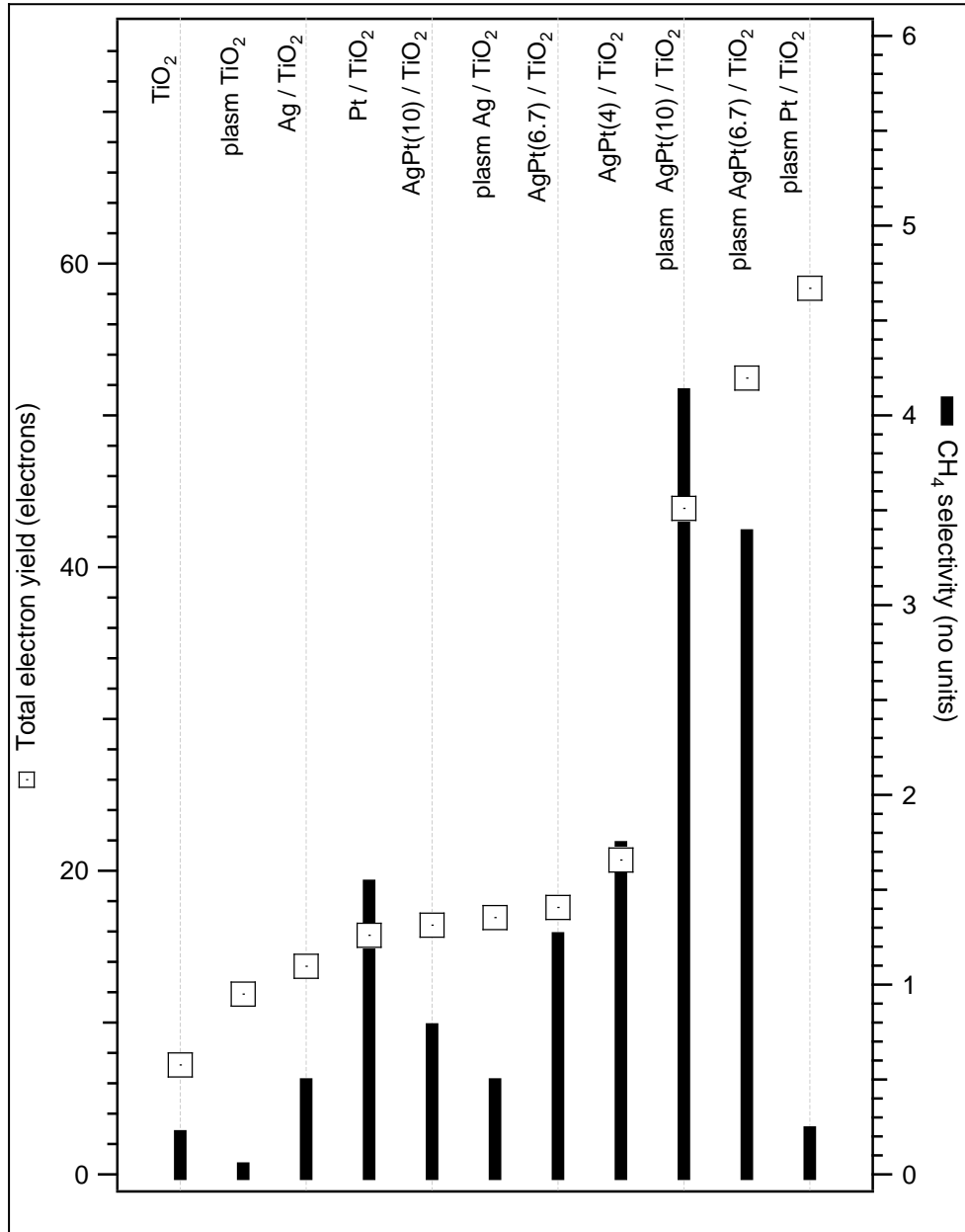
Figure 4.24. Performance of photocatalyst composites after 6 h of irradiation. The term plasm denotes the photocatalyst samples with plasmonic Ag@SiO$_2$ core-shell nanoparticles.

112
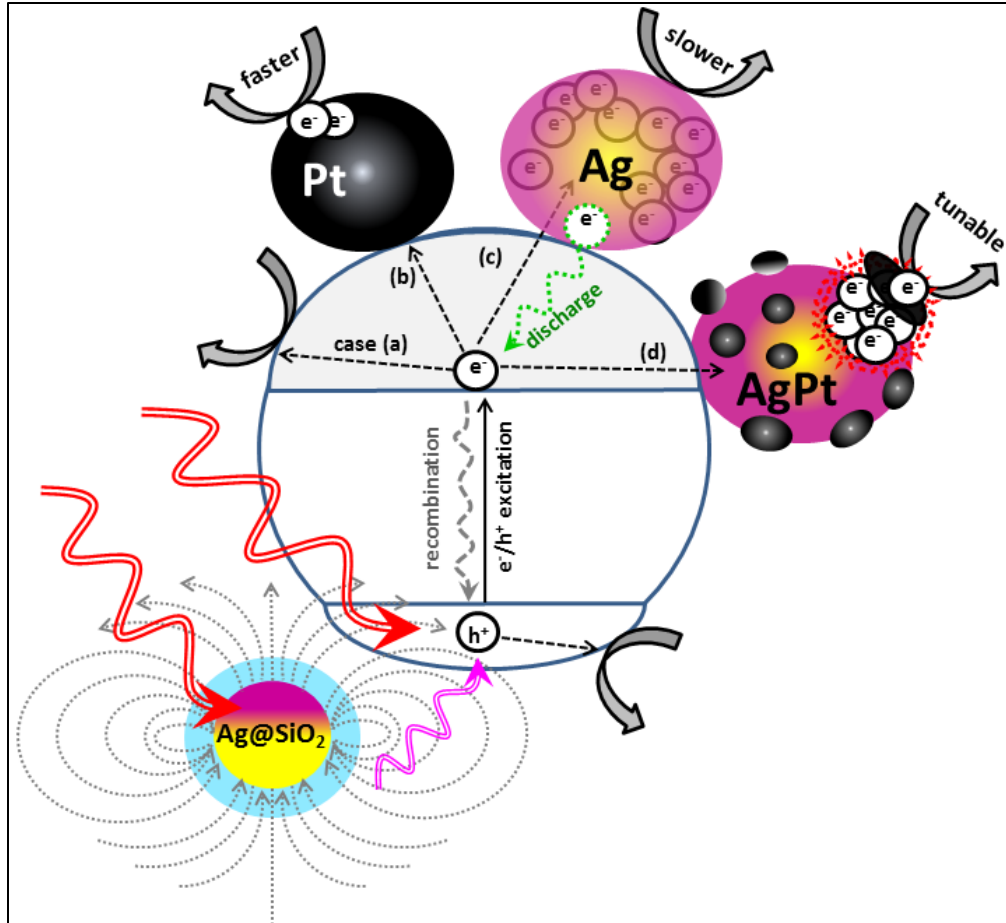
Figure 4.25. Different photo excited charge pathways subsequent to electron-hole generation assisted by plasmonic Ag@SiO$_2$ core-shell nanoparticles: case (a) to semiconductor surface, case (b) to Pt nanoparticle surface, case (c) to Ag nanoparticle surface, and case (d) to bimetallic Ag-Pt surface

113
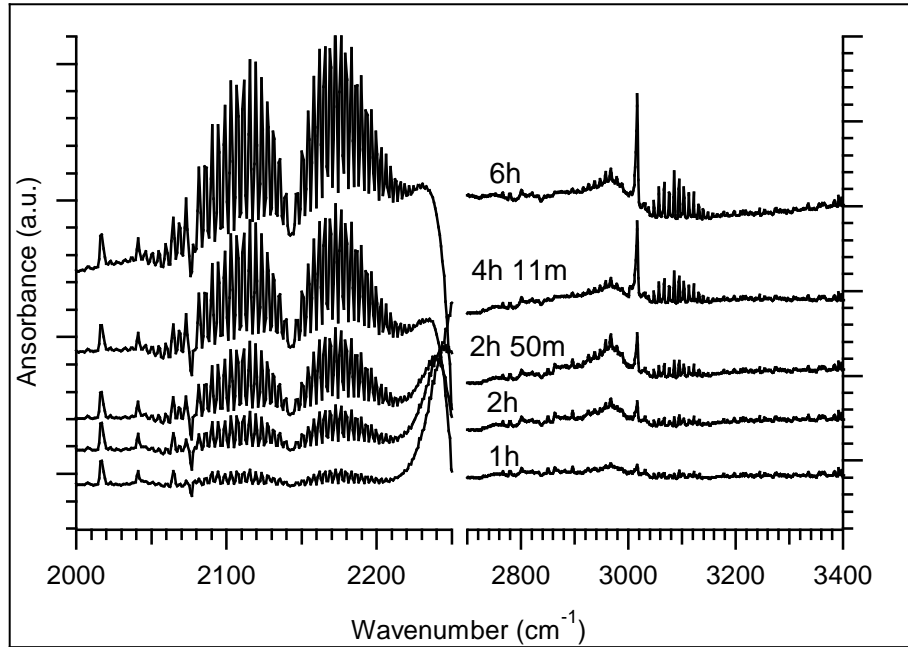
Figure 4.26. FTIR spectra of CO and CH_4 formation from native TiO_2 during photoreduction using quartz window. A split x-axis is used for the wavenumber scale.
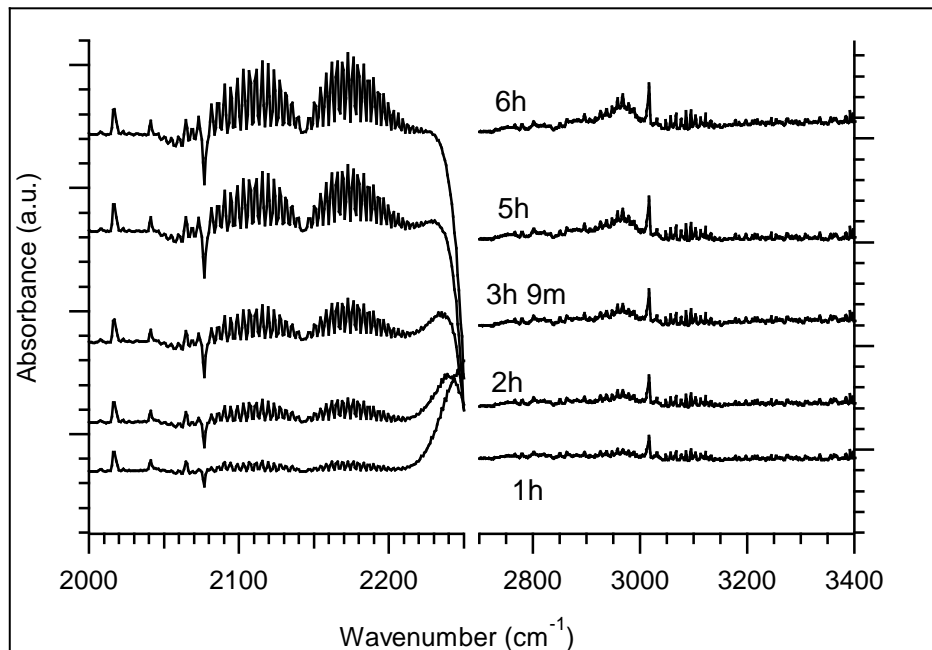
Figure 4.27. FTIR spectra of CO and CH_4 formation from Ag/TiO_2 during photoreduction using quartz window. A split x-axis is used for the wavenumber scale.

114
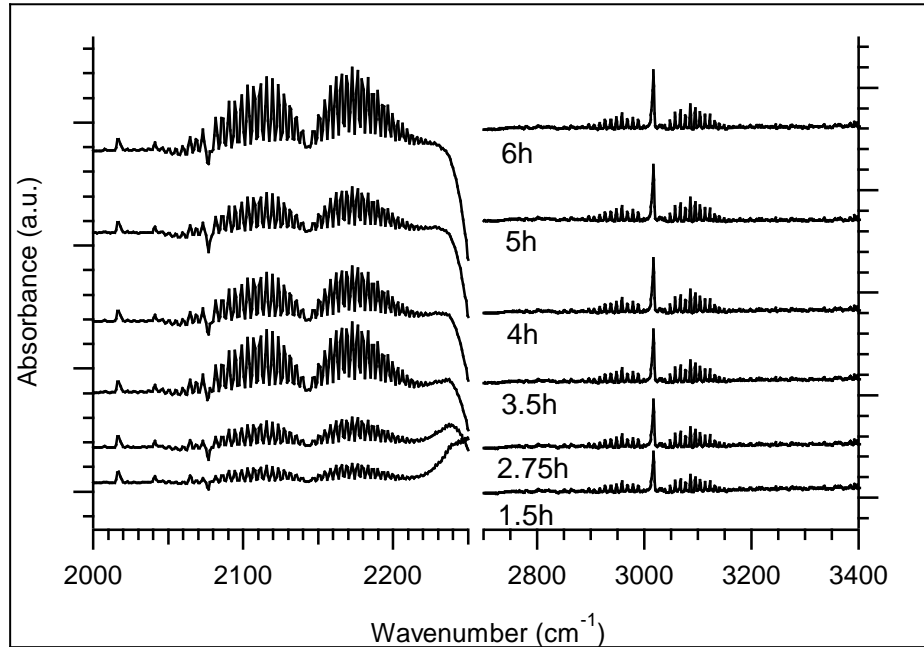
Figure 4.28. FTIR spectra of CO and CH$_4$ formation from Pt/TiO$_2$ during photoreduction using quartz window. A split x-axis is used for the wavenumber scale.
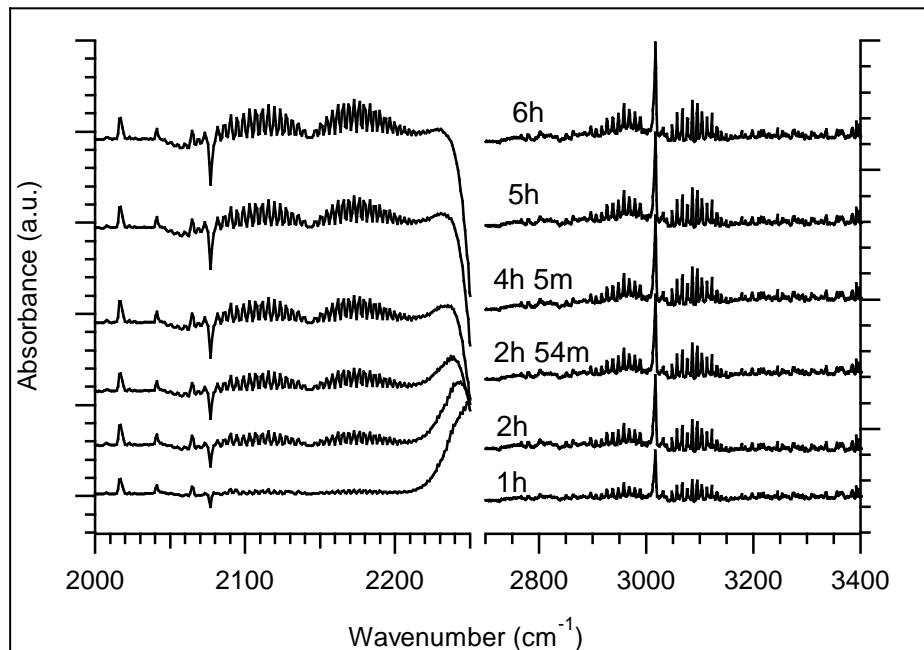
Figure 4.29. FTIR spectra of CO and CH$_4$ formation from Ag-Pt(4)/TiO$_2$ during photoreduction using quartz window. A split x-axis is used for the wavenumber scale.

115
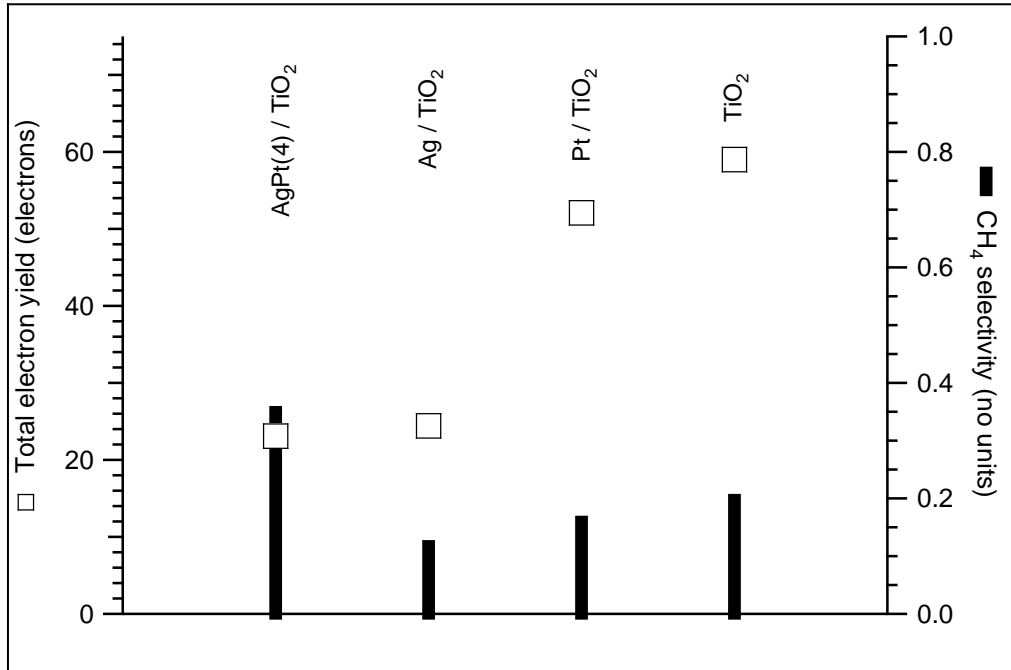
Figure 4.30. Performance of photocatalyst samples after 6 hours of irradiation using quartz window
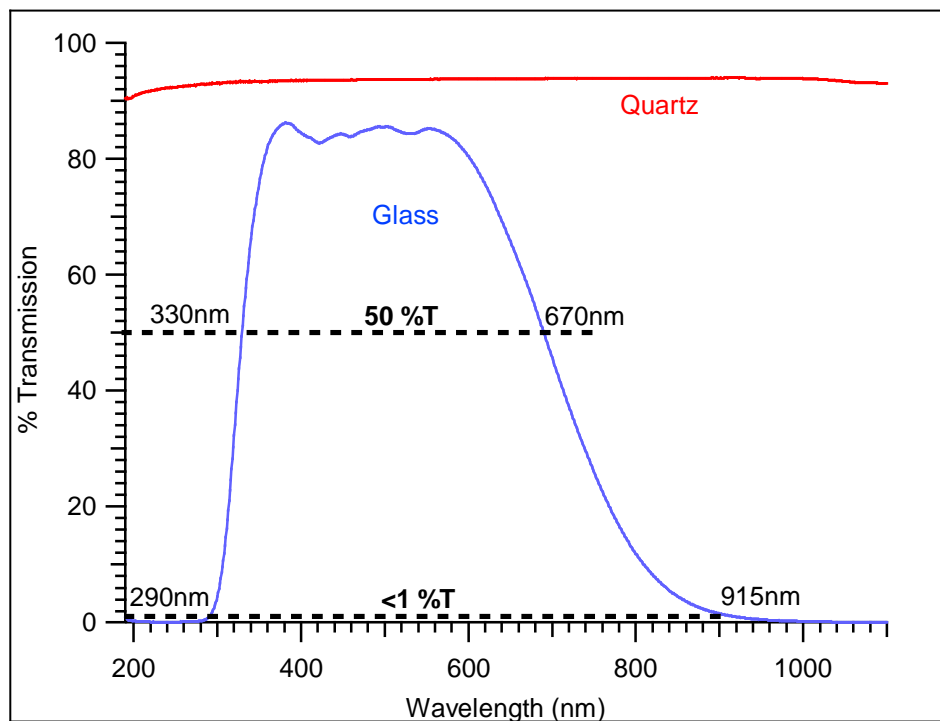
Figure 4.31. Transmission spectra of glass and quartz windows that were used during photoreduction experiments

116

CHAPTER 5: SUMMARY, CONCLUSIONS AND FUTURE WORK

5.1 Summary and conclusions

In this doctoral research, we have used novel colloidal routes to effectively control nanomaterial features and demonstrate how physical and chemical characteristics of nanomaterials can impact catalytic reactions, specifically the oxidation of CO and the photoreduction of CO_2. Using surfactant mediated synthesis we have carried out systematic variation of the catalytic nanoparticle size and studies its role. Novel nanoshell geometry has been used to explore the impact of surface area in photocatalysis. And finally, variations in elemental composition of co-catalytic nanoparticles in combination with core-shell plasmonic particles have been investigated for enhancing photoreduction reactions.

In chapter 2, the role of nanoparticle size of cobalt oxide for CO oxidation catalysis was investigated using advanced in-situ FTIR spectroscopy. We synthesized CoO catalyst particles with nanometer control over their average size. Nanoparticles ranging from 1 to 14nm were decorated on SiO_2 colloid supports via self-assembly approaches. By using this novel approach, we were able to directly estimate the impact of catalyst size on activation energy for CO oxidation reaction. To our knowledge, this is the first study of its kind. A major finding from the experiments was that a two-step mechanism for CO oxidation could be predicted. The activation energies obtained from the experimental studies were found to be a function of nanoparticle size. The two-step

117

mechanism predicted from experiments was validated using DFT calculations (PhD dissertation by Ms. Nianthrini Balakrishnan). This strategy of using colloidal techniques to prepare a model catalyst for investigation of size effect, the use of temperature programmed in-situ IR to probe kinetics, and to combine the experimental results with theoretical approaches can be a powerful tool to study catalytic reactions.

In chapter 3, we have demonstrated the synthesis of novel TiO_2 nanoshells with high surface area. Nanoshells of TiO_2 around colloidal SiO_2 were prepared by surface functionalization methods. Oligomeric chains of poly(NIPAAM) were carefully grafted on SiO_2 surface to initiate deposition of a TiO_2 precursor. This is the first time that nanoshells of TiO2 have been experimentally synthesized. The photocatalytic activity of the TiO_2 nanoshells was measured using a home-build reactor for CO_2 photoreduction reaction. We found that in the presence of water vapor, CO_2 can be successfully converted to synthetic hydrocarbon fuels such as CH_4 using the novel nanoshell structures which minimizes the use of bulk titania material. Further improvements in the CO_2 photoreduction yields were found by using a platinum co-catalyst on the TiO_2 nanoshell. We believe that the nanoshell structure can be optimized and can form the basis of improved photocatalytic yields.

Chapter 4 detailed results wherein colloidal nanoparticles of Ag, Pt and bimetallic nanoparticles of Ag-Pt with different Pt content were synthesized and their optical properties were measured using UV-Vis absorbance spectroscopy. These nanoparticles with different elemental compositions were deposited on a commercially available P25 TiO_2 to demonstrate the role of elemental composition of co-catalysts nanoparticles for CO_2 reduction photocatalysis. It was found that bimetallic Ag-Pt co-catalyst nanoparticles

118

showed improved photocatalytic yield and product selectivity. Core-shell nanoparticles with Ag core and SiO_2 shell that possess plasmonic character were prepared to enhance the catalytic activity of TiO_2 photocatalyst during CO_2 photoreduction reaction. The inner Ag core has plasmonic character that enhances the electromagnetic field near the TiO_2 surface. The SiO_2 shell serves as an insulating barrier for the photo-electrons from travelling from TiO_2 surface to the inner Ag core. The unique core-shell geometric structure of Ag@SiO_2 enhanced the photocatalytic activity by increasing the electron-hole pair generations with a TiO_2 semiconductor during photocatalysis.

Overall, this dissertation provides insights to novel colloidal preparation routes to synthesize nanomaterials of discrete sizes, high surface area, different elemental composition and specific core-shell geometric structures. In addition, this dissertation has demonstrated the correlation between the structure-property relationships of nanomaterials to two catalytic reactions: CO oxidation and CO_2 photoreduction.

5.2 Future work

We believe that the research pursued in this doctoral project lays the groundwork for other work in the field of nanomaterial synthesis. For example, the valuable insights gained from the preparation of CoO nanoparticles with precise control of size can be extended to synthesize CoO nanoparticles of different shapes. Wang and coworkers[52] have recently shown that a flat cobalt oxide surface when subjected to femtosecond lasers transforms its surface to spike like periodic features. It has been demonstrated that these periodic features have unique capability to produce synthetic hydrocarbons from CO_2 and water when irradiated directly under sunlight. This phenomenon is due to the enhancement in the photon absorption by nanostructured spike-like features. Cobalt

119

nanoparticles with shapes that impart them with a plasmonic character or similar photon absorptions as the spike-like surfaces may be used for CO_2 photoreduction reactions. The feasibility of this hypothesis is supported by our preliminary work that shows that nano-triangles of cobalt oxide possess a plasmonic band in the visible region. The TEM and UV-Vis absorbance spectra of cobalt oxide nano-triangles from this preliminary work are shown in figures 5.1 and 5.2. The colloidal approaches for spherical nanoparticle preparation mentioned in chapter 2 were extremely useful in the synthesis of the cobalt nano-triangles[136]. It is clear that colloidal approaches can be a viable alternative method to produce nanoparticles in large scales when compared to more energy intensive methods such as femtosecond laser etching methods.

Techniques developed for TiO_2 nanoshell creation can be expanded to fabricate new material composites containing TiO_2 coatings with high surface area. These coatings can be used to not only enhance the material properties but also to diversify the applications of the resulting composites. For instance, ZnO, a metal oxide has been used in nanoelectronics, sensors, light-emitting diodes, photocatalysis, and nanopiezotronics due to its unique semiconducting, piezoelectric, and pyroelectric properties[197, 198]. ZnO has shown stability under low humidity environment[199]; however, it undergoes photolysis in the presence of moisture under strong UV irradiation[200, 201]. By coating TiO_2 on ZnO, this synergistic combination improves the stability of ZnO since TiO_2 has higher oxidizing power than ZnO [39, 202, 203]. Irannejad and coworkers have observed that there was an improvement in photocatalytic activity of ZnO rods were coated with TiO_2 compared to uncoated ZnO rods[177]. Park and coworkers have demonstrated the benefit of coating photoelectrodes made of ZnO with TiO_2 for achieving higher power conversion efficiency[204]. TiO_2 deposited on RuO_2 via

120

reactive sputtering method[205] shows an improvement in the mechanical, optical, electrical, and photoconductive properties compared to native RuO_2, a metal oxide used as interconnects in electronic devices such as resistors[206, 207]. Thin coatings of TiO_2 are an ideal choice to complement the transparent and conducting properties of Ga_2O_3, a material used in optoelectronic devices for flat panel displays, solar energy conversion devices and optical limiters for UV and thermostable sensors[185, 208]. Chang and coworkers[209] have demonstrated CVD methods to effectively deposit TiO_2 on Ga_2O_3. Zhang and coworkers[210] have shown the preparation of TiO_2 nanocable arrays on Si substrates by using a vapor phase deposition method. Macák and coworkers have synthesized highly porous TiO_2 nanotubes with high aspect ratios by tailoring the conditions during electrochemical anodization of titanium[42]. Chu and coworkers also applied electrochemical anodization techniques to synthesize a three-dimensional highly porous TiO_2-SiO_2-TeO_2-Al_2O_3 photocatalyst composite[46]. Grimes' research group have synthesized self-aligned highly ordered TiO_2 nanotube arrays by anodization methods and used as a photocatalyst for reduction of CO_2 to synthetic hydrocarbons[48, 50]. Yang and coworkers[211] have demonstrated the preparation of thin-film photoelectrodes containing hollow TiO_2 hemispheres via a combination of colloidal templating and RF-sputtering methods. However, most of these methods involve vapor deposition, layer-by-layer coating, or electrochemical deposition and these approaches have limited scalability as they are expensive and time consuming due to the multiple assembly steps involved in the preparation steps to obtain TiO_2 of sufficient thickness[212-220]. In comparison, the use of polymer templating to create nanoshells of TiO_2 is simpler and more versatile.

121

The syntheses procedures developed for bimetallic nanoparticles and core-shell plasmonic nanoparticles can be used in combination with polymer templating method to create multi-functional surfaces with high surface area and porosity. For instance, by using a mixture containing an appropriate polymer template, titania, bimetallic co-catalysts and plasmonic nanoparticles, the preparation of high surface area panels or electrodes using colloidal approaches may become possible as shown schematically in figure 5.3. By coating the flat surface by dip coating and further heat or UV treatment, porous photocatalyst films can be prepared with embedded nanoparticles. The embedded co-catalyst nanoparticles serve as electron-hole transferring sites and plasmonic nanoparticles serve as electron-hole boosting sites. These films can be used for direct photoreactions of CO_2 reduction, water splitting and degradation reactions, or as photoelectrodes. These novel preparation techniques can be beneficial for photocatalytic and photovoltaic industries to manufacture multifunctional films via inexpensive routes.
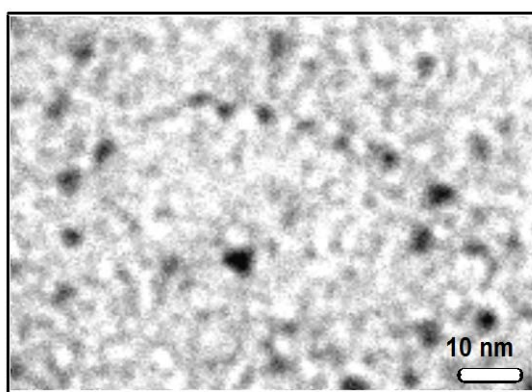
Figure 5.01. TEM image of cobalt oxide nano-triangle
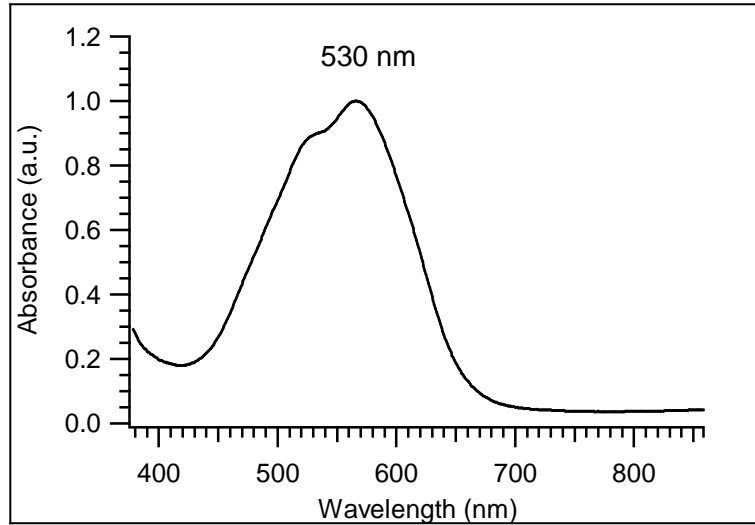
Figure 5.02. UV-Vis absorbance spectrum of cobalt oxide nano-triangles in o-dichlorobenzene
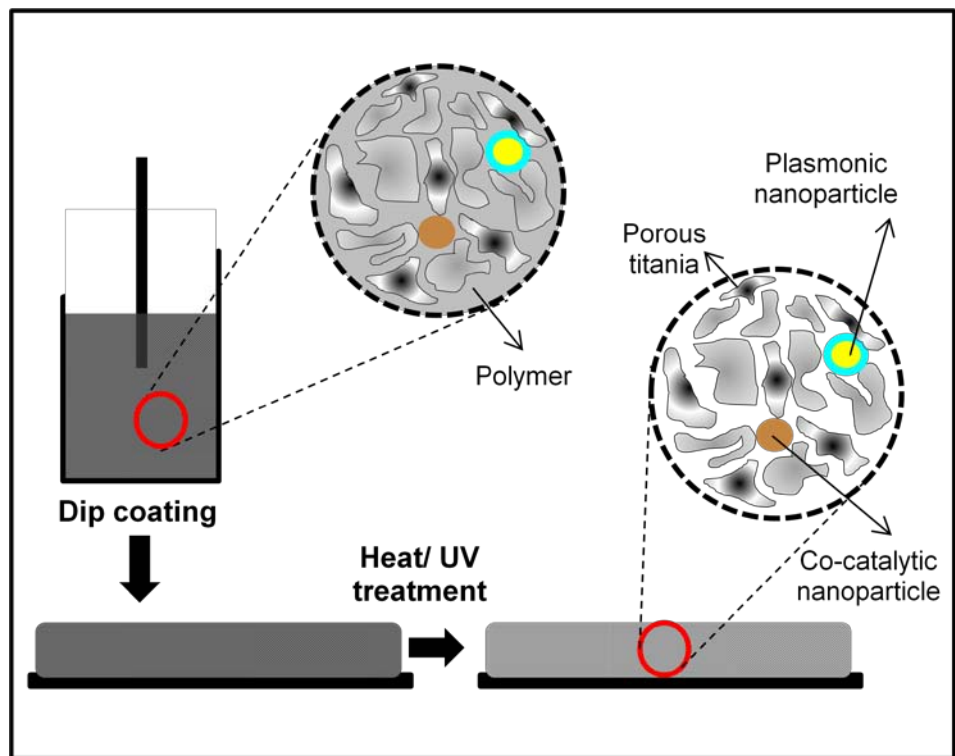
Figure 5.03. Schematic of preparation of porous high surface area multifunctional titania film

REFERENCES

1. Deng, W., et al., *Reaction-Relevant Gold Structures in the Low Temperature Water-Gas Shift Reaction on Au-CeO$_2$.* The Journal of Physical Chemistry C, 2008. 112(33): p. 12834-12840.

2. Aguilar-Guerrero, V. and B. Gates, *Kinetics of CO Oxidation Catalyzed by Supported Gold: A Tabular Summary of the Literature.* Catalysis Letters, 2009. 130(1): p. 108-120.

3. Sanchez, A., et al., *When Gold Is Not Noble:Nanoscale Gold Catalysts.* The Journal of Physical Chemistry A, 1999. 103(48): p. 9573-9578.

4. Pastoriza-Santos, I. and L.M. Liz-Marzán, *Synthesis of Silver Nanoprisms in DMF.* Nano Letters, 2002. 2(8): p. 903-905.

5. Chen, J., et al., *Facile Synthesis of Gold-Silver Nanocages with Controllable Pores on the Surface.* Journal of the American Chemical Society, 2006. 128(46): p. 14776-14777.

6. Murphy, C.J., *Nanocubes and Nanoboxes.* Science, 2002. 298(5601): p. 2139-2141.

7. Scott, R.W.J., et al., *Titania-Supported PdAu Bimetallic Catalysts Prepared from Dendrimer-Encapsulated Nanoparticle Precursors.* Journal of the American Chemical Society, 2005. 127(5): p. 1380-1381.

8. Mott, D., et al., *Synergistic activity of gold-platinum alloy nanoparticle catalysts.* Catalysis Today, 2007. 122(3–4): p. 378-385.

9. Liz-Marzán, L.M., M. Giersig, and P. Mulvaney, *Synthesis of Nanosized Gold−Silica Core−Shell Particles.* Langmuir, 1996. 12(18): p. 4329-4335.

10. Jana, N.R., L. Gearheart, and C.J. Murphy, *Seeding Growth for Size Control of 5−40 nm Diameter Gold Nanoparticles.* Langmuir, 2001. 17(22): p. 6782-6786.

11. Lu, Y., et al., *Synthesis and Self-Assembly of Au@SiO2 Core−Shell Colloids.* Nano Letters, 2002. 2(7): p. 785-788.

12. Loo, C., et al., *Nanoshell-Enabled Photonics-Based Imaging and Therapy of Cancer.* Technology in Cancer Research & Treatment, 2004. 3(1): p. 33-40.

13. Yong, K.-T., et al., *Synthesis and plasmonic properties of silver and gold nanoshells on polystyrene cores of different size and of gold–silver core–shell nanostructures.* Colloids and Surfaces A: Physicochemical and Engineering Aspects, 2006. 290(1–3): p. 89-105.

14. Ji, X., et al., *Bifunctional Gold Nanoshells with a Superparamagnetic Iron Oxide−Silica Core Suitable for Both MR Imaging and Photothermal Therapy.* The Journal of Physical Chemistry C, 2007. 111(17): p. 6245-6251.

15. Zhang, J.Z., *Biomedical Applications of Shape-Controlled Plasmonic Nanostructures: A Case Study of Hollow Gold Nanospheres for Photothermal Ablation Therapy of Cancer.* The Journal of Physical Chemistry Letters, 2010. 1(4): p. 686-695.

16. Zhou, B., R. Balee, and R. Groenendaal, *Nanoparticle and nanostructure catalysts: Technologies and markets.* Nanotechnology law and buisiness, 2005. 2(3): p. 222-229.

17. Dahl, S., et al., *Role of Steps in N_2 Activation on Ru(0001).* Physical Review Letters, 1999. 83(9): p. 1814-1817.

18. Haruta, M., et al., *Low-Temperature Oxidation of CO over Gold Supported on TiO_2, α-Fe_2O_3, and Co_3O_4.* Journal of Catalysis, 1993. 144(1): p. 175-192.

19. Haruta, M., *When Gold Is Not Noble: Catalysis by Nanoparticles.* The Chemical Record, 2003. 3(2): p. 75-87.

20. McCarthy, E., et al., *Some unique aspects of CO oxidation on supported Pt.* Journal of Catalysis, 1975. 39(1): p. 29-35.

21. Shaikhutdinov, S.K., et al., *Size and Support Effects for CO Adsorption on Gold Model Catalysts.* Catalysis Letters, 2003. 86(4): p. 211-219.

22. Lu, H.M. and X.K. Meng, *Theoretical Model to Calculate Catalytic Activation Energies of Platinum Nanoparticles of Different Sizes and Shapes.* The Journal of Physical Chemistry C, 2009. 114(3): p. 1534-1538.

23. Overbury, S.H., et al., *Evaluation of the Au size effect: CO oxidation catalyzed by Au/TiO2.* Journal of Catalysis, 2006. 241(1): p. 56-65.

24. Valden, M., X. Lai, and D.W. Goodman, *Onset of Catalytic Activity of Gold Clusters on Titania with the Appearance of Nonmetallic Properties.* Science, 1998. 281(5383): p. 1647-1650.

25. Grass, M.E., et al., *A Reactive Oxide Overlayer on Rhodium Nanoparticles during CO Oxidation and Its Size Dependence Studied by In Situ Ambient-Pressure X-ray Photoelectron Spectroscopy.* Angewandte Chemie International Edition, 2008. 47(46): p. 8893-8896.

26. Joo, S.H., et al., *Size Effect of Ruthenium Nanoparticles in Catalytic Carbon Monoxide Oxidation.* Nano Letters, 2010. 10(7): p. 2709-2713.

125

27. Boudart, M. and F. Rumpf, *The catalytic oxidation of CO and structure insensitivity.* Reaction Kinetics and Catalysis Letters, 1987. 35(1): p. 95-105.

28. Falsig, H., et al., *Trends in the Catalytic CO Oxidation Activity of Nanoparticles.* Angewandte Chemie International Edition, 2008. 47(26): p. 4835-4839.

29. Norskov, J.K., et al., *Towards the computational design of solid catalysts.* Nat Chem, 2009. 1(1): p. 37-46.

30. Ledoux, M.J. and C. Pham-Huu, *High specific surface area carbides of silicon and transition metals for catalysis.* Catalysis Today, 1992. 15(2): p. 263-284.

31. Zhao, D., et al., *Morphological Control of Highly Ordered Mesoporous Silica SBA-15.* Chemistry of Materials, 2000. 12(2): p. 275-279.

32. Terribile, D., et al., *The Synthesis and Characterization of Mesoporous High-Surface Area Ceria Prepared Using a Hybrid Organic/Inorganic Route.* Journal of Catalysis, 1998. 178(1): p. 299-308.

33. Chuah, G.K., S. Jaenicke, and T.H. Xu, *Acidity of high-surface-area zirconia prepared from different precipitants.* Surface and Interface Analysis, 1999. 28(1): p. 131-134.

34. Ohno, T., et al., *Morphology of a TiO2 Photocatalyst (Degussa, P-25) Consisting of Anatase and Rutile Crystalline Phases.* Journal of Catalysis, 2001. 203(1): p. 82-86.

35. Herrmann, J.M., et al., *Characterization and photocatalytic activity in aqueous medium of TiO_2 and $Ag-TiO_2$ coatings on quartz.* Applied Catalysis B: Environmental, 1997. 13(3–4): p. 219-228.

36. Fujishima, A., T.N. Rao, and D.A. Tryk, *Titanium dioxide photocatalysis.* Journal of Photochemistry and Photobiology C: Photochemistry Reviews, 2000. 1(1): p. 1-21.

37. Turchi, C.S. and D.F. Ollis, *Photocatalytic degradation of organic water contaminants: Mechanisms involving hydroxyl radical attack.* Journal of Catalysis, 1990. 122(1): p. 178-192.

38. Pekakis, P.A., N.P. Xekoukoulotakis, and D. Mantzavinos, *Treatment of textile dyehouse wastewater by TiO2 photocatalysis.* Water Research, 2006. 40(6): p. 1276-1286.

39. Linsebigler, A.L., G. Lu, and J.T. Yates, *Photocatalysis on TiO2 Surfaces: Principles, Mechanisms, and Selected Results.* Chemical Reviews, 1995. 95(3): p. 735-758.

40. Paleologou, A., et al., *Disinfection of water and wastewater by TiO2 photocatalysis, sonolysis and UV-C irradiation.* Catalysis Today, 2007. 129(1–2): p. 136-142.

41.   Fujishima, A. and K. Honda, *Electrochemical Photolysis of Water at a Semiconductor Electrode.* Nature, 1972. 238(5358): p. 37-38.

42.   Macák, J.M., H. Tsuchiya, and P. Schmuki, *High-Aspect-Ratio TiO2 Nanotubes by Anodization of Titanium.* Angewandte Chemie International Edition, 2005. 44(14): p. 2100-2102.

43.   Yu, J., et al., *Preparation, Microstructure and Photocatalytic Activity of the Porous TiO2 Anatase Coating by Sol-Gel Processing.* Journal of Sol-Gel Science and Technology, 2000. 17(2): p. 163-171.

44.   Grosso, D., et al., *Highly Porous TiO$_2$ Anatase Optical Thin Films with Cubic Mesostructure Stabilized at 700 °C.* Chemistry of Materials, 2003. 15(24): p. 4562-4570.

45.   Zhang, D., et al., *Room-Temperature Synthesis of Porous Nanoparticulate TiO2 Films for Flexible Dye-Sensitized Solar Cells.* Advanced Functional Materials, 2006. 16(9): p. 1228-1234.

46.   Chu, S.-Z., et al., *Highly porous TiO$_2$/Al$_2$O$_3$ composite nanostructures on glass by anodization and the sol-gel process: fabrication and photocatalytic characteristics.* Journal of Materials Chemistry, 2003. 13(4): p. 866-870.

47.   Colón, G., M.C. Hidalgo, and J.A. Navío, *A novel preparation of high surface area TiO$_2$ nanoparticles from alkoxide precursor and using active carbon as additive.* Catalysis Today, 2002. 76(2–4): p. 91-101.

48.   Paulose, M., et al., *Anodic Growth of Highly Ordered TiO2 Nanotube Arrays to 134 μm in Length.* The Journal of Physical Chemistry B, 2006. 110(33): p. 16179-16184.

49.   Yoriya, S. and C.A. Grimes, *Self-Assembled TiO2 Nanotube Arrays by Anodization of Titanium in Diethylene Glycol: Approach to Extended Pore Widening.* Langmuir, 2009. 26(1): p. 417-420.

50.   Roy, S.C., et al., *Toward Solar Fuels: Photocatalytic Conversion of Carbon Dioxide to Hydrocarbons.* ACS Nano, 2010. 4(3): p. 1259-1278.

51.   Vorobyev, A.Y., V.S. Makin, and C. Guo, *Periodic ordering of random surface nanostructures induced by femtosecond laser pulses on metals.* Journal of Applied Physics, 2007. 101(3): p. 034903.

52.   Wang, C., et al., *Using metal nanostructures to form hydrocarbons from carbon dioxide, water and sunlight.* AIP Advances, 2011. 1(4): p. 042124.

53.   Li, R.R., et al., *Dense arrays of ordered GaAs nanostructures by selective area growth on substrates patterned by block copolymer lithography.* Applied Physics Letters, 2000. 76(13): p. 1689-1691.

127

54.   Choi, Y.-K., et al., *Fabrication of Sub-10-nm Silicon Nanowire Arrays by Size Reduction Lithography.* The Journal of Physical Chemistry B, 2003. 107(15): p. 3340-3343.

55.   Crepaldi, E.L., et al., *Controlled Formation of Highly Organized Mesoporous Titania Thin Films: From Mesostructured Hybrids to Mesoporous Nanoanatase TiO$_2$.* Journal of the American Chemical Society, 2003. 125(32): p. 9770-9786.

56.   Greeley, J. and M. Mavrikakis, *Alloy catalysts designed from first principles.* Nat Mater, 2004. 3(11): p. 810-815.

57.   Deganello, F., et al., *Catalytic reduction of nitrates and nitrites in water solution on pumice-supported Pd–Cu catalysts.* Applied Catalysis B: Environmental, 2000. 24(3–4): p. 265-273.

58.   Gao, W., et al., *Titania supported Pd-Cu bimetallic catalyst for the reduction of nitrate in drinking water.* Applied Catalysis B: Environmental, 2003. 46(2): p. 341-351.

59.   Wang, C., et al., *CO Hydrogenation to Light Alkenes Over Mn/Fe Catalysts Prepared by Coprecipitation and Sol-gel Methods.* Catalysis Letters, 2005. 105(1): p. 93-101.

60.   Ma, W., et al., *Mo−Fe Catalysts Supported on Activated Carbon for Synthesis of Liquid Fuels by the Fischer-Tropsch Process: Effect of Mo Addition on Reducibility, Activity, and Hydrocarbon Selectivity.* Energy & Fuels, 2006. 20(6): p. 2299-2307.

61.   Lohitharn, N., J.G. Goodwin Jr, and E. Lotero, *Fe-based Fischer–Tropsch synthesis catalysts containing carbide-forming transition metal promoters.* Journal of Catalysis, 2008. 255(1): p. 104-113.

62.   Lee, Y.-W., et al., *Octahedral Pt-Pd alloy catalysts with enhanced oxygen reduction activity and stability in proton exchange membrane fuel cells.* RSC Advances, 2012. 2(3): p. 1119-1125.

63.   Hirakawa, T. and P.V. Kamat, *Charge Separation and Catalytic Activity of Ag@TiO$_2$ Core−Shell Composite Clusters under UV−Irradiation.* Journal of the American Chemical Society, 2005. 127(11): p. 3928-3934.

64.   Awazu, K., et al., *A Plasmonic Photocatalyst Consisting of Silver Nanoparticles Embedded in Titanium Dioxide.* Journal of the American Chemical Society, 2008. 130(5): p. 1676-1680.

65.   Cheng, J., et al., *Preparation of Fe (core)/SiO$_2$ (shell) composite particles with improved oxidation-resistance.* Materials Research Bulletin, 2006. 41(8): p. 1424-1429.

66.   Akimov, Y. and W. Koh, *Design of Plasmonic Nanoparticles for Efficient Subwavelength Light Trapping in Thin-Film Solar Cells.* Plasmonics, 2011. 6(1): p. 155-161.

128

67. Hägglund, C. and B. Kasemo, *Nanoparticle Plasmonics for 2D-Photovoltaics:Mechanisms, Optimization, and Limits.* Opt. Express, 2009. 17(14): p. 11944-11957.

68. An, C., S. Peng, and Y. Sun, *Facile Synthesis of Sunlight-Driven AgCl:Ag Plasmonic Nanophotocatalyst.* Advanced Materials, 2010. 22(23): p. 2570-2574.

69. Christopher, P., H. Xin, and S. Linic, *Visible-light-enhanced catalytic oxidation reactions on plasmonic silver nanostructures.* Nat Chem, 2011. 3(6): p. 467-472.

70. Ingram, D.B. and S. Linic, *Water Splitting on Composite Plasmonic-Metal/Semiconductor Photoelectrodes: Evidence for Selective Plasmon-Induced Formation of Charge Carriers near the Semiconductor Surface.* Journal of the American Chemical Society, 2011. 133(14): p. 5202-5205.

71. Christopher, P., D.B. Ingram, and S. Linic, *Enhancing Photochemical Activity of Semiconductor Nanoparticles with Optically Active Ag Nanostructures: Photochemistry Mediated by Ag Surface Plasmons.* The Journal of Physical Chemistry C, 2010. 114(19): p. 9173-9177.

72. El-Eskandarany, M.S., K. Aoki, and K. Suzuki, *Formation of amorphous aluminum tantalum nitride powders by mechanical alloying.* Applied Physics Letters, 1992. 60(13): p. 1562-1563.

73. Xie, X., et al., *Low-temperature oxidation of CO catalysed by Co3O4 nanorods.* Nature, 2009. 458(7239): p. 746-749.

74. Varghese, O.K., et al., *High-Rate Solar Photocatalytic Conversion of CO2 and Water Vapor to Hydrocarbon Fuels.* Nano Letters, 2009. 9(2): p. 731-737.

75. Sasirekha, N., S.J.S. Basha, and K. Shanthi, *Photocatalytic performance of Ru doped anatase mounted on silica for reduction of carbon dioxide.* Applied Catalysis B: Environmental, 2006. 62(1–2): p. 169-180.

76. Wu, J., *Photocatalytic Reduction of Greenhouse Gas CO<sub>2</sub> to Fuel.* Catalysis Surveys from Asia, 2009. 13(1): p. 30-40.

77. Anpo, M., et al., *Photocatalytic reduction of CO_2 with H_2O on various titanium oxide catalysts.* Journal of Electroanalytical Chemistry, 1995. 396(1–2): p. 21-26.

78. Tseng, I.H., W.-C. Chang, and J.C.S. Wu, *Photoreduction of CO2 using sol–gel derived titania and titania-supported copper catalysts.* Applied Catalysis B: Environmental, 2002. 37(1): p. 37-48.

79. Tseng, I.H. and J.C.S. Wu, *Chemical states of metal-loaded titania in the photoreduction of CO2.* Catalysis Today, 2004. 97(2–3): p. 113-119.

80. Hou, W., et al., *Photocatalytic Conversion of CO_2 to Hydrocarbon Fuels via Plasmon-Enhanced Absorption and Metallic Interband Transitions.* ACS Catalysis, 2011. 1(8): p. 929-936.

81.   Li, Y., et al., *Photocatalytic reduction of CO2 with H2O on mesoporous silica supported Cu/TiO2 catalysts.* Applied Catalysis B: Environmental, 2010. 100(1–2): p. 386-392.

82.   Wang, C., et al., *Visible Light Photoreduction of CO2 Using CdSe/Pt/TiO2 Heterostructured Catalysts.* The Journal of Physical Chemistry Letters, 2009. 1(1): p. 48-53.

83.   *American Precious Metals Exchange, Inc. (APMEX)* Available from: http://www.apmex.com/.

84.   Couwenberg, P.M., Q. Chen, and G.B. Marin, *Kinetics of a Gas-Phase Chain Reaction Catalyzed by a Solid: The Oxidative Coupling of Methane over Li/MgO-Based Catalysts.* Ind. Eng. Chem. Res., 1996. 35(11): p. 3999-4011.

85.   Stoeber, W., A. Fink, and E. Bohn, *Controlled growth of monodisperse silica spheres in the micron size range.* J. Colloid Interface Sci. , 1968. 26(1): p. 62-9.

86.   Reculusa, S., et al., *Synthesis of Daisy-Shaped and Multipod-like Silica/Polystyrene Nanocomposites.* Nano Lett. , 2004. 4(9): p. 1677-1682.

87.   Westcott, S.L., et al., *Formation and Adsorption of Clusters of Gold Nanoparticles onto Functionalized Silica Nanoparticle Surfaces.* Langmuir, 1998. 14(19): p. 5396-5401.

88.   Heikkinen, J.J., J.P. Heiskanen, and O.E.O. Hormi, *Grafting of functionalized silica particles with poly(acrylic acid).* Polym. Adv. Technol. , 2006. 17(6): p. 426-429.

89.   Liu, J., R. Pelton, and A.N. Hrymak, *Properties of Poly(N-isopropylacrylamide)-Grafted Colloidal Silica.* J. Colloid Interface Sci. , 2000. 227(2): p. 408-411.

90.   Bourgeat-Lami, E. and J. Lang, *Encapsulation of inorganic particles by dispersion polymerization in polar media. 1. Silica nanoparticles encapsulated by polystyrene.* J. Colloid Interface Sci. , 1998. 197(2): p. 293-308.

91.   Petit, C., A. Taleb, and M.P. Pileni, *Cobalt Nanosized Particles Organized in a 2D Superlattice: Synthesis, Characterization, and Magnetic Properties.* J. Phys. Chem. B 1999. 103(11): p. 1805-1810.

92.   Sun, S. and C.B. Murray, *Synthesis of monodisperse cobalt nanocrystals and their assembly into magnetic superlattices.* J. Appl. Phys. , 1999. 85(8, Pt. 2A): p. 4325-4330.

93.   Sun, S., et al., *Monodisperse FePt nanoparticles and ferromagnetic FePt nanocrystal superlattices.* Science (Washington, D. C.) 2000. 287(5460): p. 1989-1992.

94.   Puntes, V.F., K.M. Krishnan, and A.P. Alivisatos, *Colloidal nanocrystal shape and size control: The case of cobalt.* Science (Washington, DC, U. S.) 2001. 291(5511): p. 2115-2117.

130

95.   Apsel, S.E., et al., *Surface-enhanced magnetism in nickel clusters.* Phys. Rev. Lett., 1996. 76(9): p. 1441-4.

96.   Miyajima, K., et al., *Stern-Gerlach Experiments of One-Dimensional Metal-Benzene Sandwich Clusters: Mn(C6H6)m (M = Al, Sc, Ti, and V).* J. Am. Chem. Soc. , 2007. 129(27): p. 8473-8480.

97.   Zemski, K.A., D.R. Justes, and A.W. Castleman, Jr., *Studies of Metal Oxide Clusters: Elucidating Reactive Sites Responsible for the Activity of Transition Metal Oxide Catalysts.* J. Phys. Chem. B 2002. 106(24): p. 6136-6148.

98.   El-Shall, M.S. and W. Slack, *Ultrafine Metal Particles in Polymers and the Formation of Periodic Polymer Stripes.* Macromolecules 1995. 28(24): p. 8456-8.

99.   Guo, B.C., et al., *Generation of metal-carbon and metal-nitrogen clusters with a laser induced plasma technique.* J. Chem. Phys., 1992. 97(7): p. 5243-5.

100.   Yang, Y.A., et al., *Direct ejection of clusters from nonmetallic solids during laser vaporization.* Phys. Rev. Lett. , 1991. 66(9): p. 1205-8.

101.   Bondybey, V.E. and J.H. English, *Laser induced fluorescence of metal clusters produced by laser vaporization: Gas phase spectrum of lead (Pb2).* J. Chem. Phys. , 1981. 74(12): p. 6978-9.

102.   He, Y., X. Li, and M.T. Swihart, *Laser-Driven Aerosol Synthesis of Nickel Nanoparticles.* Chem. Mater. , 2005. 17(5): p. 1017-1026.

103.   Ishigaki, T., *Synthesis of nanoparticles by thermal plasma technology.* Mater. Integr. , 2008. 21(7): p. 58-66.

104.   Shah, P. and A. Gavrin, *Synthesis of nanoparticles using high-pressure sputtering for magnetic domain imaging.* J. Magn. Magn. Mater. , 2006. 301(1): p. 118-123.

105.   Lerner, M.I. and V.V. Shamanskii, *Synthesis of nanoparticles by high-power current pulses.* J. Struct. Chem. , 2004. 45(Suppl.): p. S111-S114.

106.   Desnica, U.V., et al., *Direct ion beam synthesis of II-VI nanocrystals.* Nucl. Instrum. Methods Phys. Res., Sect. B 2004. 216: p. 407-413.

107.   Taboada, E., et al., *Supercritical-Fluid-Assisted One-Pot Synthesis of Biocompatible Core(gamma -Fe2O3)/Shell(SiO2) Nanoparticles as High Relaxivity T2-Contrast Agents for Magnetic Resonance Imaging.* Adv. Funct. Mater. , 2009. 19(14): p. 2319-2324.

108.   Kim, J., et al., *Metal nanoparticle synthesis using supercritical alcohol.* Mater. Lett. , 2009. 63(21): p. 1880-1882.

109. Bremholm, M., M. Felicissimo, and B.B. Iversen, *Time-Resolved In Situ Synchrotron X-ray Study and Large-Scale Production of Magnetite Nanoparticles in Supercritical Water.* Angew. Chem., Int. Ed. , 2009. 48(26): p. 4788-4791, S4788/1-S4788/12.

110. Li, K. and F.-S. Zhang, *Preparing silver nanoparticles in supercritical water.* Mater. Lett. , 2009. 63(3-4): p. 437-440.

111. Panigrahi, M.R. and S. Panigrahi, *Synthesis and microstructure of Ca-doped BaTiO3 ceramics prepared by high-energy ball-milling.* Phys. B (Amsterdam, Neth.) 2009. 404(21): p. 4267-4272.

112. Ghosh, B. and S.K. Pradhan, *Microstructural characterization of nanocrystalline SiC synthesized by high-energy ball-milling.* J. Alloys Compd. , 2009. 486(1-2): p. 480-485.

113. Filipek, E. and K. Wieczorek-Ciurowa, *Comparison between the synthesis in molybdenum and antimony oxides system by high-temperature treatment and high-energy ball milling.* J. Therm. Anal. Calorim. , 2009. 97(1): p. 105-110.

114. Manova, E., et al., *Mechanochemical synthesis and characterization of nanodimensional iron-cobalt spinel oxides.* J. Alloys Compd. , 2009. 485(1-2): p. 356-361.

115. Nagy, J.B., et al., *Nanoparticles in microemulsions: a general approach.* NATO ASI Ser., Ser. 3: High Technology, 1996. 18(Nanoparticles in Solids and Solutions): p. 71-129.

116. Petit, C. and M.P. Pileni, *Nanosize cobalt boride particles: control of the size and properties.* J. Magn. Magn. Mater. , 1997. 166(1-2): p. 82-90.

117. Chen, J.P., et al., *Enhanced magnetization of nanoscale colloidal cobalt particles.* Phys. Rev. B: Condens. Matter 1995. 51(17): p. 11527-32.

118. Suslick, K.S., et al., *Nanostructured Fe-Co catalysts generated by ultrasound.* Mater. Res. Soc. Symp. Proc. , 1994. 351(Molecularly Designed Ultrafine/Nanostructured Materials): p. 443-8.

119. Teo, B.M., et al., *Novel One-Pot Synthesis of Magnetite Latex Nanoparticles by Ultrasound Irradiation.* Langmuir 2009. 25(5): p. 2593-2595.

120. Vidotti, M., R.P. Salvador, and S.I. Cordoba de Torresi, *Synthesis and characterization of stable Co and Cd doped nickel hydroxide nanoparticles for electrochemical applications.* Ultrason. Sonochem. , 2008. 16(1): p. 35-40.

121. Dahl, J.A., B.L.S. Maddux, and J.E. Hutchison, *Toward Greener Nanosynthesis.* Chem. Rev. (Washington, DC, U. S.) 2007. 107(6): p. 2228-2269.

122. Pi, Z.-b., et al., *Preparation of ultrafine particles of azithromycin by sonochemical method.* Nanomedicine (N. Y., NY, U. S.) 2007. 3(1): p. 86-88.

123. Ren, L., et al., *Synthesis of CoC2O4.2H2O nanorods and their thermal decomposition to Co3O4 nanoparticles.* Chem. Phys. Lett. , 2009. 476(1-3): p. 78-83.

124. Chernavskii, P.A., et al., *Formation of Co nanoparticles in the process of thermal decomposition of the cobalt complex with hexamethylenetetramine $(NO_3)_2Co(H_2O)_6(HMTA)_2.4(H_2O)$.* Russ. J. Phys. Chem. A 2008. 82(13): p. 2176-2181.

125. Papirer, E., et al., *The preparation of a ferrofluid by decomposition of dicobalt octacarbonyl. II. Nucleation and growth of particles.* J. Colloid Interface Sci. , 1983. 94(1): p. 220-8.

126. Papirer, E., et al., *The preparation of a ferrofluid by decomposition of dicobalt octacarbonyl. I. Experimental parameters.* J. Colloid Interface Sci. , 1983. 94(1): p. 207-19.

127. Van Dillen, A.J., et al., *Synthesis of supported catalysts by impregnation and drying using aqueous chelated metal complexes.* J. Catal. , 2003. 216(1-2): p. 257-264.

128. Wang, W.J. and Y.W. Chen, *Influence of metal loading on the reducibility and hydrogenation activity of cobalt/alumina catalysts.* Appl. Catal. , 1991. 77(2): p. 223-33.

129. Calleja, G., A. De Lucas, and R. Van Grieken, *Cobalt/HZSM-5 zeolite catalyst for the conversion of syngas to hydrocarbons.* Appl. Catal. , 1991. 68(1-2): p. 11-29.

130. Zhang, Y., et al., *Effect of Water Vapor on the Reduction of Ru-Promoted Co/Al2O3.* J. Catal. , 1999. 188(2): p. 281-290.

131. Bogush, G.H., M.A. Tracy, and C.F. Zukoski Iv, *Preparation of monodisperse silica particles: Control of size and mass fraction.* J. Non-Cryst. Solids, 1988. 104(1): p. 95-106.

132. Bogush, G.H. and C.F. Zukoski Iv, *Uniform silica particle precipitation: An aggregative growth model.* J. Colloid Interface Sci., 1991. 142(1): p. 19-34.

133. Tan, C.G., B.D. Bowen, and N. Epstein, *Production of monodisperse colloidal silica spheres: Effect of temperature.* J. Colloid Interface Sci., 1987. 118(1): p. 290-293.

134. Matsoukas, T. and E. Gulari, *Dynamics of growth of silica particles from ammonia-catalyzed hydrolysis of tetra-ethyl-orthosilicate.* J. Colloid Interface Sci., 1988. 124(1): p. 252-261.

135. Huber, D.L., *Synthesis, properties, and applications of Iron nanoparticles.* Small 2005. 1(5): p. 482-501.

136. Puntes, V.F., K. Krishnan, and A.P. Alivisatos, *Synthesis of Colloidal Cobalt Nanoparticles with Controlled Size and Shapes.* Topics in Catalysis, 2002. 19(2): p. 145-148.

137. Shukla, N., et al., *Surfactant effects on the shapes of cobalt nanoparticles.* Materials Letters, 2006. 60(16): p. 1950-1955.

138. Zhuo, L., et al., *Solvothermal Synthesis of CoO, Co3O4, Ni(OH)2 and Mg(OH)2 Nanotubes.* Crystal Growth & Design, 2008. 9(1): p. 1-6.

139. Zhang, L. and D. Xue, *Preparation and magnetic properties of pure CoO nanoparticles.* Journal of Materials Science Letters, 2002. 21(24): p. 1931-1933.

140. Yu, Y., et al., *Facile synthesis, characterization and electrochemical properties of cuspate deltoid CoO crystallites.* Journal of Alloys and Compounds, 2009. 471(1â€'2): p. 268-271.

141. Prieto, G., et al., *Cobalt particle size effects in Fischer-Tropsch synthesis: structural and in-situ spectroscopic characterization on reverse micelle-synthesised Co/ITQ-2 zeolite catalysts.* J. Catal. , 2009. 266(1): p. 129-144.

142. Huber, D.L., et al., *Synthesis of highly magnetic iron nanoparticles suitable for field structuring using a [beta]-diketone surfactant.* J. Magn. Magn. Mater., 2004. 278(3): p. 311-316.

143. Gazit, O., N. Dan, and R. Tannenbaum, *Nanocluster Nucleation and Growth in Polymeric Media Below the Glass Transition.* Macromolecules (Washington, DC, U. S.) 2008. 41(6): p. 2164-2171.

144. David, K., et al., *Effect of polymer architecture on metal nanoclusters.* Polymer 2006. 47(25): p. 8344-8349.

145. Weigelt, S., et al., *Covalent interlinking of an aldehyde and an amine on a Au(111) surface in ultrahigh vacuum.* Angew. Chem., Int. Ed. , 2007. 46(48): p. 9227-9230.

146. Bae, S.S., et al., *Monolayer assembly and striped architecture of Co nanoparticles on organic functionalized Si surfaces.* Appl. Phys. A: Mater. Sci. Process. , 2005. 80(6): p. 1305-1310.

147. Saib, A.M., et al., *Preparation and characterisation of spherical Co/SiO2 model catalysts with well-defined nano-sized cobalt crystallites and a comparison of their stability against oxidation with water.* J. Catal., 2006. 239(2): p. 326-339.

148. Steen, E.v., et al., *TPR Study on the Preparation of Impregnated Co/SiO2Catalysts.* J. Catal., 1996. 162(2): p. 220-229.

149. Yiu, H.H.P., et al., *Synthesis of novel magnetic iron metal-silica (Fe-SBA-15) and magnetite-silica (Fe3O4-SBA-15) nanocomposites with a high iron content using temperature-programed reduction.* Nanotechnology 2008. 19(25): p. 255606/1-255606/7.

134

150.   Naumann d'Alnoncourt, R., et al., *The influence of strongly reducing conditions on strong metal-support interactions in Cu/ZnO catalysts used for methanol synthesis.* Phys. Chem. Chem. Phys. , 2006. 8(13): p. 1525-1538.

151.   Kadkhodayan, A. and A. Brenner, *Temperature-programmed reduction and oxidation of metals supported on γ-alumina.* Journal of Catalysis, 1989. 117(2): p. 311-321.

152.   Silverstein, R.M., G.C. Bassler, and T.C. Morril, *Spectrometric Identification of Organic Compounds.* Fourth ed. 1981: John Wiley & Sons.

153.   Chen, J.G., et al., *Study on Deactivation of $Co/ZrO_2/SiO_2$ Catalyst For Fischer-Tropsch Synthesis.* Reaction Kinetics and Catalysis Letters, 2001. 73(1): p. 169-177.

154.   Rosynek, M.P. and C.A. Polansky, *Effect of cobalt source on the reduction properties of silica-supported cobalt catalysts.* Appl. Catal. , 1991. 73(1): p. 97-112.

155.   Roe, G.M., et al., *Role of supports for cobalt-based catalysts used in Fischer-Tropsch synthesis of hydrocarbons.* Stud. Surf. Sci. Catal. , 1988. 36(Methane Convers.): p. 509-15.

156.   Paryjczak, T., J. Rynkowski, and S. Karski, *Thermoprogrammed reduction of cobalt oxide catalysts.* J. Chromatogr. , 1980. 188(1): p. 254-6.

157.   Van't Blik, H.F.J., D.C. Koningsberger, and R. Prins, *Characterization of supported cobalt and cobalt-rhodium catalysts. III. Temperature-programmed reduction (TPR), oxidation (TPO), and EXAFS of cobalt-rhodium/silica.* J. Catal. , 1986. 97(1): p. 210-18.

158.   Kogelbauer, A., J.C. Weber, and J.G. Goodwin, Jr., *The formation of cobalt silicates on Co/SiO2 under hydrothermal conditions.* Catal. Lett. , 1995. 34(3,4): p. 259-67.

159.   Coulter, K.E. and A.G. Sault, *Effects of activation on the surface properties of silica-supported cobalt catalysts.* J. Catal. , 1995. 154(1): p. 56-64.

160.   van Steen, E., et al., *TPR study on the preparation of impregnated Co/SiO2 catalysts.* J. Catal. , 1996. 162(2): p. 220-229.

161.   Khodakov, A.Y., et al., *Reducibility of Cobalt Species in Silica-Supported Fischer–Tropsch Catalysts.* Journal of Catalysis, 1997. 168(1): p. 16-25.

162.   Kadinov, G., et al., *IR spectroscopy study of CO adsorption and of the interaction between CO and hydrogen on alumina-supported cobalt.* Journal of the Chemical Society, Faraday Transactions, 1998. 94(19): p. 3027-3031.

163.   Kissinger, H.E., *Reaction Kinetics in Differential Thermal Analysis.* Analytical Chemistry, 1957. 29(11): p. 1702-1706.

164. Wimmers, O.J., P. Arnoldy, and J.A. Moulijn, *Determination of the reduction mechanism by temperature-programmed reduction: application to small iron oxide (Fe2O3) particles.* The Journal of Physical Chemistry, 1986. 90(7): p. 1331-1337.

165. Gentry, S.J., N.W. Hurst, and A. Jones, *Temperature programmed reduction of copper ions in zeolites.* Journal of the Chemical Society, Faraday Transactions 1: Physical Chemistry in Condensed Phases, 1979. 75: p. 1688-1699.

166. Ciobîca, I.M., et al., *Adsorbate induced reconstruction of cobalt surfaces.* Surface Science, 2008. 602(1): p. 17-27.

167. Hendriksen, B.L.M., et al., *The role of steps in surface catalysis and reaction oscillations.* Nat Chem, 2010. 2(9): p. 730-734.

168. Ortiz, M.I., A. Romero, and A. Irabien, *Integral kinetic analysis from temperature programmed reaction data: alkaline hydrolysis of ethyl acetate as test reaction.* Thermochimica Acta, 1989. 141(0): p. 169-180.

169. Coats, A.W. and J.P. Redfern, *Kinetic Parameters from Thermogravimetric Data.* Nature, 1964. 201(4914): p. 68-69.

170. Gong, X.-Q., R. Raval, and P. Hu, *CO dissociation and O removal on Co(0 0 0 1): a density functional theory study.* Surface Science, 2004. 562(1-3): p. 247-256.

171. Ge, Q. and M. Neurock, *Adsorption and Activation of CO over Flat and Stepped Co Surfaces: A First Principles Analysis.* The Journal of Physical Chemistry B, 2006. 110(31): p. 15368-15380.

172. Lanzani, G., et al., *CO Disproportionation on a Nanosized Iron Cluster.* The Journal of Physical Chemistry C, 2009. 113(30): p. 12939-12942.

173. Narayanan, R. and M.A. El-Sayed, *Shape-Dependent Catalytic Activity of Platinum Nanoparticles in Colloidal Solution.* Nano Letters, 2004. 4(7): p. 1343-1348.

174. Hanprasopwattana, A., et al., *Morphology of titania coatings on silica gel.* Catal. Lett. , 1997. 45(3,4): p. 165-175.

175. Caruso, F., et al., *Hollow titania spheres from layered precursor deposition on sacrificial colloidal core particles.* Adv. Mater. (Weinheim, Ger.) 2001. 13(10): p. 740-744.

176. Cheng, B., Y. Le, and J. Yu, *Preparation and enhanced photocatalytic activity of $Ag@TiO_2$ core-shell nanocomposite nanowires.* Journal of Hazardous Materials, 2010. 177(1-3): p. 971-977.

177. Irannejad, A., et al., *Effect of the TiO_2 shell thickness on the dye-sensitized solar cells with $ZnO-TiO_2$ core-shell nanorod electrodes.* Electrochimica Acta, 2011. 58(0): p. 19-24.

136

178. Linic, S., P. Christopher, and D.B. Ingram, *Plasmonic-metal nanostructures for efficient conversion of solar to chemical energy.* Nat Mater, 2011. 10(12): p. 911-921.

179. Chen, L., et al., *Characterization of Ag/Pt core-shell nanoparticles by UV–vis absorption, resonance light-scattering techniques.* Spectrochimica Acta Part A: Molecular and Biomolecular Spectroscopy, 2007. 68(3): p. 484-490.

180. Heskins, M. and J.E. Guillet, *Solution Properties of Poly(N-isopropylacrylamide).* Journal of Macromolecular Science: Part A - Chemistry, 1968. 2(8): p. 1441-1455.

181. Zhang, Q., L. Gao, and J. Guo, *Effects of calcination on the photocatalytic properties of nanosized TiO2 powders prepared by TiCl4 hydrolysis.* Applied Catalysis B: Environmental, 2000. 26(3): p. 207-215.

182. Pajonk, G.M., *Aerogel catalysts.* Appl. Catal., 1991. 72(2): p. 217-266.

183. Zhang, Z., et al., *Role of Particle Size in Nanocrystalline TiO2-Based Photocatalysts.* The Journal of Physical Chemistry B, 1998. 102(52): p. 10871-10878.

184. Inoue, T., et al., *Photoelectrocatalytic reduction of carbon dioxide in aqueous suspensions of semiconductor powders.* Nature, 1979. 277(5698): p. 637-638.

185. Dimitrijevic, N.M., et al., *Role of Water and Carbonates in Photocatalytic Transformation of CO_2 to CH_4 on Titania.* Journal of the American Chemical Society, 2011. 133(11): p. 3964-3971.

186. Lee, S.-w., et al., *Anatase TiO_2 Nanoparticle Coating on Barium Ferrite Using Titanium Bis-Ammonium Lactato Dihydroxide and Its Use as a Magnetic Photocatalyst.* Chemistry of Materials, 2004. 16(6): p. 1160-1164.

187. Hurum, D.C., et al., *Recombination Pathways in the Degussa P25 Formulation of TiO_2: Surface versus Lattice Mechanisms.* The Journal of Physical Chemistry B, 2004. 109(2): p. 977-980.

188. Subramanian, V., E.E. Wolf, and P.V. Kamat, *Catalysis with TiO2/Gold Nanocomposites. Effect of Metal Particle Size on the Fermi Level Equilibration.* Journal of the American Chemical Society, 2004. 126(15): p. 4943-4950.

189. Wood, A., M. Giersig, and P. Mulvaney, *Fermi Level Equilibration in Quantum Dot−Metal Nanojunctions†.* The Journal of Physical Chemistry B, 2001. 105(37): p. 8810-8815.

190. Kimling, J., et al., *Turkevich Method for Gold Nanoparticle Synthesis Revisited.* The Journal of Physical Chemistry B, 2006. 110(32): p. 15700-15707.

191. Pillai, Z.S. and P.V. Kamat, *What Factors Control the Size and Shape of Silver Nanoparticles in the Citrate Ion Reduction Method?* The Journal of Physical Chemistry B, 2003. 108(3): p. 945-951.

192.   Rivas, L., et al., *Growth of Silver Colloidal Particles Obtained by Citrate Reduction To Increase the Raman Enhancement Factor.* Langmuir, 2001. 17(3): p. 574-577.

193.   Gao, J., et al., *Bimetallic Ag-Pt hollow nanoparticles: Synthesis and tunable surface plasmon resonance.* Scripta Materialia, 2007. 57(8): p. 687-690.

194.   He, W., et al., *Formation of AgPt Alloy Nanoislands via Chemical Etching with Tunable Optical and Catalytic Properties.* Langmuir, 2009. 26(6): p. 4443-4448.

195.   Yang, J., et al., *Synthesis of Pt/Ag bimetallic nanorattle with Au core.* Scripta Materialia, 2006. 54(2): p. 159-162.

196.   Kobayashi, Y., et al., *Silica coating of silver nanoparticles using a modified Stober method.* Journal of Colloid and Interface Science, 2005. 283(2): p. 392-396.

197.   Wang, Z.-Y., et al., *CO2 photoreduction using NiO/InTaO4 in optical-fiber reactor for renewable energy.* Applied Catalysis A: General, 2010. 380(1–2): p. 172-177.

198.   Yoneyama, H., *Photoreduction of carbon dioxide on quantized semiconductor nanoparticles in solution.* Catalysis Today, 1997. 39(3): p. 169-175.

199.   Yang, Y., et al., *Unexpected Long-Term Instability of ZnO Nanowires Protected by a TiO$_2$ Shell.* Journal of the American Chemical Society, 2009. 131(39): p. 13920-13921.

200.   Fu, H., et al., *Photocorrosion Inhibition and Enhancement of Photocatalytic Activity for ZnO via Hybridization with C60.* Environmental Science & Technology, 2008. 42(21): p. 8064-8069.

201.   Kislov, N., et al., *Photocatalytic Degradation of Methyl Orange over Single Crystalline ZnO: Orientation Dependence of Photoactivity and Photostability of ZnO.* Langmuir, 2009. 25(5): p. 3310-3315.

202.   Wu, W., et al., *Preparation and properties of composite particles made by nano zinc oxide coated with titanium dioxide.* Journal of Materials Science, 2006. 41(18): p. 5845-5850.

203.   Barreca, D., et al., *First Example of ZnⱯTiO $_2$ Nanocomposites by Chemical Vapor Deposition: Structure, Morphology, Composition, and Gas Sensing Performances.* Chemistry of Materials, 2007. 19(23): p. 5642-5649.

204.   Park, K., et al., *Effect of an Ultrathin TiO2 Layer Coated on Submicrometer-Sized ZnO Nanocrystallite Aggregates by Atomic Layer Deposition on the Performance of Dye-Sensitized Solar Cells.* Advanced Materials, 2010. 22(21): p. 2329-2332.

205.   Kataoka, K., A. Harada, and Y. Nagasaki, *Block copolymer micelles for drug delivery: design, characterization and biological significance.* Advanced Drug Delivery Reviews, 2001. 47(1): p. 113-131.

138

206. Baxter, S. and A.B.D. Cassie, *8—The water repellency of fabrics and a new water repellency test.* Journal of the Textile Institute Transactions, 1945. 36(4): p. T67-T90.

207. Martines, E., et al., *Superhydrophobicity and Superhydrophilicity of Regular Nanopatterns.* Nano Letters, 2005. 5(10): p. 2097-2103.

208. Qin, S., et al., *Photocatalytic reduction of CO2 in methanol to methyl formate over CuO–TiO2 composite catalysts.* Journal of Colloid and Interface Science, 2011. 356(1): p. 257-261.

209. Ku, Y., W.-H. Lee, and W.-Y. Wang, *Photocatalytic reduction of carbonate in aqueous solution by UV/TiO2 process.* Journal of Molecular Catalysis A: Chemical, 2004. 212(1–2): p. 191-196.

210. Zhang, H., et al., *Synthesis of TiO2/SiO2 Core/Shell Nanocable Arrays.* The Journal of Physical Chemistry B, 2004. 108(39): p. 14866-14869.

211. Ma, M. and R.M. Hill, *Superhydrophobic surfaces.* Current Opinion in Colloid & Interface Science, 2006. 11(4): p. 193-202.

212. Lee, J.-W., et al., *Preparation and characterization of SiO$_2$/TiO$_2$ core-shell particles with controlled shell thickness.* Materials Chemistry and Physics, 2007. 106(1): p. 39-44.

213. Li, Q. and P. Dong, *Preparation of nearly monodisperse multiply coated submicrospheres with a high refractive index.* Journal of Colloid and Interface Science, 2003. 261(2): p. 325-329.

214. Guo, X.-C. and P. Dong, *Multistep Coating of Thick Titania Layers on Monodisperse Silica Nanospheres.* Langmuir, 1999. 15(17): p. 5535-5540.

215. Lee, J.W., et al., *The effects of sonification and TiO2 deposition on the micro-characteristics of the thermally treated SiO2/TiO2 spherical coreâ€"shell particles for photo-catalysis of methyl orange.* Microporous and Mesoporous Materials, 2008. 116(1â€"3): p. 561-568.

216. Ladhari, N., et al., *Stratified PEI-(PSS-PDADMAC)20-PSS-(PDADMAC-TiO2)n multilayer films produced by spray deposition.* Colloids and Surfaces A: Physicochemical and Engineering Aspects, 2008. 322(1â€"3): p. 142-147.

217. Chung, C.-J. and J.-H. Jean, *Synthesis of Hollow Titania Powder by the Hydrothermal Method.* Journal of the American Ceramic Society, 2008. 91(9): p. 3074-3077.

218. Agrawal, M., et al., *Fabrication of hollow titania microspheres with tailored shell thickness.* Colloid & Polymer Science, 2008. 286(5): p. 593-601.

219. Caruso, F., et al., *Hollow Titania Spheres from Layered Precursor Deposition on Sacrificial Colloidal Core Particles.* Advanced Materials, 2001. 13(10): p. 740-744.

139

220.   Jiang, Y., et al., *Preparation of Protamine–Titania Microcapsules Through Synergy Between Layer-by-Layer Assembly and Biomimetic Mineralization.* Advanced Functional Materials, 2009. 19(1): p. 150-156.

APPENDICES

Appendix A: Nomenclature

AAEM	Acetoacetoxyethyl methacrylate
Ag	Silver
AgCl	Silver chloride
Ag-Pt	Silver-platinum
Al	Aluminum
Al_2O_3	Alumina
AOT	sodium bis(2-ethylhexyl) sulfosuccinate
APDMS	N-Aminoethyl aminopropyl methyl dimethoxysilane
Au	Gold
$Au@SiO_2$	Gold-core silica shell
BUA	11-Bromoundecanoic acid
CeO_2	Ceria
CO	Carbon monoxide
Co	Cobalt
CO_2	Carbon dioxide
CoO	Cobalt oxide
Cr	Chromium
DFT	Density functional theory
Fe	Iron
FTIR	Fourier transform infra red
FTS	Fischer Tropsch synthesis
H_2	Hydrogen
IR	Infrared

Appendix A: (Continued)

Ir	Iridium
Mn	Manganese
Mo	Molybdenum
MPS	Methacryloxy propyltrimethoxysilane
N_2	Nitrogen
NH_3	Ammonia
Ni	Nickel
NIPAAM	N-isoproplyacrylamide
PAA	Polyacrylic acid
Pb	Lead
Pd	Palladium
Pd-Cu	Palladium-copper
Pt	Platinum
Rh	Rhodium
Ru	Ruthenium
SiO_2	Silica
$SiO_2@Au$	Silica-core gold shell
Ta	Tantalum
TeO_2	Telluria
TiO_2	Titania
TOF	Turn over frequency
UV	Ultraviolet
UV-Vis	Ultraviolet-visible

143

Appendix A: (Continued)

V	Vanadium
W	Tungsten
XRD	X-ray diffraction
Zr	Zirconium
ZrO_2	Zirconia